Different Approaches to Improve Metamorphic Buffer Layers Grown on a GaAs Substrate

Different Approaches to Improve Metamorphic Buffer Layers Grown on a GaAs Substrate

By

Sudip Kumar Saha

B.Sc (2009)

Bangladesh University of Engineering and Technology,

Dhaka, Bangladesh

A Thesis Submitted to the School of Graduate Studies in

Partial Fulfillment of the Requirements for the Degree of

Master of Applied Science

McMaster University © Copyright by Sudip Kumar Saha, September 2012

Master Of Applied Science (2012)	McMaster University
(Engineering Physics)	Hamilton, Ontario, Canada

TITLE	Different Approaches to Improve Metamorphic Buffer Layers Grown on a GaAs Substrate
AUTHOR	Sudip Kumar Saha, Bachelor of Science, Electrical and Electronic Engineering (Bangladesh University of Engineering and Technology)
SUPERVISOR	Dr. David A.Thompson, Professor Emeritus, Engineering Physics Dr. Daniel Cassidy, Professor, Engineering Physics
NUMBER OF PAGES	xi, 86

Abstract

Metamorphic buffer (MB) layers were studied as a means to grow epilayers on top of a GaAs substrate which have different lattice constant than the GaAs. Growths were done by molecular beam epitaxy on a GaAs (001) substrate. The growths of step-graded InGaAs and InGaAsP MBs have been investigated using both linear and logarithmic grading profiles. The logarithmic grading profile shows slight improvement in the crystal quality over the linear grading profiles. This is an indication that instead of increasing the strain with the same grading rate, it may be helpful to have higher grading rate at the beginning and lower grading rate at the end of the buffer.

InGaAsP graded buffers were grown where group III ratio was kept fixed. However due to the existence of phase separation and lower relaxation the quaternary growths exhibited no performance improvement as might have been expected from growths with only group V grading. Also, the effects of using an InGaP layer grown at low temperature before the MB were determined. Quantum wells (QW), which were grown on top of the MBs, were used to probe the optical emission properties. No significant difference was observed in photoluminescence between the samples with a low temperature layer and without a low temperature layer. Annealing enhanced the PL intensity but the crystal quality degraded due to the appearance of surface defects. Surface undulations, known as “cross-hatch” (CH), were observed in the top MB layers. Atomic force microscopy (AFM) was used to analyze the surface morphology and degree of polarization (DOP) measurement was used to analyze the strain features in the final MB layer. Similar patterns of both surface morphology and strain field indicate a correlation between these two. From analysis of the periodicity of strain field and the CH, evidence was found in the support of one of the existing models of CH evolution which implies that the CH appears before the formation of MDs and subsequently MDs form at some troughs in the undulation.

Dedicated to my parents:

Sontosh Kumar Shaha and Alpana Rani Saha

Acknowledgements

First, I would like to offer my sincerest gratitude to one of my supervisors Dr. David A. Thompson for his continuous guidance, advice and encouragement throughout the work. I greatly appreciate for his continuous inspiration, patience and dedication to this work. His deep understanding of the semiconductors was most useful during the growths in MBE and characterizing the samples. He generously let me explore different areas which attracted my attention, examined my data and hypotheses critically, and offered valuable advices. Next, I thank my other supervisor Dr. Daniel Cassidy for his guidance and support throughout the course of this study. He was always there with an open door for all the problems that I faced. Other than these two supervisors, there was Dr. Brad Robinson and Dr. Shahram Ghanad Tavakoli who acted like a pseudo-supervisor during the course of my study.

I also thank Professor Dr. Peter Mascher and Professor Dr. Gianluigi Botton as they always manage their time for me whenever I wanted to discuss about my study. Those discussions were really encouraging and helped me to gain some insight about the physics of the growth.

I also thank Doris for helping me in the clean room, Andy Duft for teaching me how to use atomic force microscopy and Fred Pearson for teaching me to use transmission electron microscopy.

Finally, I am extremely thankful to my parents for their moral support and encouragement. Without their support this thesis would have been impossible.

Table of Contents

Abstract iii
Acknowledgements v
Table of Contents vi
List of Figures viii
List of Tables x
List of Abbreviations xi
Chapter 1 : INTRODUCTION 1
1.1 Motivation 1
1.2 Strained Epitaxy 3
1.3 Polarity of Dislocations in III-V Compound Semiconductors 8
1.4 Theory of Metamorphic Buffer Layers 10
1.5 Outline of the Thesis 11
Chapter 2 : MATERIALS GROWTH AND CHARACTERIZATION 13
2.1 Introduction 13
2.2 Molecular Beam Epitaxy 13
2.3 X-ray Diffraction 15
2.3.1 Lattice Parameter Determination 17
2.3.2 The Glancing Incidence and Glancing Exit Technique 18
2.3.3 Least Square Criterion Method for Lattice Constant Determination 20
2.3.4 Least Square Criterion Method for Lattice Constant Determination 23
2.4 Atomic Force Microscopy 24
2.5 Rapid Thermal Annealing 25
2.6 Photoluminescence 26
2.7 Degree of Polarization 26
2.8 Transmission Electron Microscopy 28
Chapter 3 : EFFECT OF LOW-TEMPERATURE LAYER 30
3.1 Introduction 30
3.2 Previous works 30

3.3 Experimental Procedure 31
3.4 Results and Discussion 33
3.5 Summary 37
Chapter 4 : SURFACE OBSERVATION OF METAMORPHIC-BUFFER 38
4.1 Introduction 38
4.2 Cross-Hatch 38
4.3 Background 40
4.4 Experimental Procedure 43
4.5 Results 44
4.6 Discussion 48
4.7 Summary 52
Chapter 5 : COMPARISON BETWEEN ANION VS. CATION AND LINEAR VS. LOGARITHMIC GRADING 53
5.1 Introduction 53
5.2 Distribution of Misfit Dislocations in graded layers 54
5.3 Background of metamorphic buffer 55
5.4 Sample growth 58
5.5 X-ray analysis 61
5.6 Atomic Force Microscopy (AFM) 65
5.7 Etch Pit Density 68
5.8 Photoluminescence 70
5.9 Degree of Polarization 73
5.10 Transmission Electron Microscopy (TEM) 74
5.11 Conclusion 77
Chapter 6 : Conclusion 79
6.1 Summary 79
6.2 Future Research 80
REFERENCES 82

List of Figures

Fig 1-1: Bandgap vs. lattice-constant plot of the III-V compounds [5]. ... 3
Fig 1-2: Schematic of strained epitaxy (a) Coherent growth and (b) incoherent growth. ... 4
Fig 1-3: The elastic strain energy increases linearly with layer thickness but the energy of misfit dislocation rises slowly [8]. ... 5
Fig 1-4: Theoretical critical thickness of InGaAs/GaAs system (shown by solid line) and the triangle, dotted lines and solid circles are different experimental observations [7]. ... 6
Fig 1-5: Misfit dislocations from the interface terminating at the surface, referred to as threading dislocations [7]. ... 7
Fig 1-6: Effect of strain on bandedges of a direct bandgap material [5]. ... 7
Fig 1-7: The stacking sequence of zinc-blende structure in <111> direction. Atoms with different size indicate that they are not on the same height along the projected direction [10]. ... 8
Fig 1-8: III-V compound semiconductor structure viewed along (a) <1 $\bar{1}$ 0> direction and (b) <110> direction to explain the conventional 'shuffle-set' and 'glide-set' dislocations [10]. ... 9
Fig 1-9: Simplified schematic illustration of the propagation of dislocations through the misfit layers: (a) new MDs originate at each new misfit plane; (b) initial MDs bend over at successive misfit planes leading to a constant density of dislocations as the buffer grows [12]. ... 10
Fig 2-1: Schematic representation of MBE apparatus [14]. ... 14
Fig 2-2: Mosaic structure of a crystal. ... 16
Fig 2-3: Schematic of triple axis high resolution x-ray diffractometer [15]. ... 17
Fig 2-4: Schematic of Bragg law [15]. ... 18
Fig 2-5: Geometries of (a) the glancing incidence and (b) the glancing exit [15]. ... 19
Fig 2-6: Relation between the epitaxial and substrate crystal lattice [18]. ... 24
Fig 2-7: SEM images of Si-cantilever and tip. ... 25
Fig 2-8: Scaning directions for DOP measurement. ... 27
Fig 2-9: Experimental setup for the DOP measurement. ... 28
Fig 3-1: Change of PL peak intensity with annealing temperature. ... 34
Fig 3-2: Blue-shift of PL peak wavelength with annealing temperature ... 35
Fig 3-3: FWHM of PL spectra vs. annealing temperature ... 35
Fig 3-4: Optical microscope image of the sample surface after annealing. ... 36
Fig 3-5: SEM image of the crack lines. ... 37
Fig 4-1: Plot of epilayer thickness vs. misfit in the InGaAs/GaAs system. Cross hatch patterns can be seen in the shaded area [36]. ... 39
Fig 4-2: Optical microscope image of cross-hatch in $In_{0.3}Ga_{0.7}As$ layer grown metamorphically on GaAs (001) substrate ... 40
Fig 4-3: Elastic distortion of vertical lattice planes in a morphologically undulating heteroepitaxial layer under compressive stress [46]. ... 41
Fig 4-4: (a) AFM images of the final layer ($In_{0.3}Ga_{0.7}As$) of metamorphic buffer, (b) 3D view of surface undulation of the same sample shown in (a). ... 45

Fig 4-5: Surface height profile along (a) <110> and (b) <1$\bar{1}$0> directions. Horizontal axis indicates the scan direction (shown upto 16μm) and the vertical axis represents the surface heights in nm (in (a) range is -10 to 10 nm and in (b) range is from -4 to 4 nm. 46
Fig 4-6: Photoluminescence signal from the sample. 47
Fig 4-7: Maps of DOP of the sample (100×100 μm^2). 47
Fig 4-8: omega-2theta curve for the as-grown sample where the beam is incident on [1-10] direction. 48
Fig 4-9: (a) Calculated DOP map for 60° MD [20], (b) example of DOP obtained from the sample. 49
Fig 4-10: Cross sectional TEM bright field image of the sample. 50
Fig 5-1: Variation of strain with layer thickness for linear and logarithmically graded sample.... 60
Fig 5-2: Cross-sectional bright field TEM image of linearly-graded quaternary alloy grown at 500°C. 60
Fig 5-3: (004) ω-2θ x-ray scans around <110> direction for (a) linear $In_xGa_{1-x}As$ and (b) linear $In_{.485}Ga_{.515}As_yP_{1-y}$ metamorphic layers. 62
Fig 5-4: (004) Reciprocal space maps for linearly graded $In_xGa_{1-x}As$ (a) in <110> and (b) in <1$\bar{1}$0> directions; logarithmically graded $In_xGa_{1-x}As$ (c) in <110> and (d) in <1$\bar{1}$0> directions; linearly graded $In_{.485}Ga_{.515}As_yP_{1-y}$ (e) in <110> and (f) in <1$\bar{1}$0> directions and logarithmically graded $In_{.485}Ga_{.515}As_yP_{1-y}$ (g) in <110> and (h) in <1$\bar{1}$0> directions. 64
Fig 5-5: 5x5 μm^2 AFM images of (a) sample 1, (b) sample 2, (c) sample 3 and (d) sample 4. 66
Fig 5-6: 3-D view of 15x15 μm^2 of AFM images for (a) sample 1 and (b) sample 2. 67
Fig 5-7: Optical microscope images of the buffer layers after etching. 69
Fig 5-8: RT-PL spectra from the QW grown above metamorphic buffers. 71
Fig 5-9: Bandgap model for phase separated region. 72
Fig 5-10: Bright field X-TEM images of (a) sample 1, (b) sample 2, (c) sample 3 and (d) sample 4. Left images are for the first few layers and right images are the last few layers. 75
Fig 5-11: Dark field (g=200) XTEM images of (a) sample2 and (b) sample 3. 77

List of Tables

Table 3-1: Structural detail of the samples. LT layer exists for only sample A. 32
Table 3-2: X-ray measurement data.. 33
Table 4-1: Metamorphic structure details 44
Table 5-1: Details of the metamorphic structures grown.. 59
Table 5-2: Structural details of the layers grown on top of meta-substrate. 61
Table 5-3: Results from x-ray analysis 62
Table 5-4: AFM measurement of different parameters. 67
Table 5-5: Etch pit density measurement.. 69
Table 5-6: FWHM of RT-PL spectra.. 70
Table 5-7: Calculation of band-gap difference between 9K and 300K. 72
Table 5-8: Values obtained from DOP scan. 74

List of Abbreviations

Acronyms

AFM	Atomic Force Microscopy
CH	Cross-Hatch
DOP	Degree of Polarization
GSMBE	Gas Source Molecular Beam Epitaxy
LT	Low-Temperature
MBL	Metamorphic Buffer Layer
MD	Misfit Dislocation
MBE	Molecular Beam Epitaxy
PL	Photoluminescence
QW	Quantum Well
RMS	Root Mean Square
RSM	Reciprocal Space Map
RT	Room Temperature
RTA	Rapid Thermal Annealing
TDD	Threading Dislocation Density
TEM	Transmission Electron Microscopy
TPV	Thermo-photovoltaic
UHV	Ultrahigh Vacuum

Chapter 1 : INTRODUCTION

1.1 Motivation

Since the advent of epitaxy in the 1960s, it has become the most important factor for the advancement of electronic and photonic devices. Over the last six decades, many advances have been recorded in semiconductor technology, in fields such as computers, information technology, telecommunications, solar cells, and consumer electronics, and the key driver of this progress has been the ability to grow high quality semiconductor materials to take advantage of novel and complex device designs.

However, one of the key limitations of epitaxy is the need for lattice-matching the device layers to readily available substrates in order to obtain high-quality materials for useful, high-performance devices. A key requirement for device structures grown using epitaxy is that the substrate would act as a seed crystal, from which subsequent, crystal layers, having different energy bandgaps, are grown. Device designs having increasing complexity and functionality can now be realized using lattice-matched heteroepitaxy. Multiple compositions, lattice-matched thick epilayers can be grown on top of a substrate without dislocation. However, the choices for device layer materials are limited based on the choice of the starting substrate due to the lattice matching condition, and thereby limit device designs. Alternatively, pseudomorphic devices, which include thin strained layers which have different lattice constants from the substrate, have opened up new possibilities, such as high electron mobility transistors [1] and efficient III-V Quantum well (QW) lasers operating over broader wavelength range [2]. As the thickness of strained layers are constrained by the critical thickness limit, the bulk of the high performance device layers still require to be lattice-matched to the substrate or defect generation will degrade the device performance. Thus the fundamental problem of growing high-quality lattice-mismatched materials still exists.

Therefore, after six decades of epitaxy, device designs are to a large extent still limited by the availability of the substrates. In fact, today's semiconductor industry focus on yield, cost and scalability which means that the size of available substrates has become another important consideration. Thus a high-quality single crystal wafer may no longer be sufficient for industry to adopt it as a viable platform for a given application, if the wafers cannot be made large enough. For example, thermoelectric and mid-IR devices are generally grown on InAs or GaSb wafers. But due to the smaller size of the substrates (typically 3-inch diameter), these devices are of high cost and hence of limited commercial interest.

Moreover, the constraint of lattice constant is also one of the major obstacles to obtain optimized triple junction solar cells. At present, the most efficient triple junction solar cell has the bandgap profile of InGaP(1.86 eV)/$In_{0.01}Ga_{0.99}As$(1.40eV)/Ge(0.65eV), which is lattice matched with a Ge substrate [3]. The conversion efficiency for this combination has reached around 30%. However, theoretical analysis showed that the conversion efficiency can be increased to 39% by replacing the $In_{0.01}Ga_{0.99}As$ cell by the $In_{0.16}Ga_{0.84}As$ (1.2 eV) cell [4]. Using this composition would produce strain in the region of growth and hence nucleate dislocations, which would reduce the conversion efficiency severely.

Thus, the work in this thesis is devoted to overcome the lattice-matching constraint, so that new materials can be grown whose lattice constant is different from any of the available substrates. That goal can, in principle, be achieved by using metamorphic graded buffers as the means to controllably change the spacing of atoms while preserving the crystal quality. This graded buffer can then be used as a "pseudo-substrate" with the modified lattice-constant on which subsequent epitaxial layers with the desired electronic properties can be grown. The lattice-matching constraint of epitaxy could then be relaxed enabling a wider choice of materials that should allow more optimal design choice. It is evident from Fig 1-1 that the III-V semiconductor materials span a wide range of lattice constants and bandgaps. But commercially available substrates (Si, Ge, GaAs, InP, GaSb

and InAs) provide a limited range of lattice constants and restricts the epitaxial growth to a narrow range of ternary and quaternary alloys. With the development of metamorphic graded buffer technology wide parameter space will be opened up.

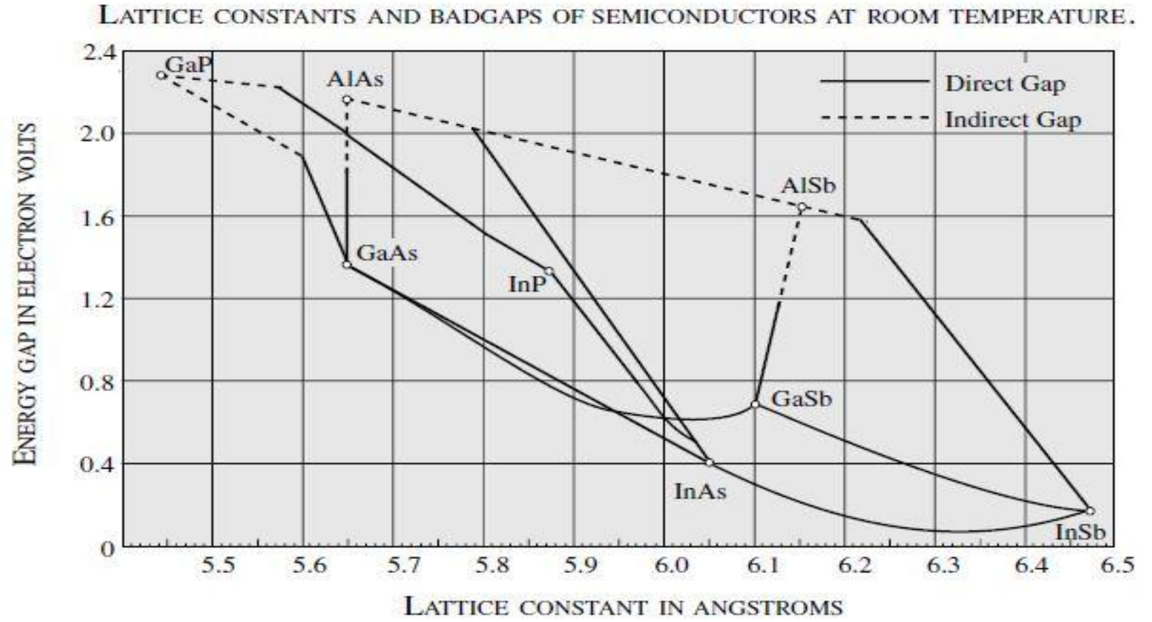

Fig 1-1: Bandgap vs. lattice-constant plot of the III-V compounds [5].

For the purpose of this work, only compressive metamorphic buffers (strain of ~1.37%) grown on the GaAs substrate, have been studied. The goal of this work is to investigate some possible approaches to improve the metamorphic buffers (MBs). Therefore, it is important to know how to judge the quality and usefulness of the graded buffers. The quality of the pseudo-substrates was determined by threading dislocation densities (TDDs), surface roughness, mosaicity and photoluminescence measurements.

1.2 Strained Epitaxy

Before going into the details of graded buffer approach it is useful to review the fundamentals of strained epitaxy. Strained epitaxy occurs when the epitaxial layers have a different lattice constant from the host substrate. Consider that the lattice constants of the epilayer and the substrate are a_L and a_s, respectively. Then the mismatch, f, which is defined as [5]

$$\boldsymbol{f = \frac{a_s - a_L}{a_L} = \varepsilon + \delta} \qquad \text{Equation 1-1}$$

arises, which is accommodated by the sum of elastic strain, ε, and the plastic strain, δ. Elastic strain is accommodated by tetragonal distortion of crystal lattice (shown in Fig 1-2(a)) and plastic strain is accommodated by forming line-defects known as misfit dislocations (MDs) (shown in Fig 1-2(b)). The energy of forming a dislocation is generally greater than that required for small distortions of atomic bonds. Thus in strained epitaxy, the film will undergo elastic deformation initially. As the thickness (h) of the strained film increases, the elastic strain energy also increases ($E_{strain} \propto h$). But the dependence of plastic energy with thickness is weak ($E_{dislocation} \propto \ln(h)$). Hence after growing the strained layer up to a certain thickness, the elastic energy will exceed the plastic energy and thus would favor the formation of MDs. The thickness of the film at which this happens is known as critical thickness, h_c. The growth is called coherent if no dislocation forms and incoherent if the MDs form to accommodate the misfit strain.

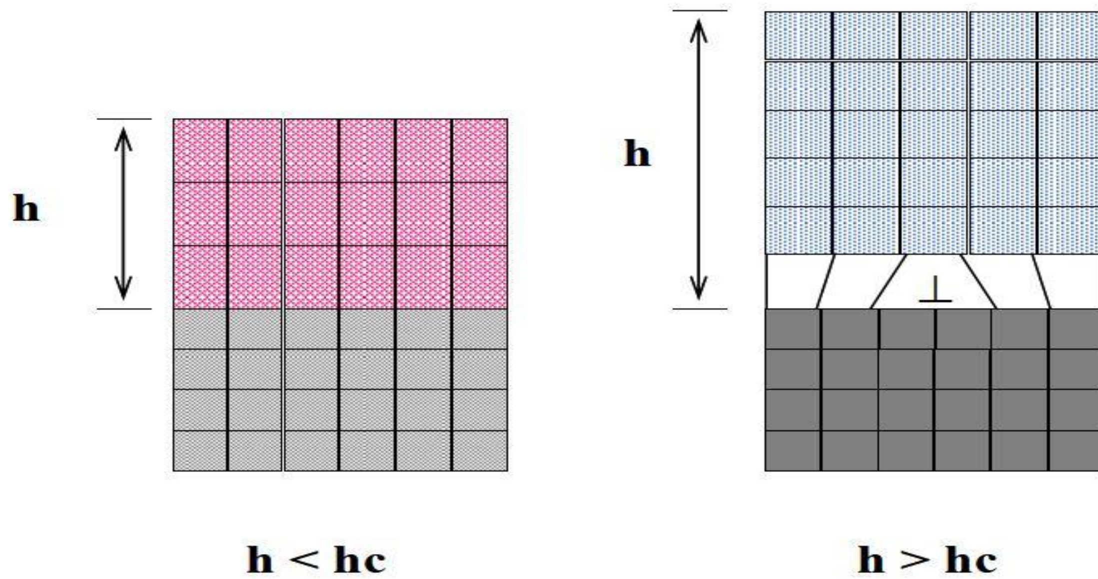

Fig 1-2: Schematic of strained epitaxy (a) Coherent growth and (b) incoherent growth.

The concept of critical thickness is schematically shown in Fig 1-3, which shows that elastic strain is smaller than energy of dislocation formations when epilayer thickness is less than h_c and it becomes larger when epilayer thickness is greater than h_c. The

mathematical expression for critical thickness was developed by Mathews and Blakeslee [6] using a force balance approach and modified by Fitzgerald [7]

$$\boldsymbol{h_c} = \frac{D(1-\vartheta cos^2\alpha)[ln(\frac{h_c}{b})+1]}{Yf} \qquad \text{Equation 1-2}$$

where, D is the average shear modulus of the film and underlying substrate. $\boldsymbol{\vartheta}$, b and Y are the Poisson's ratio, Burgers vector and Young's modulus of the film, respectively. α is the angle between the Burgers vector and line vector of the dislocation. For the 60° dislocations, that are initially formed in the case of III-V semiconductors, α=60°. From equation 1-2, it can be seen that critical thickness decreases rapidly with the misfit strain. The plot of critical thickness vs. In mole fraction for InGaAs epilayer grown on GaAs substrate is shown in Fig 1-4.

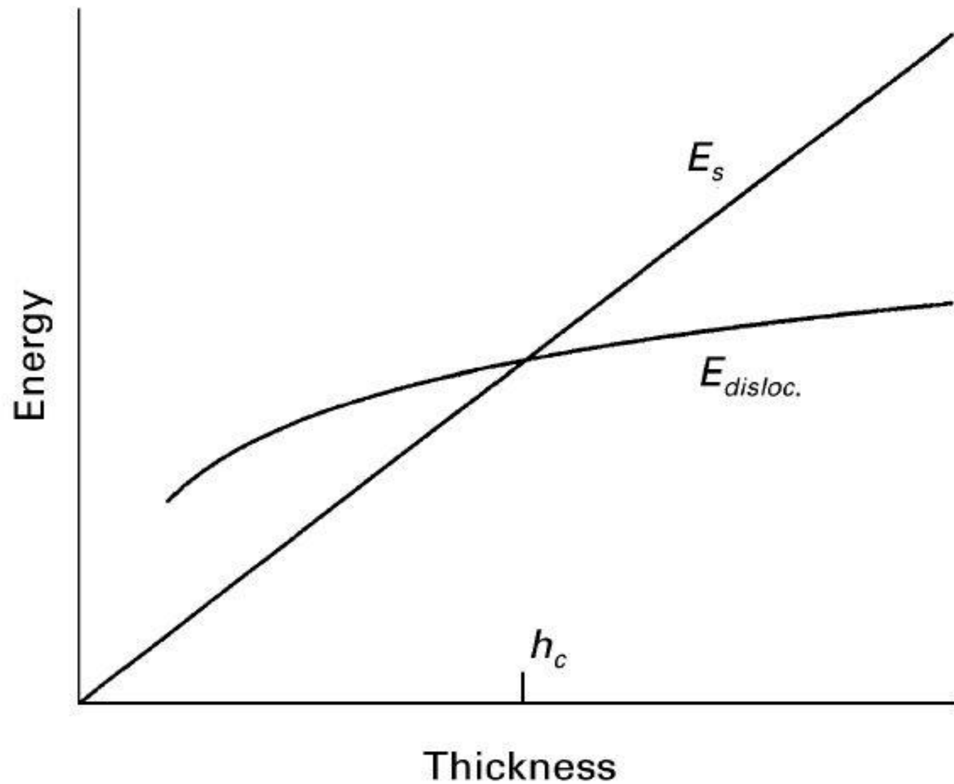

Fig 1-3: The elastic strain energy increases linearly with layer thickness but the energy of misfit dislocation rises slowly [8].

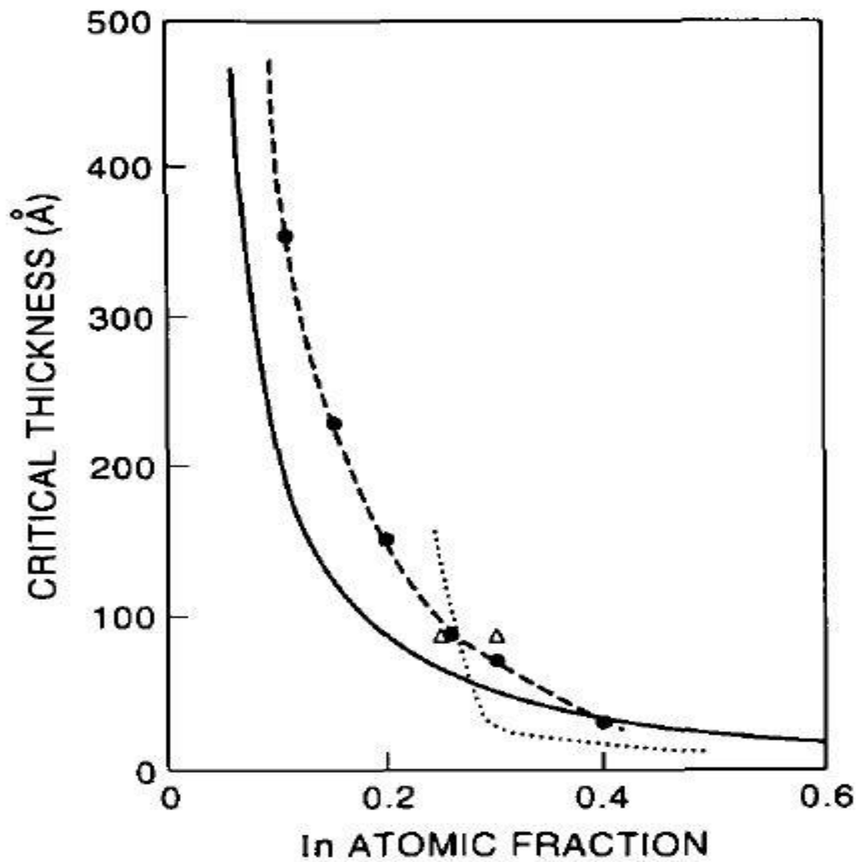

Fig 1-4: Theoretical critical thickness of InGaAs/GaAs system (shown by solid line) and the triangle, dotted lines and solid circles are different experimental observations [7].

From Fig 1-4, it can be seen that theoretical critical thickness is lower than the experimentally determined values. This is due to the kinetics of dislocation nucleation and glide, which are thermally-activated processes, and a typical growth temperature is not enough for efficient generation and glide of dislocations [9]. Once dislocations are formed, they can only terminate at a free surface [10]. Therefore, the MDs have to extend along the film/substrate interface or make their way through the film to the top surface. These latter dislocations are known as threading dislocations (TDs). As TDs thread through the epitaxially grown films, they will pass through the device active layers (shown in Fig 1-5) and can serve as strong carrier scattering and non-radiative recombination centers [11]. It is therefore important to keep threading dislocation density (TDD) as low as possible.

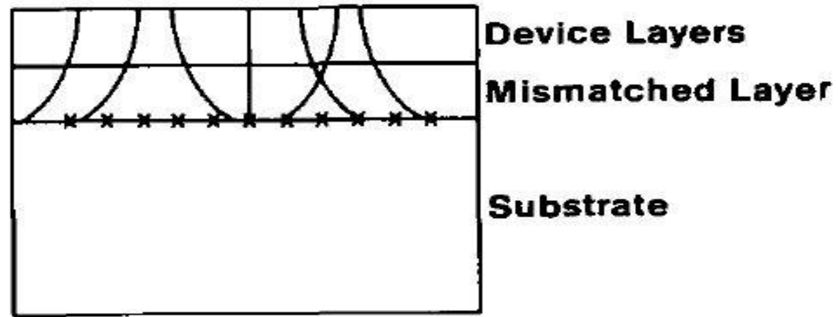

Fig 1-5: Misfit dislocations from the interface terminating at the surface, referred to as threading dislocations [7].

The bandgap of an epilayer is also modified by the strain [5]. In an unstrained, bulk semiconductor, the light hole (LH) and heavy hole (HH) bands are degenerate at the Brillouin zone center and a spin split-off band lies lower in energy. For a strained system, HH and LH bands become non-degenerate. For a biaxial compressive strained layer, the HH state is above the LH state. On the other hand, biaxial tensile strain reduces the bandgap and the LH state is above the HH state. These changes of bandgaps are shown in Fig 1-6, where the horizontal axis represents the wave vector and vertical axis represents the electron energy.

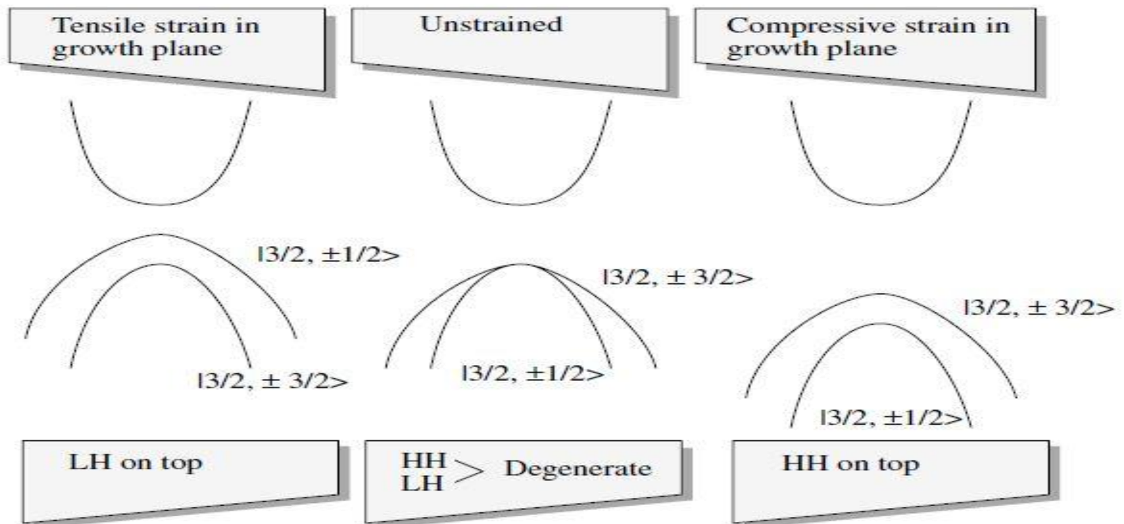

Fig 1-6: Effect of strain on bandedges of a direct bandgap material [5].

1.3 Polarity of Dislocations in III-V Compound Semiconductors

III-V compound semiconductors have the zinc-blende structure. Its stacking sequence in <111> direction is ⋯AaBbCcAa⋯ (shown in Fig 1-7, <111> is normal to the plane of the figure) where A, B, C are group III atoms and a, b, c are group V atoms. The spacing between aB, bC, cA is shorter than Aa, Bb, Cc. Typical Burger's vector for (001) substrate is 1/2<110> and the most common slip planes are (111) planes.

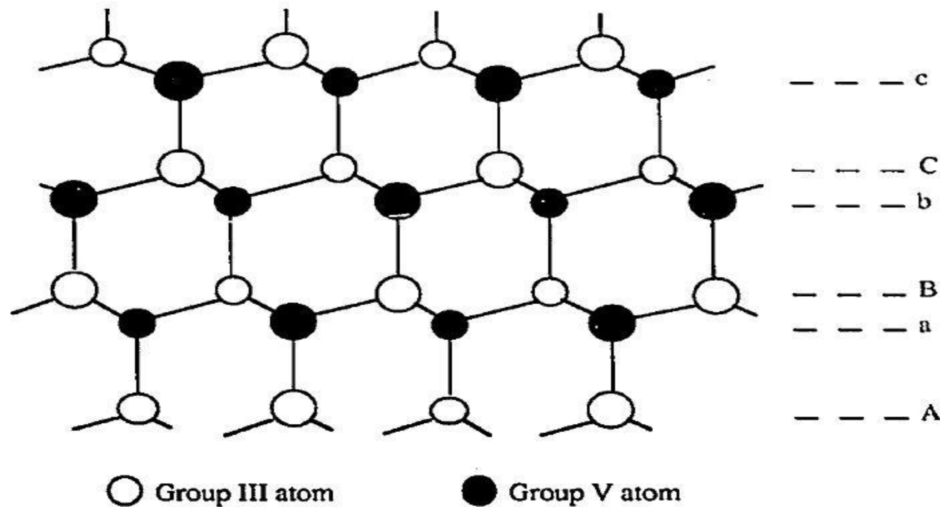

Fig 1-7: The stacking sequence of zinc-blende structure in <111> direction. Atoms with different size indicate that they are not on the same height along the projected direction [10].

Fig 1-8 shows the zinc-blende structure viewed along two orthogonal <110> directions. A dislocation is introduced by removing some material from the crystal. In Fig 1-8, material can be removed either along 1-2-3-4 or along 1-5-6-4. Although, conventionally it was believed that the cut is made along 1-2-3-4, due to the widely spaced III-V bonds, it was shown later that for III-V semiconductors most of the dislocations are made by the cut along 1-5-6-4, as they are found to be able to move more readily [10]. The dislocations associated with 1-2-3-4 cut and 1-5-6-4 cut is called 'shuffle-set' and 'glide-set' dislocations, respectively. The type of the core of the dislocations (group III or V) depends on which way the cut is made. Both shuffle-set cut 1-2-3-4 and glide-set cut 1-5-6-4 give α dislocation in Fig 1-8 (a) and β dislocation in Fig 1-8 (b).

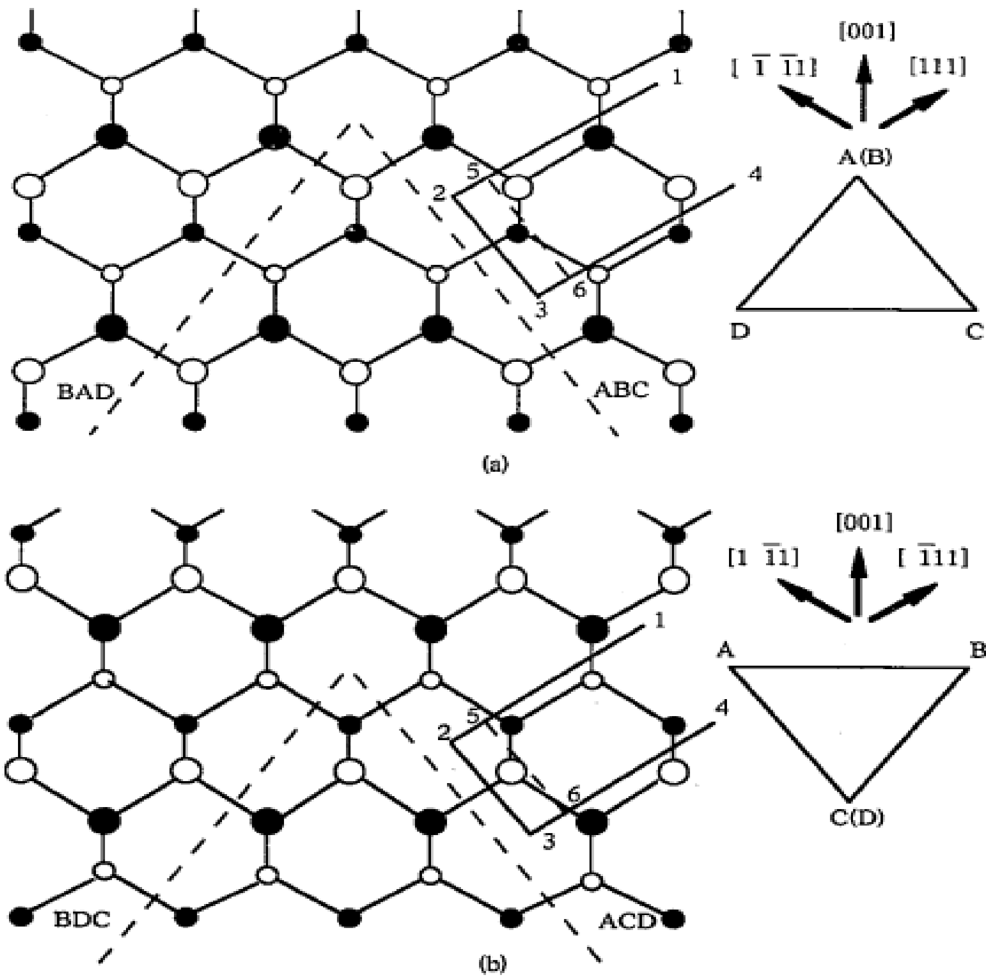

Fig 1-8: III-V compound semiconductor structure viewed along (a) <1$\bar{1}$0> direction and (b) <110> direction to explain the conventional 'shuffle-set' and 'glide-set' dislocations [10].

The above concept of dislocation polarity can be applied to MDs. For compressively strained films α-dislocations are along <1$\bar{1}$0> direction and β-dislocations are along <110> direction. As for III-V semiconductors, the dislocations are mainly glide-type [7]. α-dislocations have group V core and β-dislocations have group III core. Thus the MDs along <1$\bar{1}$0> and <110> directions are different in nature.

1.4 Theory of Metamorphic Buffer Layers

A key metric of the quality of pseudo-substrates is the TDD and surface roughness. Metamorphic buffer layers (MBLs) are grown to obtain a pseudo-substrate which will have the desired lattice constant, on which to grow subsequent device layers, with low TDD. Metamorphic growth is initiated on a standard substrate and the composition is varied either gradually or in steps in order to achieve a final different lattice constant. As the goal is to achieve a relaxed layer as a pseudo-substrate, the formation of dislocations is desired. Thus for a graded buffer system, multiple misfit planes will exist. Two types of dislocation movements can occur in these layers (shown in Fig 1-9) [12]. In the first case, each misfit plane will give rise to new MDs and dislocation density will continually increase as the buffer grows (Fig 1-9(a)). In the second case, despite of forming new MDs at each new misfit plane, when the dislocations from previous layers reach the misfit plane they will bend over into the misfit plane to relieve the mismatch stress there (Fig 1-9(b)). The latter is more energetically favorable since no new dislocations need to be formed and the total dislocation density is lowered.

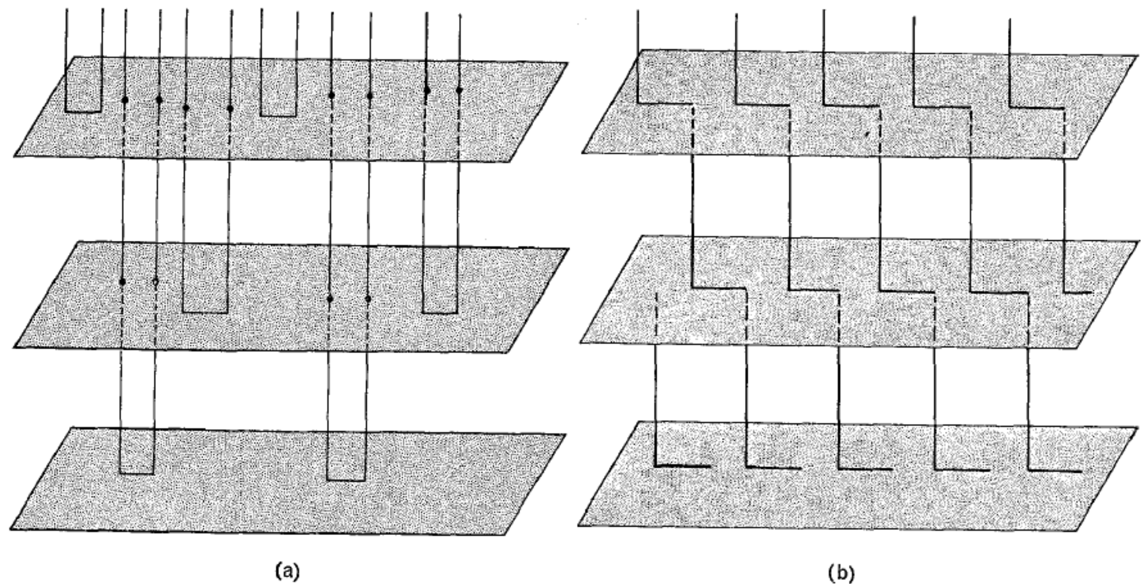

Fig 1-9: Simplified schematic illustration of the propagation of dislocations through the misfit layers: (a) new MDs originate at each new misfit plane; (b) initial MDs bend over at successive misfit planes leading to a constant density of dislocations as the buffer grows [12].

Since dislocations must terminate at a free surface or close upon themselves in the form of a dislocation loop and the target is to obtain a pseudo-substrate with low TDD, dislocations need to end at the edge of the substrate in an interface and high glide velocity is required to achieve this goal. This is done by varying the grading rate slowly and therefore adding strain to the system in a controllable fashion. Thus dislocations nucleate in an orderly fashion over the volume of the MBLs. As relatively few dislocations are needed to relieve strain at any one time, optimal recycling of threading dislocations can be achieved, which reduces the need to nucleate MDs. A high growth temperature is maintained during the growth and this leads to greater glide velocity [7]. This also leads to the formation of longer MDs and, therefore, allows fewer MDs to relieve the same amount of mismatch and maximizes their probability to glide towards the edges and terminate there. However, as the nucleation of dislocations is also a thermally activated process, too high a growth temperature can lead to the formation of excess dislocations which is not desired. Therefore, an optimized growth temperature is required.

The nucleation and glide of dislocations are related to each other. Controlled nucleation of dislocations reduces the chance of the interaction among themselves, which in turn reduces the likelihood of pile-up of dislocations which are unable to glide and lead to the formation of threading dislocations. On the other hand, a higher glide velocity produces longer MDs and therefore reduces the number of dislocations required to relieve similar mismatch. All of these help to keep TDD to a minimum.

1.5 Outline of the Thesis

The thesis has altogether six chapters. Chapter 1 discussed the need of a pseudo-substrate with different lattice parameters and the method to achieve this. The theory of MBLs is also discussed.

Chapter 2 will describe the epitaxial growth process used for this work and provide details about the experimental tools used in this research. Chapter 3 will discuss the effect of growing an underlying low-temperature layer before initiating metamorphic growths. The effect of annealing on the buffers over a temperature range of 650-900°C is

investigated. Chapter 4 explores the surface features of the pseudo-substrate. Evolution of the well-known cross-hatch morphology will be discussed. In Chapter 5, comparison is done between a logarithmic and linear grading approach and also ternary and quaternary buffer layers. That chapter will describe the crystal quality, optical luminescence quality and surface morphology of the pseudo-substrates. Chapter 6 will conclude the thesis with a compendium of the major findings of the present research and suggest future research projects.

Chapter 2 : MATERIALS GROWTH AND CHARACTERIZATION

2.1 Introduction

This Chapter will discuss about the growth and characterization of the engineered materials grown in this work. All growths were done using gas source molecular beam epitaxy (GSMBE).

Several techniques were employed to characterize the structural and optical quality of the grown films, including x-ray diffraction (XRD), cross-sectional transmission electron microscopy (X-TEM), atomic force microscopy (AFM), photoluminescence (PL), degree of polarization (DOP), optical microscopy and chemical etching for determining etch-pit density.

2.2 Molecular Beam Epitaxy

Epitaxy is defined as the deposition of a crystalline overlayer on a crystalline substrate. In order to grow an epitaxial layer, it is important to have similar crystal symmetry between the epilayer and substrate. Molecular beam epitaxy (MBE) was used as a technique of epitaxial growth in this work. In MBE, epitaxial layers are grown by the reactions of several molecular or atomic beams on a heated substrate surface under ultrahigh vacuum (UHV) ($\sim10^{-8} - 10^{-10}$ torr). The UHV environment is necessary to ensure that the rate of impact on the substrate surface of residual gas molecules in the MBE chamber is insignificant relative to the rate of deposition of the source molecules and atoms effusing from their sources, ensuring a low impurity concentration in the epilayer, while also eliminating interactions between beam components and gas molecules during transit. Thus samples grown in MBE have high material quality [13]. The reason behind the popularity of MBE techniques among crystal growers is the intrinsic feasibility of controlling the profile of the composition and doping of the

growing structure at the monolayer level. A schematic representation of the MBE is illustrated in Fig 2-1.

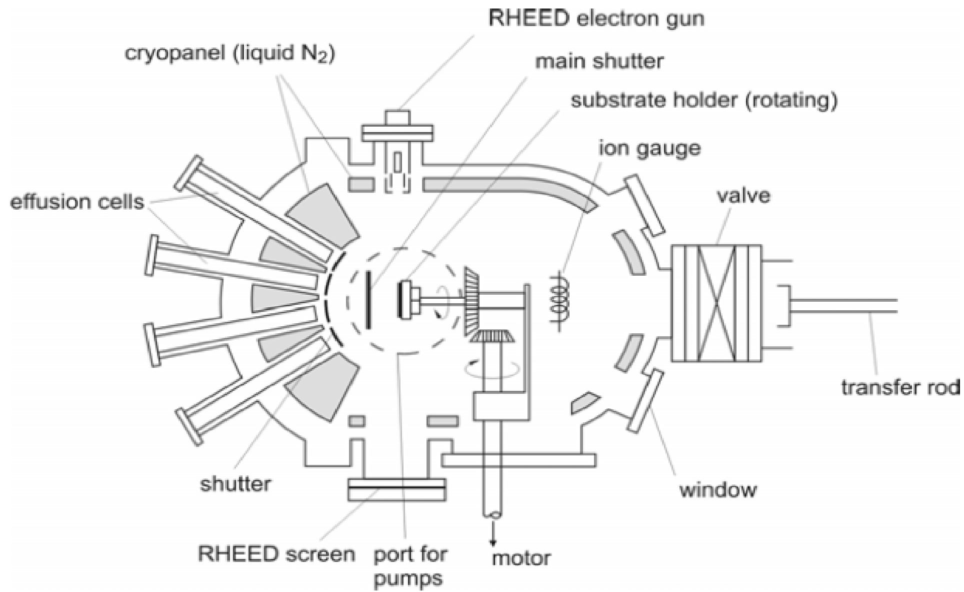

Fig 2-1: Schematic representation of MBE apparatus [14].

All the samples were grown by a GSMBE system manufactured by SVT Associates. Evaporation sources were used for the group III (In and Ga) elements. The group V (As and P) elements were deposited as dimers produced using AsH_3 and PH_3, which were dissociated to form As_2 and P_2 dimers, by passing the gases over a hot filament at 950°C. These dimers dissociate while bonding to the group III elements on the sample surface. The group III fluxes were adjusted by controlling the temperature of the respective sources, which in turn controls the group III layer composition and the layer growth rate. The group V composition was controlled by adjusting the gas flow rates separately, while taking into account the different sticking coefficients of the two dimers.

The GSMBE system, used for this experiment, consists of a stainless steel loading chamber, a transfer and preparation chamber and a growth chamber. The growth chamber

is maintained at an UHV environment by using a combination of turbo-pump and cryo-pump. Liquid nitrogen cryopanels surround the interior of the growth chamber to minimize re-evaporation from the internal walls and maintain thermal isolation between the cells. The geometry of the system is such that the sources provide an upward directed flux upon a downward facing substrate. An optical pyrometer was used for monitoring the substrate temperature during growth. The fluctuation of temperature profile obtained can also provide information on surface roughness.

The MBE growths were performed on 2-inch diameter, epiready, (001)±0.1°, Si-doped ($n = 10^{18}$ cm^{-3}) GaAs substrates provided by Wafer Technology Ltd. All layers were grown at a nominal growth rate of 1 μm/hr. During growth, the substrate holder was rotated at a frequency of ~15 rpm. The substrates were initially degassed at 300°C for ~15 minutes. Upon loading in the growth chamber the substrate surface was initially cleaned in-situ to remove the native oxide using a hydrogen plasma. A flux of As_2 was maintained to compensate any evaporative loss during cleaning procedure. The As_2 flux was maintained at 3 sccm, while growing GaAs or InGaAs. During the growth of InGaP or InGaAsP, group V flux was maintained at 4 sccm.

2.3 X-ray Diffraction

X-rays were discovered in 1895 by the German physicist Roentgen and were so named because their nature was unknown at the time. For crystalline semiconductor epilayers, X-ray diffraction (XRD) is a common and powerful ex-situ technique to characterize structural properties in a non-destructive fashion. Typically, XRD is used to determine lattice constants, strain, mosaicity of the epilayers and tilt information. Mosaicity is known as a kind of crystal imperfection into which a “single” crystal is broken up in an enormously exaggerated fashion (shown in Fig 2-2). All real crystals possess this type of imperfection to a lesser or greater degree. A crystal with mosaic structure does not have its atoms arranged on a perfectly regular lattice extending from one side of the crystal to the other; instead, the lattice is broken up into a number of tiny blocks, each slightly disoriented one from another.

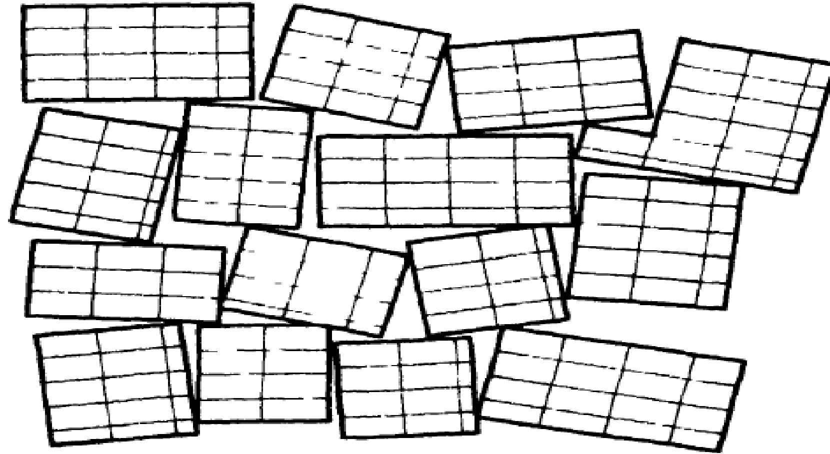

Fig 2-2: Mosaic structure of a crystal.

A BEDE D1 triple axis diffractometer was used for this work. A 50 µm slit and a two bounce asymmetric Si monochromator was used to condition the Cu-Kα_1 (λ = 1.54056 Å) X-ray beam. An analyzer crystal was used in front of the detector to improve the resolution at the expense of intensity. Fig 2-3 shows a schematic of triple axis high resolution x-ray diffractometer.

The ω-2θ (ω is the angle that the incoming beam makes with the sample surface, 2θ is the angle between diffracted and incoming beam) scans, at $\omega_{rel} = 0$ (ω_{rel} is the tilt of the sample with respect to the substrate), were performed to obtain strain information. The source is kept fixed and the sample is rotated. During rotation through an angle $\delta\omega$ the detector is rotated by twice this amount in the same direction. Reciprocal space maps (RSM) were carried out to obtain the information about tilt and mosaicity of the epilayer. A convenient approach to obtain RSM is to perform a loop scan in which the specimen is set at a particular angle and then a ω-2θ scan is performed. After that the specimen position (ω_{rel}) will be incremented and another ω-2θ scan will be performed. After collecting all the ω-2θ scans for a range of ω_{rel} values, software is used to convert the data in reciprocal space coordinates.

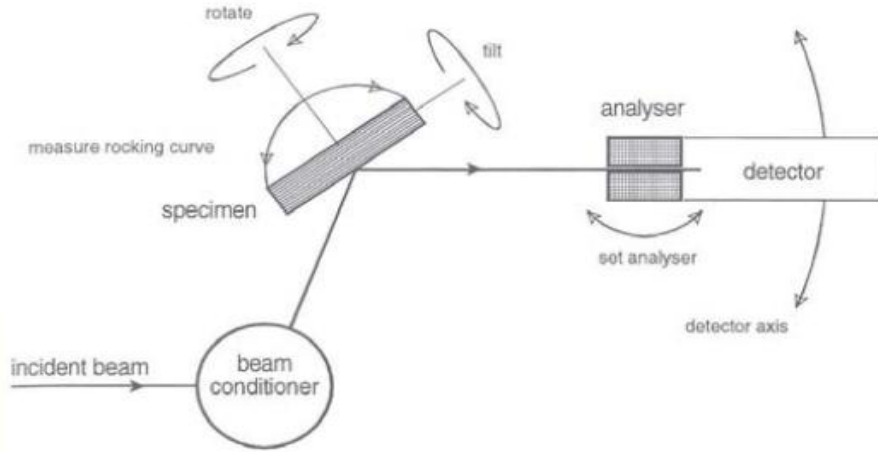

Fig 2-3: Schematic of triple axis high resolution x-ray diffractometer [15].

For XRD scans, the 2-inch diameter wafers were cleaved into quarters. One quarter of the wafer was mounted with beam direction parallel to <110> and then <1$\bar{1}$0>. All scans were done by applying voltage of -40kV and current of 30mA to the x-ray source.

2.3.1 Lattice Parameter Determination

For the characterization of compound semiconductor epilayers, it is important to determine both the in-plane and out-of-plane lattice constants, as it will provide information about composition and strain (or tetragonality of the unit cell).

Since the coherent as-grown epitaxial layers were under strain, tetragonal distortion makes the in-plane and the out-plane lattice parameters unequal. For simplicity, the two perpendicular in-plane lattice constants were assumed equal ($a_x = a_y$) and different from the lattice constant in the growth direction ($a_x = a_y \neq a_z$). The lattice parameters were determined by calculating the d-spacing (d_{hkl}) of the hkl planes, deduced from the peak separation in the rocking curves. For orthorhombic crystals ($a_x \neq a_y \neq a_z$), d_{hkl} is [15]

$$d_{hkl} = \frac{1}{\sqrt{\frac{h^2}{a_x^2} + \frac{k^2}{a_y^2} + \frac{l^2}{a_z^2}}} \qquad \text{Equation 2-1}$$

where a_x, a_y and a_z are the lattice constants and h, k and l are the Miller indices of the corresponding planes. The value of d-spacing is obtained by the well-known Bragg's law [15]

$$d_{hkl} = \frac{\lambda}{2\text{Sin}\theta_B} \qquad \text{Equation 2-2}$$

where λ is the wavelength of the X-rays and θ_B is the Bragg angle of incidence. The Bragg angle is defined as the angle between an incident x-ray beam and a set of crystal planes for which the secondary radiation displays maximum intensity as a result of constructive interference. Fig 2-4 illustrates Bragg's law and all related parameters.

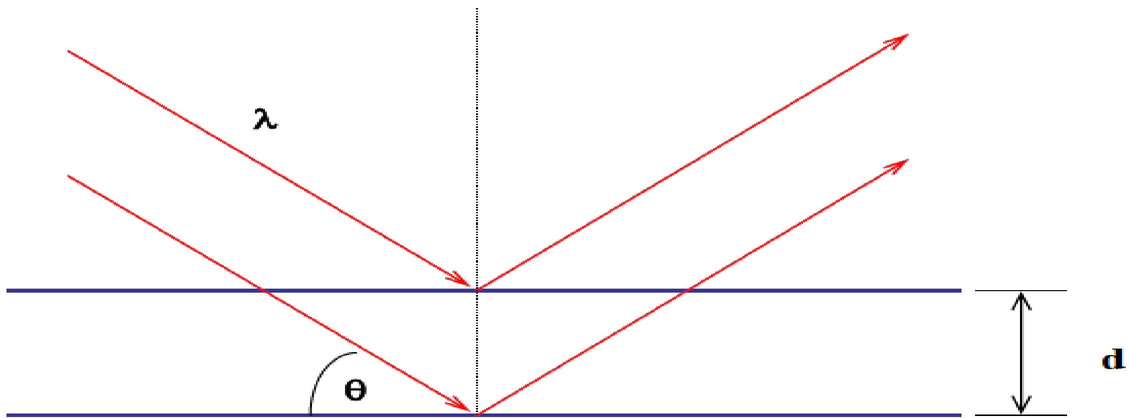

Fig 2-4: Schematic of Bragg law [15].

A (004) reflection rocking curve was performed to determine the lattice constant in the growth direction (a_z) for the epilayers grown on (001) substrate. Since the rocking curve gives the value of θ_B for the epilayers, the calculation of a_z is straightforward from equation 2-1 and equation 2-2.

2.3.2 The Glancing Incidence and Glancing Exit Technique

Depending on diffraction planes, x-ray diffraction can be divided into two categories, symmetric (e.g. (004)) orientations, where the diffraction planes are parallel to the surface, and asymmetric (e.g. (224)) orientations, where the diffraction planes are not parallel to the surface. While symmetric diffraction gives information only about

perpendicular lattice constant, asymmetric diffraction contains information about both in-plane and out of plane lattice constants. Since there always exist two similar sets of diffraction planes, with the same spacing in a crystal, two geometries of asymmetric diffraction named glancing incidence (G_{inc}) and glancing exit (G_{exit}), can be used to measure the lattice constants of the epilayer. Fig 2-5 demonstrates the geometries for G_{inc} and G_{exit} diffraction techniques. ϕ is the angle between the reflecting planes and the surface of the substrate and called the acute angle.

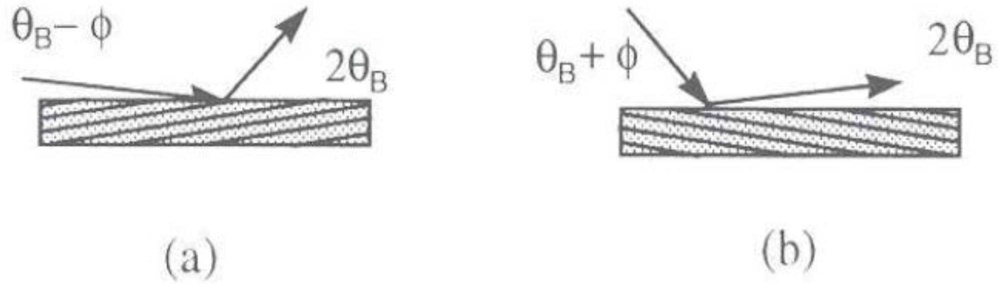

Fig 2-5: Geometries of (a) the glancing incidence and (b) the glancing exit [15].

Due to the change in lattice constant and tetragonal distortion, values of θ_B and ϕ changes from the substrate values. By solving trigonometric and algebraic equations in-plane ($a_x \equiv a_{epi}$) and out-of-plane ($a_z \equiv c_{epi}$) lattice constants could be found. Consider that $\delta\theta_{inc}$ and $\delta\theta_{exit}$ are the differences between the peak of the epilayer and substrate obtained from G_{inc} and G_{exit} diffraction, respectively and $\delta\phi$ is the difference of acute angle between substrate and epilayer. The following equations allow calculation of the Bragg angle and acute angle of the epilayer [15].

$$\delta\theta_{inc} = \delta\theta_B + \delta\phi \text{ and } \delta\theta_{exit} = \delta\theta_B + \delta\phi$$

$$\Rightarrow \begin{cases} \delta\theta_B = \frac{\delta\theta_{inc}+\delta\theta_{exit}}{2} \\ \delta\phi = \frac{\delta\theta_{inc}-\delta\theta_{exit}}{2} \end{cases} \quad \text{Equation 2-3}$$

where $\delta\theta_B$ is the difference between the epilayer and substrate Bragg angles. Since θ_{sub} and ϕ_{sub} are known, the calculation of θ_{epi} and ϕ_{epi} is straightforward. Ref. [15] showed that

$$c_{epi} = \frac{l\lambda}{2Sin\theta_{epi}cos\phi_{epi}} \text{ and } a_{epi} = \frac{\lambda.\sqrt{h^2+k^2}}{2Sin\theta_{epi}sin\phi_{epi}}$$

Once the in-plane lattice constant of the epilayer is determined, the relaxation of the epilayer can be found as [15]

$$R = \frac{a_l - a_s}{a_l^R - a_s} \times 100$$

where a_l^R, a_s and a_l are lattice constants of the fully relaxed epilayer obtained from Vegard's law, the substrate and strained epilayer, respectively. If there is no residual strain in the epilayer ($a_l^R = a_l$), relaxation will be 100%. Vegard's law for lattice constant of $In_xGa_{1-x}As_yP_{1-y}$ is

$$a\,(In_xGa_{1-x}As_yP_{1-y}) = (1-x)(1-y).a_{GaP} + (1-x)y.a_{GaAs} + x(1-y).a_{InP} + xy.a_{InAs}$$

2.3.3 Least Square Criterion Method for Lattice Constant Determination

The lattice constant calculation is not mutually consistent with different combinations of symmetric and asymmetric diffraction planes. To deal with this inconsistency Fatemi [16] proposed a refinement technique using least square criterion. The term "refinement technique" comes in the sense that each measurement is modified by small amount to make it consistent with the other. In this technique, the measured inter-plane distances, d_{hkl}, are slightly adjusted to get the consistency. Let us consider 'a' denotes the two in-plane lattice constants of the epilayer and 'c' denotes the epilayer lattice constant in the growth direction. X-ray rocking curves are obtained for four different diffraction planes. For brevity, we assume the following

$$A = \frac{1}{a^2};\ C = \frac{1}{c^2};\ P = \frac{1}{d^2_{h_1k_1l_1}};\ Q = \frac{1}{d^2_{h_2k_2l_2}};\ R = \frac{1}{d^2_{h_3k_3l_3}} \text{ and } S = \frac{1}{d^2_{h_4k_4l_4}}$$

Thus equation 2-1 can be written for four arbitrary reflections as

$$P = (h_1^2 + k_1^2)A + l_1^2C$$

$$Q = (h_2^2 + k_2^2)A + l_2^2C$$

$$R = (h_3^2 + k_3^2)A + l_3^2C$$

$$S = (h_4^2 + k_4^2)A + l_4^2C$$

It is assumed then that the measured peak separations can be adjusted by small, initially unknown amounts, so that they would result in consistent solutions for ‘a’ and ‘c’. The adjustment would affect P, Q, R and S and can therefore be written as fractional changes p, q, r and s, respectively.

$$P(1+p) = (h_1^2 + k_1^2)A + l_1^2C$$

$$Q(1+q) = (h_2^2 + k_2^2)A + l_2^2C$$

$$R(1+r) = (h_3^2 + k_3^2)A + l_3^2C$$

$$S(1+s) = (h_4^2 + k_4^2)A + l_4^2C$$

Since there are six unknown variables and four equations, two more equations are required for solving them. Hence, least square criterion is applied to put a constraint upon p, q, r and s. The criteria can be stated as

$$p^2 + q^2 + r^2 + s^2 = \text{minimum}$$

Upon differentiation with respect to A and C,

$$\begin{cases} 2p\dfrac{\delta p}{\delta A} + 2q\dfrac{\delta q}{\delta A} + 2r\dfrac{\delta r}{\delta A} + 2s\dfrac{\delta s}{\delta A} = 0 \\ 2p\dfrac{\delta p}{\delta C} + 2q\dfrac{\delta q}{\delta C} + 2r\dfrac{\delta r}{\delta C} + 2s\dfrac{\delta s}{\delta C} = 0 \end{cases}$$

$$=> \begin{cases} \dfrac{p(h_1^2 + k_1^2)}{P} + \dfrac{q(h_2^2 + k_2^2)}{Q} + \dfrac{r(h_3^2 + k_3^2)}{R} + \dfrac{s(h_4^2 + k_4^2)}{S} = 0 \\ \dfrac{pl_1^2}{P} + \dfrac{ql_2^2}{Q} + \dfrac{rl_3^2}{R} + \dfrac{sl_4^2}{S} = 0 \end{cases}$$

Rearranging the equation into matrix format results in

$$Pp - (h_1^2 + k_1^2)A - l_1^2C = -P$$

$$Qq - (h_2^2 + k_2^2)A - l_2^2C = -Q$$

$$Rr - (h_3^2 + k_3^2)A - l_3^2C = -R$$

$$Ss - (h_4^2 + k_4^2)A - l_4^2C = -S$$

$$\frac{p(h_1^2 + k_1^2)}{P} + \frac{q(h_2^2 + k_2^2)}{Q} + \frac{r(h_3^2 + k_3^2)}{R} + \frac{s(h_4^2 + k_4^2)}{S} = 0$$

$$\frac{pl_1^2}{P} + \frac{ql_2^2}{Q} + \frac{rl_3^2}{R} + \frac{sl_4^2}{S} = 0$$

The matrices obtained from these equations are as follows

$$\begin{bmatrix} P & 0 & 0 & 0 & -(h_1^2 + k_1^2) & -l_1^2 \\ 0 & Q & 0 & 0 & -(h_2^2 + k_2^2) & -l_2^2 \\ 0 & 0 & R & 0 & -(h_3^2 + k_3^2) & -l_3^2 \\ 0 & 0 & 0 & S & -(h_4^2 + k_4^2) & -l_4^2 \\ \frac{(h_1^2+k_1^2)}{P} & \frac{(h_2^2+k_2^2)}{Q} & \frac{(h_3^2+k_3^2)}{R} & \frac{(h_4^2+k_4^2)}{S} & 0 & 0 \\ \frac{l_1^2}{P} & \frac{l_2^2}{Q} & \frac{l_3^2}{R} & \frac{l_4^2}{S} & 0 & 0 \end{bmatrix} \begin{bmatrix} p \\ q \\ r \\ s \\ A \\ C \end{bmatrix} = \begin{bmatrix} -P \\ -Q \\ -R \\ -S \\ 0 \\ 0 \end{bmatrix} \qquad \text{Equation 2-4}$$

Rearranging equation 2-4

$$\begin{bmatrix} p \\ q \\ r \\ s \\ A \\ C \end{bmatrix} = \begin{bmatrix} P & 0 & 0 & 0 & -(h_1^2 + k_1^2) & -l_1^2 \\ 0 & Q & 0 & 0 & -(h_2^2 + k_2^2) & -l_2^2 \\ 0 & 0 & R & 0 & -(h_3^2 + k_3^2) & -l_3^2 \\ 0 & 0 & 0 & S & -(h_4^2 + k_4^2) & -l_4^2 \\ \frac{(h_1^2+k_1^2)}{P} & \frac{(h_2^2+k_2^2)}{Q} & \frac{(h_3^2+k_3^2)}{R} & \frac{(h_4^2+k_4^2)}{S} & 0 & 0 \\ \frac{l_1^2}{P} & \frac{l_2^2}{Q} & \frac{l_3^2}{R} & \frac{l_4^2}{S} & 0 & 0 \end{bmatrix}^{-1} \begin{bmatrix} -P \\ -Q \\ -R \\ -S \\ 0 \\ 0 \end{bmatrix} \qquad \text{Equation 2-5}$$

From equation 2-5, the parameters (p, q, r, s, A, C) were determined. In this work (004), (224), (115) and (335) reflections were used. The lattice parameter of GaAs was taken to be 5.65338Å. From A and C, the in-plane (a) and out-of-plane (c) lattice constants were determined.

Now as the lattice constants are known, it is possible to calculate the Poisson ratio of the alloy. The composition of the alloy could be determined from the Poisson ratio, using Vegard's law. For a bi-axial compression the strain components are related by [17]

$$\varepsilon_{\perp} = \frac{-2\vartheta}{1-\vartheta}\epsilon_{\parallel} \qquad \text{Equation 2-6}$$

where $\epsilon_{\parallel}$ and $\varepsilon_{\perp}$ are the in-plane and out-of-plane strain components, respectively. The strain components are defined as [17]

$$\epsilon_{\parallel} = \frac{a-a_l}{a} \text{ and } \varepsilon_{\perp} = \frac{c-a_l}{c}$$

2.3.4 Least Square Criterion Method for Lattice Constant Determination

Observation of tilt in lattice-mismatched epitaxial layer is very common. Fig 2-6 shows the basic concept of tilt in epitaxial layers. III-V materials have the cubic lattice (zinc blende) structure. An ideal epitaxial condition, where the epitaxial layers are parallel to the substrate is shown in Fig 2-6 (a) and (b), for the case of fully and partially relaxed layers, respectively. Fig 2-6 (c) and (d) shows the condition where the epilayers are not parallel with substrate, for the case of relaxed and strained epilayers, respectively. The angle between the substrate and epilayers are known as tilt. There exist two reasons of tilt formation in epilayers. One is called the coherent tilt, which is the consequence of the substrate miscut and other is called incoherent tilt which is due to the imbalance of dislocation slips in the epilayers.

The amount of tilt can be easily measured by XRD. For growth on (001) substrate diffraction from (004) plane need to be obtained. From the ω-2θ scan two peaks will be observed corresponding to substrate and epilayers. Then the angle at which the epilayers peak appears should be determined. After aligning the x-ray system for that angle a ω_{rel}

scan is done and from the peak of this scan the magnitude and direction of the tilt can be determined.

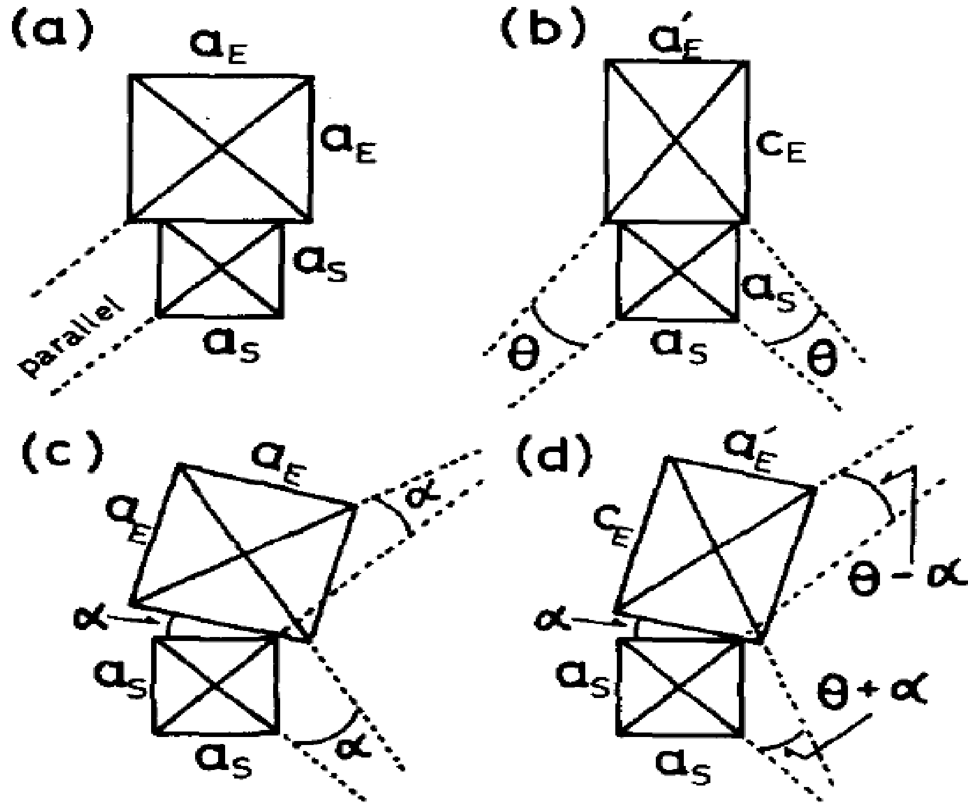

Fig 2-6: Relation between the epitaxial and substrate crystal lattice [18].

2.4 Atomic Force Microscopy

AFM is a powerful tool to characterize the surface morphology with nanometer-level precision. A cantilever tip is used which interacts with the atoms on the sample surface, leading to a force being registered by the cantilever which is then translated into an image containing the information about the surface morphology. The height of the AFM tip is monitored by a laser beam. There are 3 primary modes of AFM; e.g. contact, non-contact and tapping mode AFM. In this work, tapping mode AFM was used, in which the AFM cantilever is continuously vibrated as it is swept over a surface, and a feedback loop adjusts the height of the cantilever so that it experience a constant force from its interaction with the surface. Advantages of using tapping mode are higher lateral

resolution, lower force and less damage for the samples. A standard Si cantilever was used with a tetrahedral tip of radius ~10 nm (shown in Fig 2-7). Analysis of the AFM images were done by Nanoscope ver. 5.12 and Gwyddion.

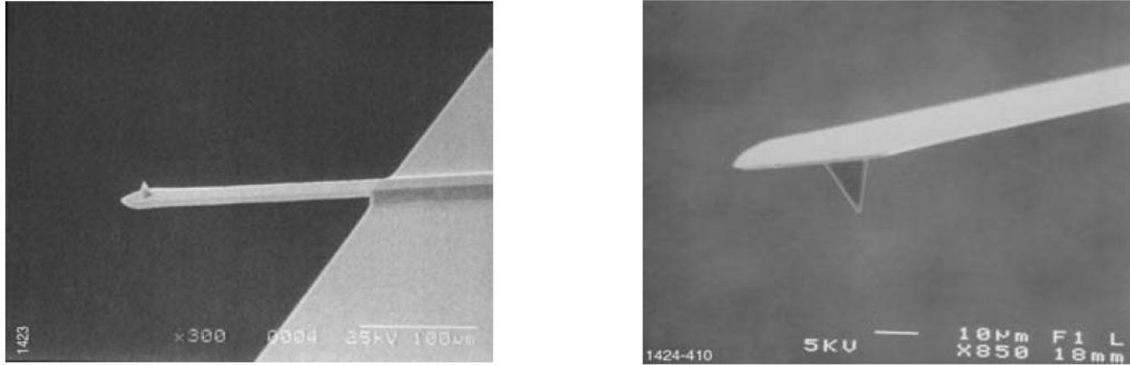

Fig 2-7: SEM images of Si-cantilever and tip.

2.5 Rapid Thermal Annealing

In the semiconductor industry, rapid thermal annealing (RTA) provides a controllable method of reducing defects in a sample. If the temperature is high enough, defects can gain enough thermal energy to diffuse towards the surface or other defects and thereby annihilates or form complexes when they interact with one another. It has been found [19] that for the appropriate annealing temperature, annealed samples contains less dislocation than the as-grown sample.

In this work, RTA was done for 30 seconds for the temperature range of 650-900°C using SiO_2 cap on top of the sample. The sample was placed in a quartz furnace chamber and a thermocouple was used to monitor the temperature. The temperature of the chamber was initially raised from room temperature to 450°C in 30 sec and held at that temperature for 30 sec, then the temperature was increased over a 30 sec interval until it reaches the desired temperature where it was held fixed for 30 sec. The quartz chamber was purged with ultra-high purity nitrogen during annealing. Samples were heated by banks of halogen lamps situated above and below the chamber. After the anneal time has elapsed, the halogen lamps are shut off and the sample is allowed to cool to RT before

removal from the chamber. The temperature, ramp rate and annealing time were computer controlled.

2.6 Photoluminescence

Photoluminescence (PL) is a non-destructive technique for investigating spontaneous emission processes in semiconductors. PL can be used for bandgap measurement, impurity and defect detection, and material quality evaluation. The spectrum of energy that is released during the recombination of electrons and holes in a semiconductor provides a means to acquire knowledge on the semiconductor bandgaps and quantum levels. The spectrum is obtained by exciting the specimen optically (or by the photon) and thereby, producing electron-hole pairs in excess of the thermal equilibrium condition. The incident photons must have an energy that is greater than the bandgap of the sample.

Two different PL setups were used for this work. In one case He-Ne laser (λ = 632.8nm) was used for excitation and for the other an Ar-ion laser (λ = 488nm) was used. Both InGaAs and Si detectors were used depending on the wavelength of interest. Low temperature spectra at about 9K to 11K were obtained by using a close cycled, helium-refrigerated, diffusion-pumped cryostat. A resistive heater was used to adjust temperature with the temperature measured by a calibrated thermocouple mounted on the cold-head below the sample.

2.7 Degree of Polarization

Polarization-resolved PL is a useful technique to map the strain field arising from device processing such as metallization and bonding, or due to the presence of defects such as edge or misfit dislocations in III-V based semiconductor materials [20]. The setup used for this work is has a strain resolution of 1×10^{-5} and spatial resolution of better than 1µm. This technique basically measures the relative strength of luminescence polarized along two orthogonal directions. There exists two ways of performing polarization-resolved measurements. One is spectrally resolved [21] and another one is room-temperature integrated luminescence [22]. The later was used in this work as it gives faster and more sensitive measurement. Standard ex-situ techniques of measuring strain

are the x-ray and TEM. X-ray is not useful for thin layers (e.g. QWs) and TEM only provides information over small area. Moreover, an extensive sample preparation technique is required for TEM. However, by measuring degree of polarization (DOP) strain mapping both of large areas and thin layers becomes possible. DOP is mathematically defined as [22]

$$\mathrm{DOP} = \frac{\int_0^\infty [\mathrm{L_{TE}(E) - L_{TM}(E)}]\mathrm{R(E)dE}}{\int_0^\infty [\mathrm{L_{TE}(E) + L_{TM}(E)}]\mathrm{R(E)dE}}$$

where $\int_0^\infty [\mathrm{L_{TE}(E) - L_{TM}(E)}]\mathrm{R(E)dE}$ and $\int_0^\infty [\mathrm{L_{TE}(E) + L_{TM}(E)}]\mathrm{R(E)dE}$ are the sum and difference of the intensities of the TE- (electric field in the plane of the layer) and TM- (electric field perpendicular to the plane of the layer) polarized luminescence from the layer of interest, integrated over all the energy transitions. R(E) is the responsivity of the detector. For an isotropic material, it has been shown [20] that the DOP is proportional to the difference in the components of strain (or stress) along two orthogonal direction. If the scanning direction is similar as shown in Fig 2-8, then [20]:

$$\mathrm{DOP_z} = -C_\varepsilon(\varepsilon_{xx} - \varepsilon_{yy}) \qquad \text{Equation 2-7}$$

where ε_{xx} and ε_{yy} are the normal components of strain along the x and y directions, respectively. C_ε is a positive calibration constant.

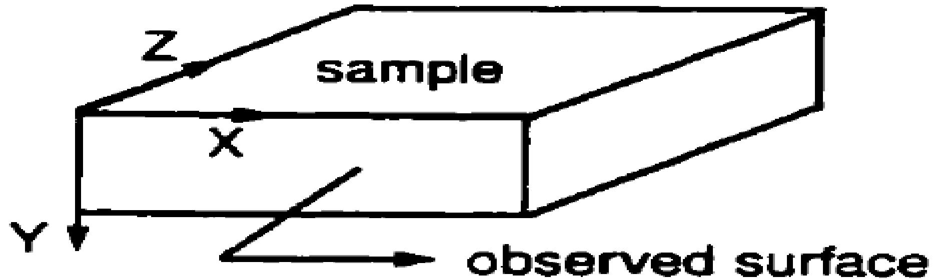

Fig 2-8: Scaning directions for DOP measurement.

The experimental apparatus used to measure the DOP is shown in Fig 2-9. The samples were optically excited by a He-Ne laser beam which was chopped at a frequency of 1010 Hz. A 40x microscope objective (Newport M-40X) was used to collect the luminescence from the samples. The luminescence then passed through a linear polarizer, rotating at a frequency of 200 Hz, and a 200μm pin hole to a detector (Si or InGaAs depending on the wavelength of interest). The samples were scanned across the measurement system by computer controlled DC motor. The accuracy of measuring the position is ~0.1 μm. Scanning directions are indicated in Fig 2-8. The samples were scanned in the 'x' direction and then stepped in the 'y' direction. Value of DOP was recorded at each scan point.

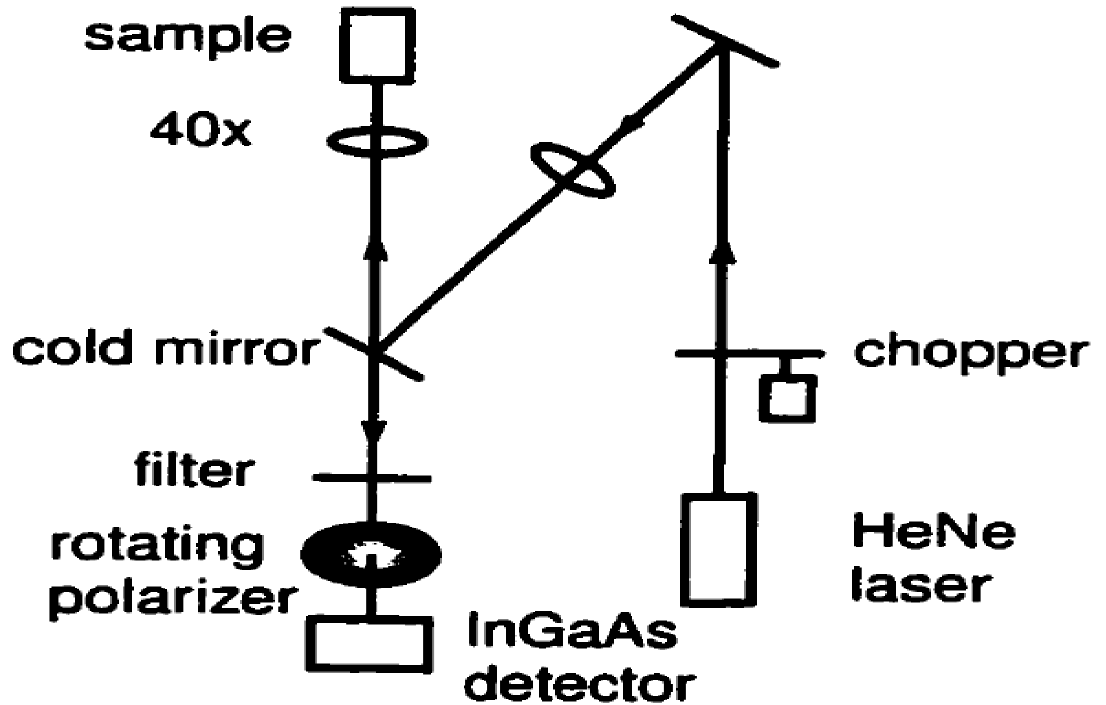

Fig 2-9: Experimental setup for the DOP measurement.

2.8 Transmission Electron Microscopy

Transmission electron microscopy (TEM) is an indispensable tool for examining the microstructural details of the epitaxial films. The technique was originally developed due

to the limited resolution of light microscope, which by principle cannot operate below the visible spectrum (~400-700nm). Since Louis de Broglie theorized that electrons have also wavelike characteristics with wavelength significantly lower than 400 nm, the possibility of using the electrons instead of the photons came forward. De Broglie's famous equation shows that the wavelength of electron, λ, is dependent on their energy, E, and, if relativistic effects are ignored (although for electron beam relativistic effects should be considered), then [23]

$$\lambda = \frac{1.22}{\sqrt{E}}$$

where E is in electron volts (eV) and λ is in nm. Thus if 100keV is applied, then the wavelength of electron would be 4 pm.

All electron imaging, for this work, were done using a Philips CM-12 electron microscope operated nominally at 120kV. Structural defects can be observed in the diffraction contrast, using bright-field or dark-field mode. Images are formed by the direct beam in the bright-field mode, whereas the diffracted beam is used for forming images in the dark-field mode.

Only cross-sectional TEM (X-TEM) was done in this work. The samples for X-TEM analysis were 100-200 nm thick and prepared by hand grinding followed by ion-milling using 4kV Ar^+ at $\pm4°$. The samples were cleaved along $<1\bar{1}0>$ direction with ~8mm in length and ~1mm in width. They were, then glued together by epoxy with the epilayers facing each other. Three Si-bars were then glued to both side and the whole structure was heated to harden the epoxy. The sample structure was thinned by grinding using different grit papers for both sides. Then two 3mm discs were cut from the sample structure. The central part of the samples was further thinned to ~20μm by dimpling. Finally, ion milling was done until a small hole appeared across the interfaces, which means that the sample achieves electron transparency. A liquid N_2 cold stage (about -165°C) equipped on the Gatan-PIPS system was employed for ion-milling.

Chapter 3 : EFFECT OF LOW-TEMPERATURE LAYER

3.1 Introduction

Obtaining a high quality metamorphic-buffer layer (MBL) has always been a major challenge. Growing an underlying lattice-matched buffer layer at low-temperature (LT) in strained heteroepitaxy has proved useful for various material systems [24-28] such as GaAs, Si, InP etc. The improved quality of the layers, grown above LT layer suggests it may be possible to achieve a better MBL by using an underlying LT layer. An example has been demonstrated for InAsP MBLs grown on InP wafer [27]. Typical characteristics of III-V LT layers are the large amount of excess group V elements and high density of point defects such as group V interstitials and V_{III} antisite defects [28]. Growing at low temperatures allowed the growth of high crystal quality nonstoichiometric material with a percentage of excess group V element that is highly dependent on the growth temperature.

In our experiment, InGaP LT layers, lattice-matched with GaAs, were grown for growth of an $In_xGa_{1-x}As$ MBL and compared with MBLs without the LT layers. It was found that although LT layer improves the optical quality of InGaAs MBLs significantly after annealing, the high annealing temperature introduce other surface defects.

3.2 Previous works

Using LT layer for growing InP based material on GaAs substrate has been proven beneficial [25, 26]. Kaminska et al. grew [29] LT GaAs and found that the amount of As interstitials and antisites depends largely on growth temperature. Warren et al. [30] confirmed the existence of excess As by TEM observation. The relative amount of As existing in the epilayer increases with decreasing growth temperature. These grown in point defects are known to have significant mobility [31]. A similar observation was found for the LT InP layer [28], where excess P is incorporated in the epilayer. Thus as the growth temperature is lowered, the incorporation probability of group V elements increased. Melloch et al. [32] discussed that the excess As in a LT-GaAs layer

precipitates upon annealing. They also showed the effect of coarsening of the clusters with annealing temperature. The size of As precipitates increases with increasing annealing temperature.

Horikawa et al. [25] used a thin (20 nm) LT GaAs layer between the GaAs substrate and an InP buffer layer. They showed that there is an optimal thickness of the LT layer which would improve the crystal quality of top InP layer. Existence of an optimal thickness was also confirmed by Ren et al. [26]. A thicker LT buffer layer might degrade the quality of top layers due to the crystalline imperfections, whereas a thinner LT buffer layer would not be enough to alleviate the distortions due to lattice mismatch. Radhakrishnan et al. [24] used both underlying LT GaAs and LT InP layers (both of them 20 nm thick) for the growth of InP on a GaAs substrate. Both x-ray and PL showed improved InP growth using this approach.

Although there is strong evidence that an underlying LT layer improves the quality of the strained layer, few reports are available where LT layers were used in compositionally graded systems. Czaban et al. [27] and Hulko et al. [33] found that a LT InP layer grown before the growth of a step-graded InAsP MBL resulted in improved optical and crystalline quality. Later Shahram et al. [34] used LT InGaP layer for the step-graded InGaAs MBL. He found large tilt of an InGaAs pseudosubstrate grown on top of the LT layer. These results suggest the possibility of achieving an improved pseudosubstrate by using an initial LT InGaP layer (lattice matched with GaAs) deposited first on a GaAs substrate.

3.3 Experimental Procedure

Two samples (sample A and B) were grown with the difference that 'A' has a LT-InGaP layer underlying the step-graded MSL. Both samples were grown by gas-source MBE (GSMBE) in a system manufactured by SVT associates. 2 inch diameter, epi-ready, (001) $\pm$ 0.1^0, GaAs wafers were used to grow the epilayers for both samples. Table 3-1 shows the layer-by-layer design of the two samples. The only difference between these two samples is that sample A has the LT InGaP layer before the MBL. An initial 0.1 μm

GaAs buffer layer was introduced to prevent the propagation of substrate surface defects into the epilayers. Based on the previous work on similar MBL [34] 85% relaxation was assumed initially for the terminating MBL layer. This is why $In_{0.26}Ga_{0.74}As$ is used as the barrier for quantum well (QW) layer ($In_{0.402}Ga_{0.598}As$). Lattice matched InGaP layers with $In_{0.26}Ga_{0.74}As$ were used to enhance carrier confinement. The 1% strained QW structure was used for PL measurements as a measure of the optical quality of the MBLs. The initial 100 nm thick GaAs buffer layer was grown at 500^{0}C and all subsequent layers were grown at 485^{0}C, except for sample A where the LT $In_{.485}Ga_{.515}P$ layer was grown at a rear-side thermocouple reading of 245^{0}C. All other temperature readings were based on the optical pyrometer data. The optical pyrometer cannot be used during the growth of LT layer as the noise becomes too high.

25 nm – $In_{0.73}Ga_{0.27}P$
150 nm – $In_{0.26}Ga_{0.74}As$
5 nm – $In_{0.402}Ga_{0.598}As$
150 nm – $In_{0.26}Ga_{0.74}As$
25 nm – $In_{0.73}Ga_{0.27}P$
700 nm - $In_{0.3}Ga_{0.7}As$
100 nm $In_xGa_{1-x}As$ with 2% increment of In upto x=0.28
LT- $In_{0.485}Ga_{0.515}P$ (245^{0}C) (For sample A only)
0.1 µm GaAs
Type-GaAs

Table 3-1: Structural detail of the samples. LT layer exists for only sample A.

ϖ-2θ and *ϖ*-relative scans were performed to obtain the residual strain, relaxation and mosaicity information. In-plane and out-of-plane lattice constants were determined by the 'refinement technique', described in chapter 2. For the photoluminescence (PL) measurement samples were optically excited using an HeNe laser. The PL spectra were collected with an InGaAs detector. All the PL measurements were done at room temperature. In this report all the PL intensity data shown are presented according to the 50 µV sensitivity of the lock-in amplifier which means that the value 10 is equivalent to the 50 µV. Rapid thermal annealing (RTA) was done for 30s at various temperatures (650-900ºC). During annealing the samples were enclosed in a graphite boat and a

nitrogen atmosphere. A SiO_2 cap was used during annealing as it caused less PL peak energy shift than an InP or GaAs cap [35].

3.4 Results and Discussion

Both in-plane and out-of-plane lattice constants were determined by using (004), (224), (115) and (335) planes x-ray reflections. From this two lattice constants, Poisson's ratio has been determined [17], which gives the exact composition of the top metamorphic layers. Table 3-2 shows the results obtained from the x-ray measurement.

Sample name	Relaxation (%)		FWHM (as-grown) (arc sec)		FWHM (annealed at 850°C) (arc sec)	
	As-grown	Annealed at 850°C	$\langle 110 \rangle$	$\langle 1\bar{1}0 \rangle$	$\langle 110 \rangle$	$\langle 1\bar{1}0 \rangle$
A	86.79	88.07	690.72	1036.85	680.51	1069.82
B	84.99	85.26	754.37	749.94	1037.55	964.81

Table 3-2: X-ray measurement data

The relaxation values for both samples are similar and they verify our initial assumption of 85% relaxation factor. Annealing does not seem to affect the relaxation significantly. Thus we can ignore any difference of relaxation between samples A and B. From FWHM of ω-relative scans of the top MBLs, it can be seen that mosaicity is less for the sample without LT layer. But after annealing at 850°C, mosaicity increases for sample B, while it was essentially unchanged for sample A. Sample A shows better crystalline quality or lower mosaicity than sample B after annealing. This suggests that 30s annealing at 850°C is too high for the InGaAs graded buffer. The reason of choosing this temperature is the highest intensity PL signal was achieved from sample annealed at 850°C. But as the crystalline quality degrades, annealing at this temperature is not suggested. 5x5 μm^2 AFM was employed to measure the rms surface roughnesses, which were 3.43 nm and 4.91 nm for sample A and B, respectively. Thus LT layer also improves surface morphology.

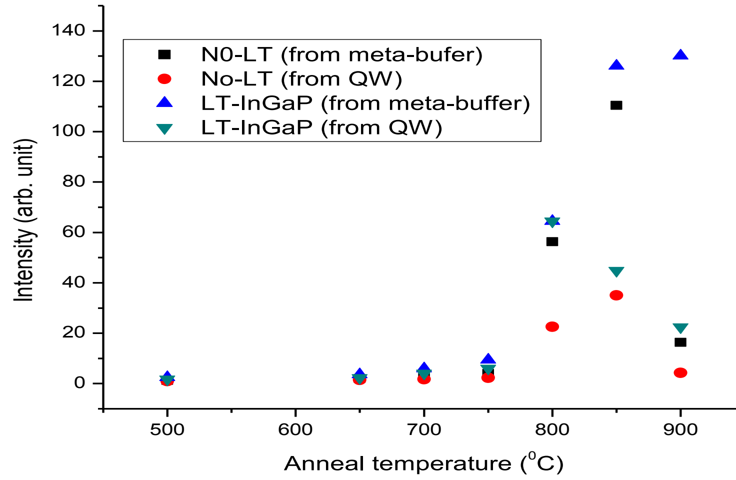

Fig 3-1: Change of PL peak intensity with annealing temperature.

PL signal was obtained from both the top metamorphic buffer and the QW grown on it. Fig 3-1 shows the change of PL intensity with annealing temperature. 500°C in the horizontal axis indicates the as-grown sample, as annealing at growth temperature should not affect the sample. As the annealing temperature increases, the difference of intensity between sample A and sample B also increases. Sample A showed higher intensity at higher annealing temperature. The intensity increased significantly for annealing at higher than 750°C and it starts to decrease after 850°C for sample B and after 900°C for sample A.

There is a blueshift of the PL peak wavelength as the annealing temperature increases (shown in Fig 3-2). It is due to the interdiffusion among different layers. It can be seen that the blueshift is less than 15nm from the top MBL peak which means that there some 'P' atoms diffuse from the top InGaP layer, but the interdiffusion was not significant; however the wavelength shift from the quantum well is larger. The blueshift is over 50 nm for annealing at 900°C. Larger blueshift of QW is due to the higher concentration gradient between QW and the barrier. Also some 'P' might diffuse to the QW. All the interdiffusion increases the bandgap of the QW and thus decreases the emission wavelength.

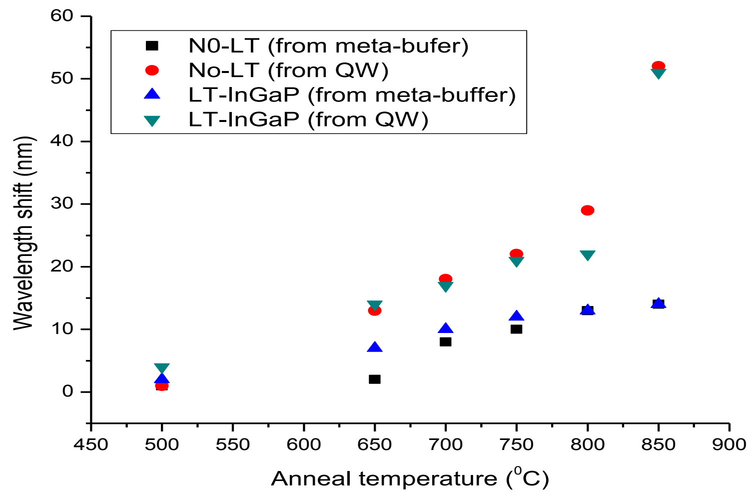

Fig 3-2: Blue-shift of PL peak wavelength with annealing temperature

FWHM of the PL spectra is similar for both as-grown samples (shown in Fig 3-3). FWHM from both meta-buffer and QW started to increase for annealing temperature higher than 750°C, which is an indication of the onset of the degradation of the optical quality. By observing the annealed samples in optical microscope, it can be said that the degradation is due to the appearance of surface defects. FWHM of the PL spectra from the QW tends to decrease upto 700°C, after that it starts to increase again.

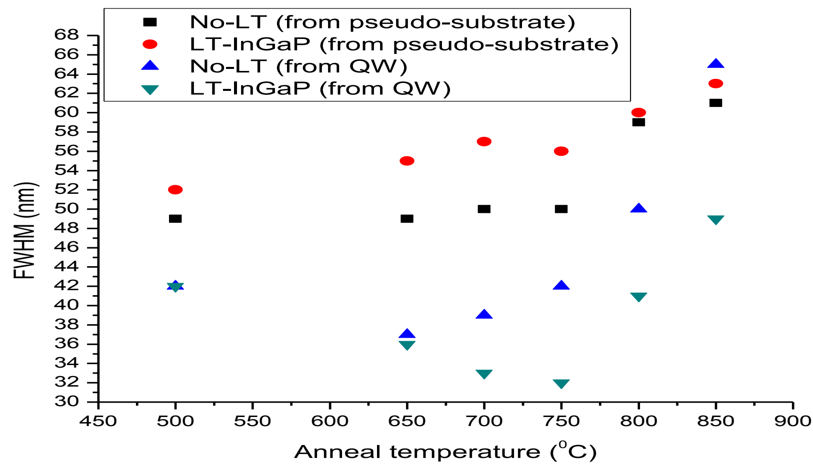

Fig 3-3: FWHM of PL spectra vs. annealing temperature

From these observations it can be speculated that the LT InGaP layer does not have any significant effect for the as-grown material. During annealing the sample with LT-InGaP starts to show better quality, but at the point where the difference becomes significant, some other mechanisms degrade the overall material quality. It can be speculated that the migration of excess P point defects to cluster formation may have improved the quality of the underlying LT layer, which in turn improves the quality of the top meta-buffer. To investigate the reason behind the higher FWHM after 750°C, samples were viewed by optical microscopy. Fig 3-4 shows a typical optical microscope image after annealing at 850°C. Cracks were observed in <110> direction. These defect structures become visible for annealing temperatures higher than or equal to 750°C. They become longer with increasing annealing temperature. SEM observation confirms that these lines are indeed cracks (shown in Fig 3-5).

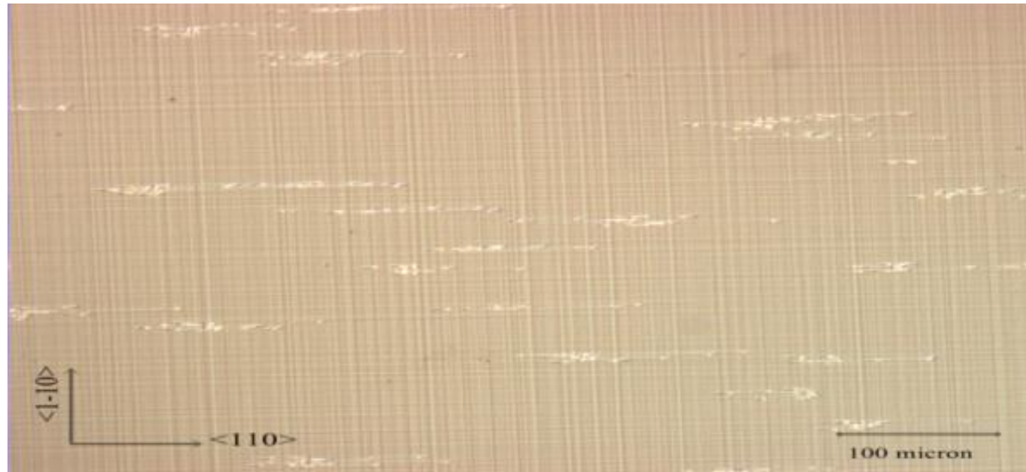

Fig 3-4: Optical microscope image of the sample surface after annealing.

The result seems unexpected; since the PL intensity shows significant improvement at annealing temperatures- when the cracks initiate. It is speculated that the excess point defects in the LT InGaP layer diffuse into the MBL, which in turn reduces the TDD into the MBL. Because these point defects were likely to interact with the existing dislocations and some of them might prevent the threading dislocations to go to the surface. Initially 60° MDs was formed to relieve the mismatch strain, but as the annealing temperature increases, larger thermal energy becomes available to form edge-

type dislocations by the interaction of two 60° MDs [36], which in turn reduces TDDs. The PL intensity increases due to the reduction of TDD. However, Olsen et al. [37] showed that the missing half planes of these edge dislocations are incipient microcracks.

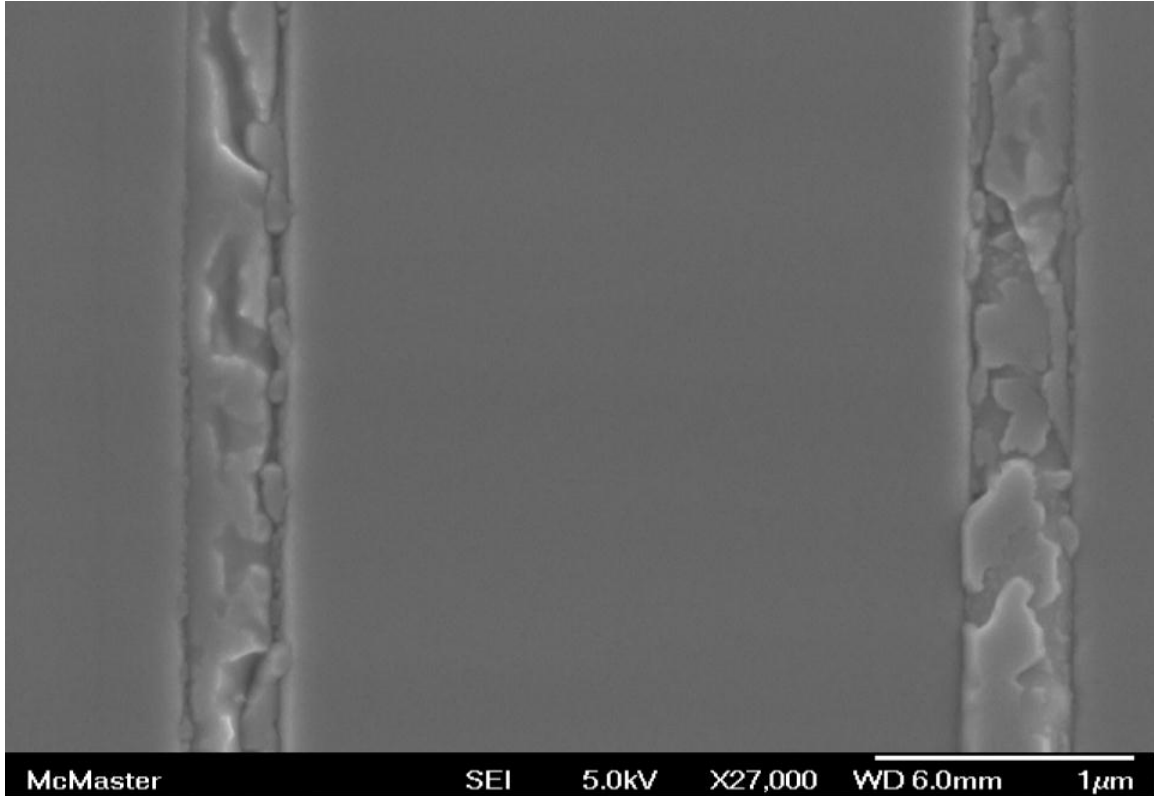

Fig 3-5: SEM image of the crack lines.

3.5 Summary

Introduction of a LT layer in the MBL might be helpful, but to utilize its full potential, it is important to optimize the growth of the LT layer, such as: thickness, growth temperature etc. For the case investigated in this work, use of a LT buffer offers no significant improvement in the as-grown samples. PL intensity rises during annealing, but the appearance of surface defects degrades the crystal quality.

Chapter 4 : SURFACE OBSERVATION OF METAMORPHIC-BUFFER

4.1 Introduction

To increase the flexibility for semiconductor device design using epitaxial growth it is necessary to grow the device structure on a metamorphic buffer and the morphology of the final buffer layer requires very careful attention. Researchers have been trying to control the surface morphology of hetero-epitaxial mismatched films [38] since 1980s. A flat surface is required for good device performance as a rough surface can lead to optical and electronic losses in the device. However, it is difficult to achieve a flat surface for lattice mismatched heteroepitaxy, whereas, for homoepitaxy and lattice matched heteroepitaxy, a flat surface is possible. It is almost impossible to prevent the surface of metamorphic-buffer from being rough. It has been shown by Srolovitz [39] that after a certain value of stress a flat surface is unstable.

The most common surface phenomenon in various types of metamorphic systems is the existence of cross-hatch (CH) pattern. In this chapter the CH phenomena is explained and the physics behind the evolution of this pattern is explored using an InGaAs/GaAs metamorphic substrate which is grown using MBE and the surface is characterized using AFM. The strain field is obtained using the DOP technique.

4.2 Cross-Hatch

Cross-Hatch (CH) is the characteristic undulating surface morphology which is common in semiconductor strained epitaxial layers, such as Ge_xSi_{1-x}/Si, $Al_xGa_{1-x}As/GaAs$, $In_xGa_{1-x}P/GaAs$, $In_xGa_{1-x}As/GaAs$ etc [40-45]. Although the surface morphology is generally mirrorlike when observed by bare eye, a CH pattern is revealed when a microscope is applied. This gridlike pattern consists of ridges aligned along $<110>$ and $<1\bar{1}0>$ directions, if a (001) substrate is employed.

The formation of CH pattern depends on many factors such as growth temperature, misfit strain and the thickness of the epitaxial layer. Typically a CH pattern is only observed for moderate crystal lattice mismatch $\varepsilon_m \leq 2\%$ for a single layer and this range can be extended if grading or metamorphic approach is applied [46]. In such systems the growth occurs in layer by layer mode (Frank van der Merwe mode). If the mismatch is much smaller, then planar surface is achieved and if the mismatch is higher, rough textured surface morphology appears. This undulating surface pattern is more evident in higher growth temperature. Chang et al. [36] modeled the growth mode based on three factors. The growth regime for various conditions is shown in Fig 4-1. This plot is for an InGaAs/GaAs heterostructure system. For other systems the plot would be similar but the values for the various regions would be different.

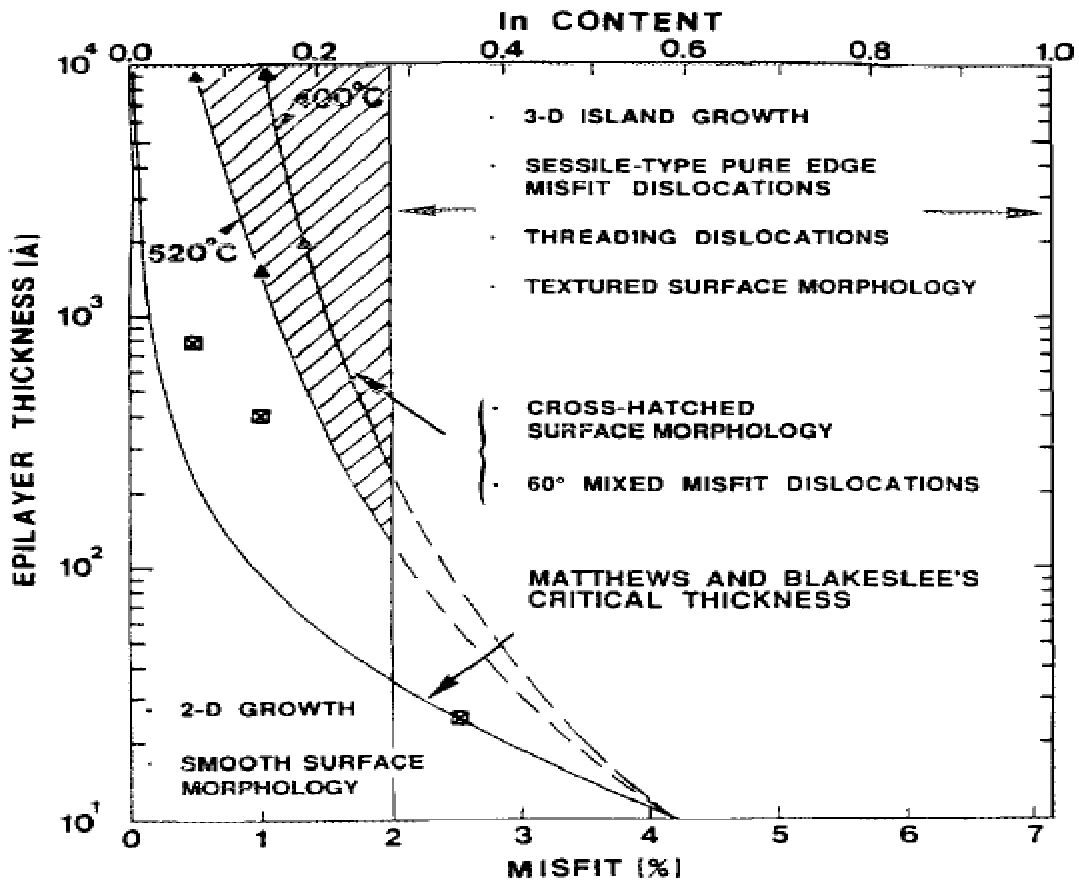

Fig 4-1: Plot of epilayer thickness vs. misfit in the InGaAs/GaAs system. Cross hatch patterns can be seen in the shaded area [36].

Fig 4-2 shows an optical microscope image of a typical CH pattern on the final layer of an InGaAs metamorphic buffer grown on GaAs (001) substrate, where the composition of the final buffer layer is $In_{0.3}Ga_{0.7}As$. From the figure it is evident that the ridges are aligned along the [110] and $[1\bar{1}0]$ directions. The periodicity of ridges is different in the two directions. This anisotropy leads to different performance of devices depending on the direction of fabrication [47]. Although this image gives an indication of the surface geometry, it is very difficult to interpret, as the surface features are close to, or below the wavelength of the light used. Thus AFM is normally introduced to analyze the surface. Also from the very early observations of the CH pattern it was determined that this undulation is related with the strain field of the surface layer. Thus DOP is employed to investigate the strain field of the surface and make a correlation between strain field and surface morphology.

Fig 4-2: Optical microscope image of cross-hatch in $In_{0.3}Ga_{0.7}As$ layer grown metamorphically on GaAs (001) substrate.

4.3 Background

Surface CH morphology was first discussed by Burmesiter et al. [48] on the $GaAs_xP_{1-x}$ layers grown on GaAs substrates. Since then many researchers have seen the CH pattern and tried to explain its evolution. Despite the frequent observation of

crosshatch, its origin remains still unclear and controversial. There are essentially two models that can be found in the literature. One model suggests surface undulation is due to elastic strain relaxation during pseudomorphic growth that leads to stress concentrations and subsequent formation of dislocations at troughs [46]. The second one suggests the misfit induced strain initially relaxes by forming misfit dislocations followed by enhanced growth rates at the relaxed surfaces above the dislocation, which then produces the surface undulations [40, 44].

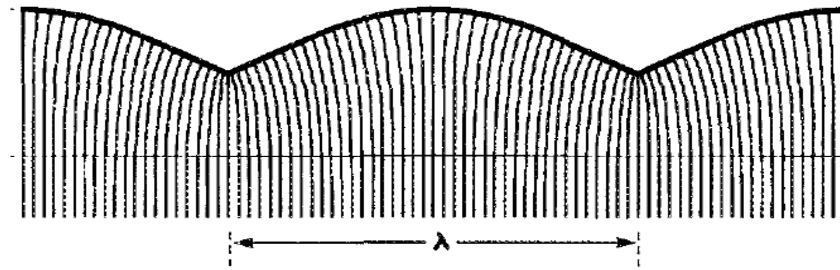

Fig 4-3: Elastic distortion of vertical lattice planes in a morphologically undulating heteroepitaxial layer under compressive stress [46].

Kishino et al. [49] found that the surface curvature of a GaAs substrate in which CH pattern is visible was always less than for a substrate where CH is not visible, if the strain imposed by the growth of strained GaAsP remained similar. The smaller surface curvature indicates that some portions of the strain were relieved in the cross-hatched sample. Consider a heteroepitaxial film which is grown compressively on a substrate (shown in Fig 4-3). For this type of undulated surface, the stress distribution becomes non-uniform and partial elastic stress relaxation will occur at the peaks in the epitaxial layer. The stress relaxation at the peaks occurs because the peaks are less supported by the surrounding material and hence are more able to relax. In other words, curvature of the surface in the peaks results larger volume which reduces the stress there. However, a consequence of this is that there will be stress concentration at the troughs. But this latter compression is localized so that the amount of material subject to additional stress is less than the amount of material subject to relaxation. Overall, the system free energy becomes lower in the undulated state than the planar surface.

G. H. Olsen [50] has found that MDs are correlated with the cross-hatch pattern. He suggested that the CH pattern is initially caused by accelerated crystal growth about MDs, and once initiated these will continue to propagate. But he could not provide a strong physical model for the evolution of the CH pattern. Franzosi et al. [51] suggested that presence of the CH pattern is a consequence of the misfit. They found that there is a correlation between MDs and the CH lines. However, the correlation is not one to one.

Frank Glas [52] suggested that the undulation is due to composition modulation along the surface. He calculated the elastic energy of an epitaxial layer of finite thickness (coherently grown on a bulk substrate), whose intrinsic lattice parameter is modulated along directions parallel to the substrate and showed that if the modulation has components with spatial periods of same order as the thickness of the layer, the elastic energy is considerably lower. This method fails to explain CH pattern observed in the epitaxial layers which are not coherent. Also CH was observed in a layer where there is no significant composition modulation. Chang et al. [36] also showed that CH occurs in a layer where there is no composition modulation.

Srolovitz [39] showed analytically that the surface of a stressed solid is unstable with respect to the formation of a CH pattern with a periodicity greater than a critical value, but failed to solve the surface evolution problem to determine the equilibrium state. Spencer et al. [53] were able to derive the fundamental equations which describe the morphological instability. They used a time dependent linear stability analysis and suggested that low temperature growth or an elastically stiff substrate can reduce surface instability.

Pidduck et al. [54] tried to find out the energy of a sinusoidally undulated surface and compare that with a planar surface which has similar strain. Their premise was that the strain is also a sinusoidal function which is 180° out of phase with respect to the surface undulation. They found that the undulated surface is more stable. According to their model a weak surface undulation forms first at the initial stage of the growth, then as the growth continues roughness and strain energy accumulates, which gives way to

strong surface diffusion currents resulting in regular undulation. Eventually MDs form and this reduces the strain in the film and slows the diffusion currents. But the physical basis of their assumption is not clear. Cullis et al. [46, 55] also found similar results. They suggested that the troughs are the source for MD generation.

Jesson et al. [56] imaged the formation of the undulation by TEM. They termed the undulation as surface cusps. They have shown mathematically that surface cusps form due to the gradient in the surface chemical potential. Stress concentrates at the cusp tip, which leads to the formation of MD. Their model was quite similar with A. G. Cullis [46].

Andrews et al. [44] used Monte-Carlo simulation to analyze the CH formation. According to their model surface steps forms in the epilayer due to the glide of MDs. Lateral surface transport then eliminates the surface steps and creates an undulated surface morphology. Jallipalli et al. [57] showed that the MD distribution at the hetero-interface also has a CH pattern and thus it has some obvious relation with the surface morphology. It has been shown by Tångring et al. [58] that by doping with Be, the surface roughness of InGaAs meta-buffer can be reduced. They showed by TEM that Be-doping reduce TDD in the buffer layer

4.4 Experimental Procedure

A step graded $In_xGa_{1-x}As$ metamorphic buffer layer was grown by gas source molecular beam epitaxy (MBE). Compositions of different layers are shown in Table 4-1. Arsenic (As) and phosphorous (P) were deposited from dimers (As_2, P_2) produced by cracking AsH_3 and PH_3. Group III elements Gallium (Ga) and Indium (In) were produced from separate Knudsen effusion cells. Cell temperatures were calibrated to yield the desired composition. 2 inch diameter, epiready, Si-doped n-type GaAs (001) $\pm$ 0.1° substrates were used. Doped GaAs substrates are commonly used for photonic devices as they have lower dislocation density compared to a semi-insulating GaAs substrates [59]. The substrate surface was cleaned in-situ by using hydrogen plasma. Sufficient As_2 flux was used to maintain surface integrity. The substrate was rotated during growth to insure

thickness and composition uniformity over the surface. The wafers were mounted on a molybdenum holder facing downward. Growth was done at a nominal rate of 1 μm/hr. A 100 nm GaAs buffer layer was deposited at the beginning of the growth. The reason behind this is that the quality of epitaxial layer surface is better than the underlying substrate. Also, this buffer layer is capable of burying any particulate present at the initial surface [60]. Although crystal defects in the substrate can propagate through the epitaxial layer, they tend to diminish as the growth continues. All the epitaxial layers except the low temperature (LT) one were grown with a pyrometer reading of 500°C. The LT-layer, where used, was grown at a rear side thermocouple reading of 245°C. This layer had previously been shown to improve the quality of the buffer layer [27]. An InGaP layer at the top was deposited to act as a potential barrier to get photoluminescence (PL) from the terminal metamorphic layer, as it is necessary to get PL for DOP analysis.

200 nm $In_{0.73}Ga_{0.27}P$
700 nm $In_{0.3}Ga_{0.7}As$
100 nm $In_xGa_{1-x}As$ (14 steps x incremented at 0.02/step)
500 nm low temperature $In_{0.485}Ga_{0.515}P$ (at 245°C)
100 nm GaAs buffer
n-type GaAs (001) substrate

Table 4-1: Metamorphic structure details

The grown sample was characterized by Nomarski microscopy, DOP and AFM. Tapping mode AFM was used. Before analyzing the sample by AFM and optical microscopy, the top InGaP layer was removed using a $HCl:H_3PO_4$ (1:3) mixture to etch the InGaP layer. The etch rate of this solution is 400 nm/min.

4.5 Results

Fig 4-4(a) illustrates experimental observation of the surface CH pattern as obtained by AFM from a surface area of 15×15 μm^2. A 3D image of this clearly shows the surface undulations in Fig 4-4(b). It is evident that the morphology is not similar in two perpendicular <110> directions. This anisotropy is attributed to the anisotropy of strain relaxation in two directions [41, 45].

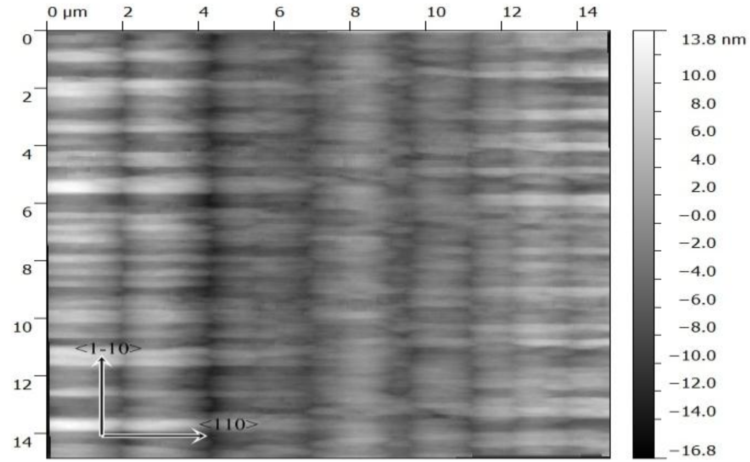

(a)

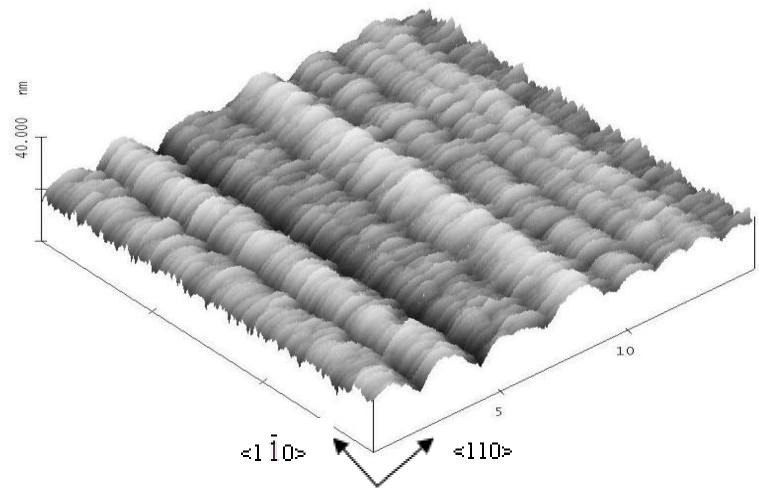

(b)

Fig 4-4: (a) AFM images of the final layer ($In_{0.3}Ga_{0.7}As$) of metamorphic buffer, (b) 3D view of surface undulation of the same sample shown in (a).

The RMS roughness of the sample area is 2.33nm. But the roughness along <110> direction is higher than the roughness along <1$\bar{1}$0>. Mean roughness along <110> and <1$\bar{1}$0> directions were determined to be 2.45 nm and 1.36 nm, respectively. To determine the peak to valley heights line scans were done in both <110> and <1$\bar{1}$0> directions (shown in fig 4-5). It is clear that the mean peak to valley height is greater in <110> than in <1$\bar{1}$0>direction. Quasi-periodicity of the surface striations in both directions can be

seen. Also, the surface undulation is not sinusoidal; troughs are sharper than the peaks (shown in Fig 4-5). Sometimes, the depth of an individual trough is significantly greater than the average. In that case, more steeply inclined facets appeared to be formed at the trough bottoms. As it is seen from height profile that CH patterns are quasi-periodic and determination of its wavelength is not straightforward. Thus we employed FFT analysis to determine the periodicity in the two directions. The mean periodicity of the surface undulation in <110> direction is ~2.6 µm and in <1$\bar{1}$0>direction is ~1.2 µm.

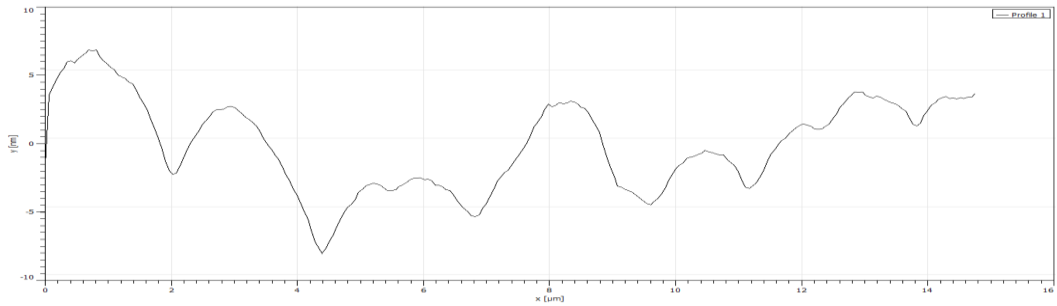

(a)

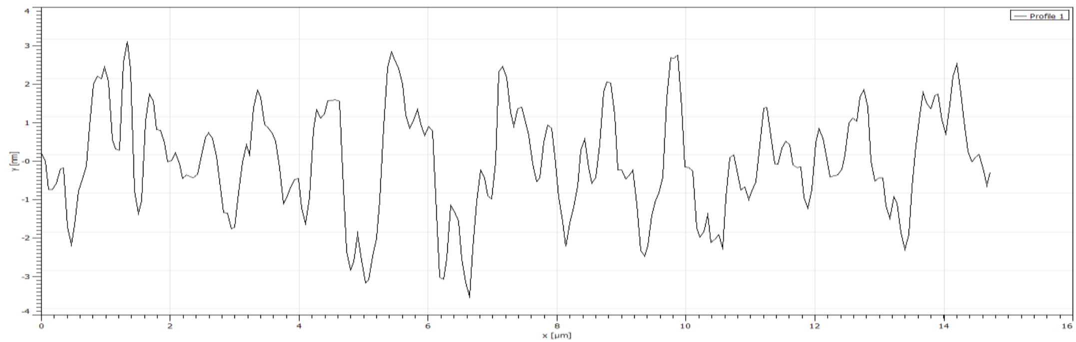

(b)

Fig 4-5: Surface height profile along (a) <110> and (b) <1$\bar{1}$0> directions. Horizontal axis indicates the scan direction (shown upto 16µm) and the vertical axis represents the surface heights in nm (in (a) range is -10 to 10 nm and in (b) range is from -4 to 4 nm.

Before measuring DOP, it is important to check that PL wavelength arises from the top metamorphic layer. Thus PL signal from the sample was collected (shown in Fig 4-6). Fig 4-7 shows the DOP map of 100×100 µm^2 area. A DOP map is basically the difference between the strains in two perpendicular directions. Offset value of DOP is the

value that occurs most frequently in the scan and found for this scan is -1.4%. Thus in Fig 4-7 the green color means -1.4% DOP. The maximum negative value obtained was ~-12.3% and maximum positive value was ~5.5% DOP. A high DOP value represents a highly strained region. It is clear from the strain map that the dislocation structure looks qualitatively similar to the CHP. Thus it is obvious that there is some correlation between the strain field and surface morphology. Although the pattern is similar, the mean periodicity in the DOP map is not the same as the CH pattern. Mean DOP periodicity in <110> direction is ~8.3 μm and in <1$\bar{1}$0>direction is ~4.6 μm.

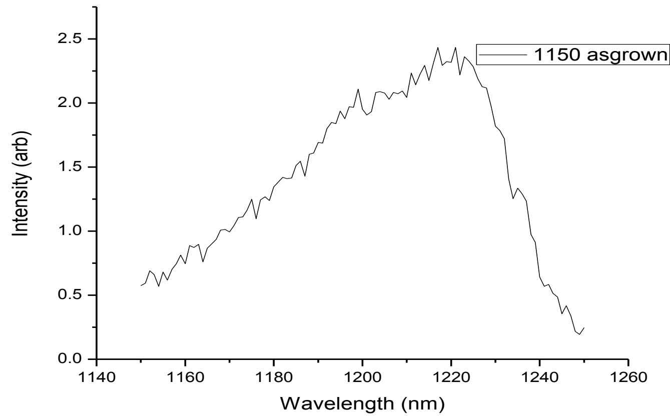

Fig 4-6: Photoluminescence signal from the sample.

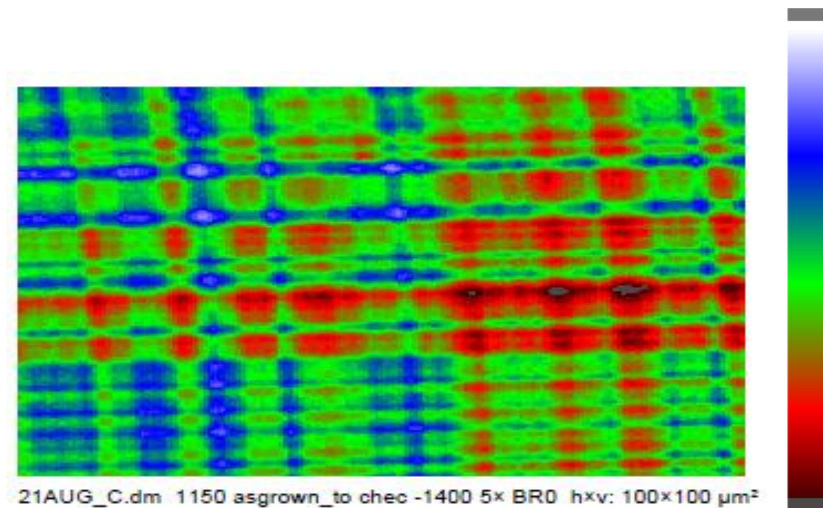

Fig 4-7: Maps of DOP of the sample (100×100 μm^2).

4.6 Discussion

It is important to check how much strain is relaxed in the sample and if the LT layer induced any extra strain or not. Thus X-ray rocking curve data is used to check the as-grown sample (shown in Fig 4-8). There is no side-peak close to the GaAs peak, which indicates that the LT-InGaP layer was closely lattice-matched with GaAs substrate. The peak at around -2500 arc sec was from the 200 nm $In_{.73}Ga_{.27}P$ capping layer and the peak around -3050 arc sec was from the 700 nm thick final layer of the meta-buffer. Thus the capping layer was lattice matched with the in-plane lattice constant of the meta-buffer. The value of in-plane lattice constant of the final meta-buffer layer was calculated in a method shown in Chapter 2 and it is 5.7560Å.Thus the final layer is 84.5% relaxed.

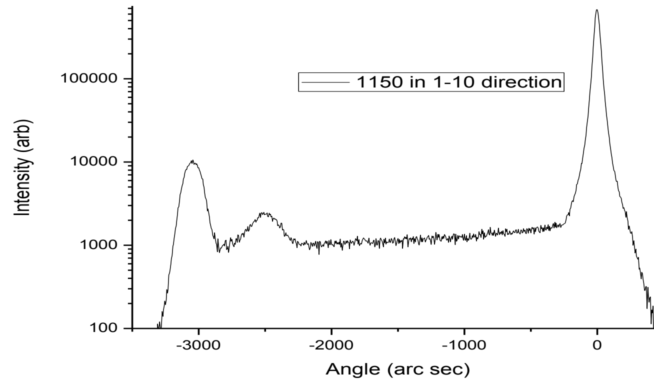

Fig 4-8: omega-2theta curve for the as-grown sample where the beam is incident on [1-10] direction.

Since the final layer is compressively strained, analysis of the PL signal is not straightforward. Equation 4-1 was employed to calculate the band energy and hence the wavelength from the final layer [61].

$$E_g^{str} = E_g^{bulk} + \Delta E_h \pm \Delta E_s \qquad \text{Equation 4-1}$$

here E_g^{str} and E_g^{bulk} are the strained bandgap and bulk bandgap energies, respectively. The hydrostatic energy shift ΔE_h is,

$$\Delta E_h = -2 d_1 \varepsilon_{11} \left(\frac{C_{11} - C_{12}}{C_{11}} \right)$$

and the strain contribution ΔE_s is,

$$\Delta E_s = \pm d_2 \varepsilon_{11} \left(\frac{C_{11} + 2C_{12}}{C_{11}} \right)$$

where ε_{11} is the residual strain and C_{11} and C_{12} are the elastic constants. For a compressively strained layer ΔE_s is positive and for tensile strain ΔE_s is negative.

From these calculations, it was determined that the PL signal should be ~1215nm, confirming that the PL signal of Fig 4-6 comes from the final meta-buffer layer and hence the DOP map corresponds to that layer only. Thus the reason of the nonzero offset value arises from the interfacial anisotropy [62]. From the DOP map, it can be seen that there are rows propagating in both <110> and <1$\bar{1}$0> directions. These rows are similar to the dislocation lines found in [20]. Also facet scan was done to identify the strain field patterns. By comparing the calculated DOP pattern for various types of dislocation with the measured one, we can identify the type of dislocations that exists in the sample. From Fig 4-9, it can be said that the MD dislocations are primarily of 60° type. The shape of DOP is slightly different than the calculated shape because of the interaction of strain fields with other MDs. Some edge dislocations were also observed in the sample. Hence it can be said that the lines in Fig 4-7 are dislocation lines. Because of the PL emission wavelength used for the DOP map, it only gives the strain map for the final meta-buffer.

(a) (b)

Fig 4-9: (a) Calculated DOP map for 60° MD [20], (b) example of DOP obtained from the sample.

Although the CH pattern in the surface and the dislocation pattern look similar, the periodicity between dislocations is higher than the periodicity in the CH. If the CH pattern was only developed from the step creation from underlying MD grid as discussed

in [40, 44, 57, 63], then the periodicity should be equal. But that is not the case found here. Because of the ability of DOP measurement to map the strain field in large scale, it became possible to measure the periodicity more accurately. Therefore, results from my thesis research support the other existing model [46, 54, 55, 64], which states that CH appears as a form of elastic stress relaxation. My results suggest that MDs form in the troughs of some of the undulations.

Thus it appears that the surface CH does not simply arise from the areas of growth above MDs. A cross-sectional TEM image (shown in Fig 4-10) was obtained to check if there is any periodic compositional variation present in the final meta-layer. It looks homogeneous and thus we can ignore the effect of compositional variation in our case.

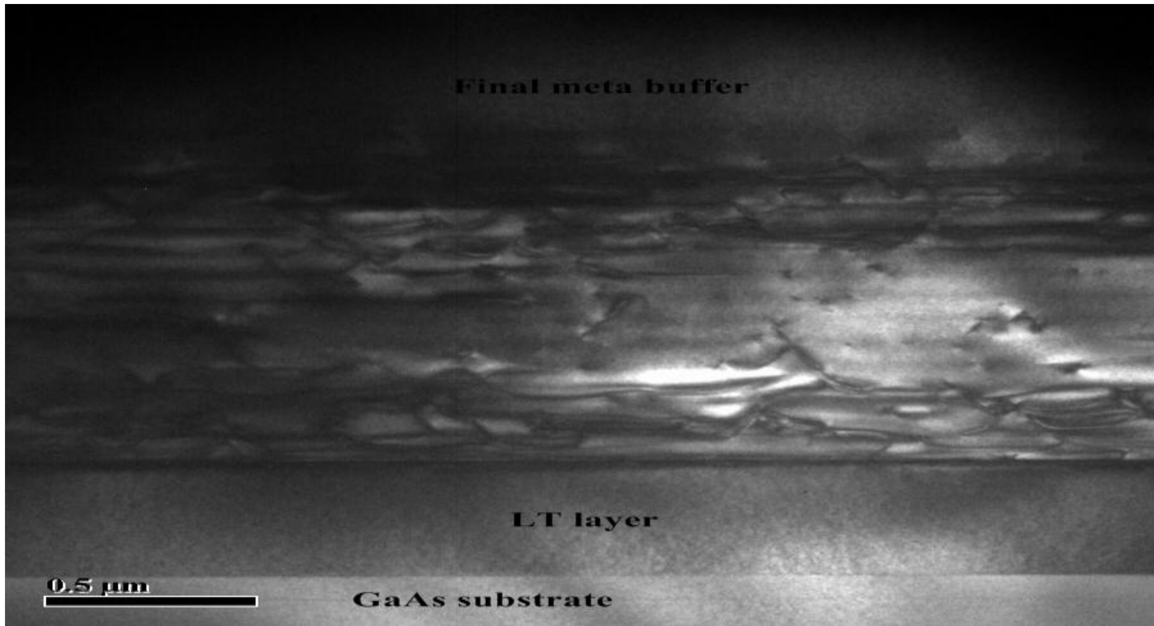

Fig 4-10: Cross sectional TEM bright field image of the sample.

Albrecht et al. [65] and Gao et al. [66] showed that CH could be found in a layer which is below the critical thickness. Thus cross-hatch forms before the nucleation of MDs. Although roughness arising from the CH increases the surface energy, the total free energy decreases since some strain is relieved. Compressive stresses in the layer are relieved partially by elastic lattice expansion at the peaks, and the valleys become highly

compressed stressed regions. It has been shown [46] that the overall free energy of the system is reduced by the undulations. Thus the strain field becomes non-uniform and this further develops the undulations. For the Si_xGe_{1-x}/Si(001) system it was found that initial ridges before the formation of MDs are in <100> direction [65, 66]. But after forming MDs in <110> direction, the strain field of MD influence the CH pattern to rotate 45° and ridges are aligned with the direction of MD line [66]. However, the process of rotation is not clearly understood till date.

As the growth proceeds local stresses in troughs increase. It is evident from the AFM image that the troughs are more cusp-like. As the stress increases the cusp sharpens more and this increases adatom migration towards the peak of the undulation. At some point the curvature of the cusp and concomitant stress concentration accelerate rapidly [56]. Thus the kinetic barrier of dislocation nucleation reduces at the cusp and some of the troughs become the source of misfit dislocation. Cullis et al. [64] also showed by TEM images that MDs form at the troughs. MDs are most likely to be Frank dislocation half-loops. After MD formation, the growth rate increases at the surface above MDs and it creates new ridges in the undulation. Thus the periodicity of the undulation decreases. As the growth proceeds, some planarization occurs. However, the driving force associated with the planarization is not strong enough and CH continues.

Now the question arises that as the strain is similar in two orthogonal <110> directions, why the periodicity is different in two directions. It has been shown that the initial CH formation was also anisotropic [66] and it in turn influence the anisotropy of MDs. The anisotropy of MDs is normally attributed to the polar nature of 60° MDs (α or β). For III-V semiconductor α dislocations are more mobile than β dislocation. For compressively strained heterogeneous systems such as $In_xGa_{1-x}As$ on GaAs, α dislocations lie in <1$\bar{1}$0> and β dislocations lie in <110> direction. Due to the asymmetry of mobility in two directions, there exist asymmetry in dislocation density [67]. It has been reported that the ridges form first in <1$\bar{1}$0> direction [41]. Hence the density of

MDs is expected to be higher in <1$\bar{1}$0> directions than in <110> direction. This explains the anisotropy of CH and strain field in two orthogonal <110> directions.

4.7 Summary

The surface morphology of an InGaAs metamorphic substrate grown on a GaAs has been investigated. A CH pattern has been observed and the evolution of this surface morphology is discussed. To summarize the evolution process we can define three stages of CH formation:

i. Formation of an undulated surface morphology as a means of elastic stress relaxation.
ii. Adatom diffuse towards the peak of the undulation, which sharpens the valley and lead to the nucleation of MDs at the valleys of the undulations, where local stress concentrations occur.
iii. Step creation at the surface above MDs and enhancement of the growth rate above the MDs create new ridges which lowers the wavelength of surface undulation.

Chapter 5 : COMPARISON BETWEEN ANION VS. CATION AND LINEAR VS. LOGARITHMIC GRADING

5.1 Introduction

Compositionally graded metamorphic buffers (MBs) generate a new pseudo-substrate having the desired lattice constant on which to grow new devices with low defect densities and hence have great promises for device applications. MBs have been grown on various substrates such as Si, GaAs and InP. Si_xGe_{1-x} MBs are normally grown on top of Si substrate in order to grow Ge based devices on Si substrates and integrate optoelectronics or photonic devices on Si technology [68]. MBs are grown on top of GaAs and InP substrates to increase the available pseudo-substrate lattice constants in bandgap engineering, where it is required to grow longer wavelength devices, particularly on InP. This work is focused on MBs grown on GaAs substrate so that GaAs substrates can be used instead of InP. Because of limited size, higher cost and higher fragility of InP substrates, they are less preferred than GaAs substrates. Also if InP based devices have been achieved on GaAs wafers, it would be considered as a giant leap for integrating longer wavelength devices in Si/SiGe based technology.

There are different approaches of growing MBs. The goal is to minimize the threading dislocations density (TDD) in the pseudo-substrate and to reduce surface roughness. Dislocations can act as non-radiative recombination centres while surface roughness or strain non-uniformity cause alloy separation, which in turn broadens the optical emission spectra for photonic devices. The quality of MBs depends on various factors. Some of them are related to the growth parameters such as growth temperature; III/V flux ratio; and some are related to the design parameters such as dopant, how the strain will vary and either the anion or cation will be used as a grading component etc. In this work, two types of variations were attempted. We have grown both ternary ($In_xGa_{1-x}As$) and quaternary ($In_xGa_{1-x}As_yP_{1-y}$) buffers and for both of them we applied linear and logarithmic compositional grading. The composition ‘x’ of group III element was kept

fixed for the quaternary and only the composition ‘y’ of the group V element was varied. Both quaternary grading approach and logarithmic grading approach are novel ideas.

5.2 Distribution of Misfit Dislocations in graded layers

Significant work has been done to optimize the design and concentration profiles of step and linear-graded metamorphic structures [27, 69-72]. Relatively little attentions has been given to non-linear grading. As the analytical model of strain relaxation for compositionally graded profile is still not well understood, it is very difficult to establish an optimized grading profile. Romanato et al. [72] presented an analytical model to calculate the MD profile in a metamorphic structure. Their model, similar to earlier models, is based on the assumption that the relaxation law that holds for a uniform layer, can be extended to a compositionally graded layer.

Now for a uniform epitaxial layer the mismatch due to the lattice mismatch, f, is accommodated by the introductions of MDs. If λ is the density of MDs per unit length and b_{II} is the burger’s vector component parallel to the interface, then the residual in-plane strain, $\mathcal{E}$, can be expressed as

$$\mathcal{E} = -f + b_{II}\lambda$$

For compositionally graded profiles, MDs are distributed over the graded layers with cross-sectional density per unit area, $\mu(t)$, which depends upon the distance, t, from the substrate. Then the equation for the residual strain becomes

$$\mathcal{E}(t) = -f(t) + b_{II}\int_0^t \mu(\tau)d\tau \qquad \text{Equation 5-1}$$

Here, $\mathcal{E}(t)$ and $f(t)$ are the depth profile of residual in-plane strain and lattice misfit with respect to substrate, respectively. If full strain relaxation ($\mathcal{E}(t) = 0$) has been assumed, then from equation 5-1

$$\mu(t) = \frac{1}{b_{II}}\frac{d}{dt}f(t)$$

The assumption of full strain relaxation means that the gliding force due to existing dislocation strain fields is strong enough to push the MD towards the substrate at the depth, where the strain is fully relaxed. If local strain fluctuations and dislocation-dislocation interactions are neglected, then there exist two opposing forces. One is the Peach-Koehler force that pushes MDs towards the substrate and another one is the image force because of the film surface that pushes MDs upward. It has been shown [73] that for the graded structure Peach-Koehler forces make the second one negligible. Now if we consider t_b as the total thickness of graded layer and after t_0 the layer is free of MDs, then $\mathcal{E}(t)$ would be zero for the thickness, $t \leq t_b$ and $\mathcal{E}(t) = -[f(t) - f(t_0)]$ for $t_0 \leq t \leq t_b$.

5.3 Background of metamorphic buffer

Metamorphic buffers have been used to restrain the surface strain below the regime of three-dimensional growth by increasing the strain by incremental steps [12, 74]. The early observations were on the graded $GaAs_yP_{1-y}$ structure grown on a GaAs substrate. It was later shown [75] that a graded $In_xGa_{1-x}As$ buffer also has a lower threading dislocation density than if grown directly on top of GaAs. From then almost all types of possible compositionally graded structures have been tried, such as: Si_xGe_{1-x}/Si [75], $In_xAl_{1-x}As/GaAs$ [76], $GaAs_ySb_{1-y}/InP$, $In_xGa_{1-x}Sb/GaSb$ [77], $InAs_yP_{1-y}/InP$ [78]. The success of these is mainly attributed to the increase of glide velocity of dislocations so that dislocations have higher probability to go towards the edge of the sample instead of threading in the growth direction [60]. A tremendous amount of effort had been put forward to optimize the growth of these graded structures. Step-graded and linear-graded structures are mostly employed in these studies. However, using these structures in mass production has not been achieved yet.

Fitzgerald et al. [68] achieved fully relaxed Ge_xSi_{1-x} layers on Si substrate. They have grown the graded structures for different x values by MBE and CVD and showed that TDD of terminating layer is less than the detection limit of TEM. Fitzgerald et al. [79] also calculated the effect of strain on surface morphology for the graded structure. It has been shown that cross-hatch morphology is quite common for this type of system. As a

consequence the surface becomes rough. Surface roughness is greater for a higher grading rate, and this introduces a higher TDD in the final layer. It has been also shown that TDD also depends on the final composition of the system and tilt of the substrate surface relative to the (001) direction.

It has been shown mathematically by Tersoff [80] that for graded layers, the force on threading dislocations is greater. This enables the movement of threading dislocations and glide in the interface more easily, which inhibits new MD generation. He also showed that the pinning of existing dislocations is less likely to occur in graded structure which increases the barrier to new MD generation.

Chyi et al. [76] compared the metamorphic growth of $In_xGa_{1-x}As$ and $In_xAl_{1-x}As$. They showed that crystallographic tilt often develops in graded systems and it depends on the mechanism of strain relief (α vs. β dislocations). A higher relaxation and smoother surface was been achieved for $In_xGa_{1-x}As$. Thus for practical purposes compositionally graded $In_xGa_{1-x}As$ has superior quality over $In_xAl_{1-x}As$. Kim et al. [81] modeled strain relaxation for a linearly graded system. They demonstrated that for this system, the critical thickness varies with film thickness. It has been shown that dislocations generated at any film thickness move towards the bottom and edges of the film.

Romanato et al. [72] used non-linear grading for the $In_xGa_{1-x}As/GaAs$ structure. They examined the influence of grading laws and growth temperature on residual strain, TDD and surface morphology. Lower TDD was achieved by using As_2 rather than As_4. They compared step, linear, parabolic and square root graded systems. It was found that parabolic and square root graded systems had a larger area free of MDs.

Hudait et al. [69] compared a cation vs. anion grading ($In_xAl_{1-x}As$ vs. $InAs_yP_{1-y}$) approach on InP substrate. It was found that $InAs_yP_{1-y}$ has lower surface roughness than $In_xAl_{1-x}As$. They have also grown thermo-photovoltaic (TPV) devices on top of these two metamorphic substrates and found better performance for $InAs_yP_{1-y}$ grading. Choy et al. [82] investigated the effect of substrate temperature on a compositionally graded InGaAs

structure. They found that both too low and too high temperatures can degrade the meta-buffer quality. Thus it is important to know the optimum temperature range and grow within that range. Leitz et al. [83] also found that lowering growth temperature increases TDD. Substrate orientation was also shown an important factor for dislocation kinetics. On-axis sample provided the best result as all 8 slip-systems were active for dislocation reduction reactions.

Lee and Fitzgerald [84] showed that continuous grading offers better quality of MBLs than step-grading. Their result demonstrates that higher grading rates increases surface roughness, as well as dislocation-dislocation and surface-dislocation interaction which lead to lower dislocation glide velocities and thereby higher TDDs. For practical limitation of the thicknesses of epilayer, they took the approach to use higher grading rate initially and decreased the grading rate gradually and found better quality MBLs than using constant grading rate of similar thickness buffer layers. They also showed that MBLs grown on off-axis substrate shows more defects than MBLs grown on on-axis substrate. By lowering the growth temperature, phase separation can be suppressed, but dislocation glide-velocity also reduces.

By growing quantum dots or quantum wells (QWs) on top of a meta-buffer, emission in the range of 1.45-1.55μm could be achieved [85-88]. Tångring et al. [47] fabricated 1.25-1.29 μm QW lasers on top of InGaAs MBs. They used Be-doping in graded buffer layers to improve the performance [58]. Surface roughness was also reduced by Be-doping. Song et al. [89] also showed the beneficial effect of Be doping. Their work also confirmed the existence of thicker clean (free of MDs) region for lower grading rate. Bing-Peng et al. [90] also achieved 1.55 μm emission from the QWs grown on top of InGaAs metamorphic buffers. They found significant improvement of both surface and optical quality by using Sb as a surfactant during the growth of MBs. Moreover, Sb incorporation into QWs also has the advantage of red-shifting the PL peak wavelength. Hence it indicates that it is possible to achieve long wavelength lasers grown on a GaAs substrate if it is possible to optimize the growth of the meta-buffer. Thus different ways

of growing meta-buffer are continuously being investigated. It has also been shown that it can be beneficial to grow a low-temperature InP layer for InAsP/InP system [27, 33]. Moreover the residual strain of the final layer can be engineered by using an overshooting layer [91]. By overshooting layer it means that to grow the MBs upto the composition whose bulk lattice constant is higher than the metamorphic pseudo-substrate. For example, the MB layers is grown upto $In_zGa_{1-z}As$ and then the final layer of composition $In_xGa_{1-x}As$ is deposited on top of that, where z>x. By changing the thickness of the overshooting layer it is possible to make the final layer either tensile or compressive. A new approach is proposed by Yang et al. [92] where a $In_xGa_{1-x}As$ graded buffer is first grown followed by the growth of a graded $In_xGa_{1-x}P$ to reach to the lattice constant of InP.

Whereas significant amount of work has been done for ternary graded system in the III-V material system, very little work could be found for a graded quaternary alloy system. Kirch et al. [93] employed graded $In_{0.485}Ga_{0.515}P_ySb_{1-y}$ alloy on a GaAs substrate and found that the surface roughness is lower than for a graded InGaAs structure. They also found lower relaxation for the quaternary. Carlin [70] used a graded $In_{0.49}Ga_{0.51}As_yP_{1-y}$ alloy. He used a higher rate of transition of lattice constant at the hetero-interfaces. The relaxation was found to be significantly lower for this case than the ternary case. Although the anion graded quaternary system is easier to grow as it takes less time to switch the group V pressure than the temperature of group III Knudsen cells, composition control of these quaternaries are more difficult as the sticking coefficient of group V element is not unity but rather dependent on growth temperature and on particular species (As or P) [94].

5.4 Sample growth

Four compositionally graded buffers were grown by MBE on 2-inch diameter epiready, Si-doped n-type GaAs (001) $\pm$ 0.1° wafers. The details of the growth were same as described in section 4.4. All the samples have the same value of partially relaxed lattice constant of the final buffer layer which is 5.73195Å. Thus the lattice mismatch

strain between the final buffer layer and substrate is 1.37%. Table 5-1 shows the layer-by-layer design of the four samples. Sample 1 and 2 are the $In_xGa_{1-x}As$ linearly and logarithmically step-graded structures, respectively; and sample 3 and 4 are the $In_{.485}Ga_{.515}As_yP_{1-y}$ linearly and logarithmically step-graded structure, respectively.

<table>
<tr><td rowspan="2">500 nm $In_{0.194}Ga_{0.806}As$</td><td rowspan="2">500 nm $In_{0.194}Ga_{0.806}As$</td><td>500 nm $In_{.485}Ga_{.515}As_{0.40}P_{0.60}$</td><td>500 nm $In_{.485}Ga_{.515}As_{0.40}P_{0.60}$</td></tr>
<tr><td>100 nm $In_{.485}Ga_{.515}As_yP_{1-y}$ (9 steps with y incremented 0.04/step)</td><td>100 nm $In_{.485}Ga_{.515}As_yP_{1-y}$ (9 steps where y=0.167log(z); z is from 2 to 10)</td></tr>
<tr><td>100 nm $In_xGa_{1-x}As$ (9 steps with x incremented 0.0194/step)</td><td>100 nm $In_xGa_{1-x}As$ (9 steps where x=0.0809log(z); z is from 2 to 10)</td><td>100 nm $In_{.485}Ga_{.515}P$</td><td>100 nm $In_{.485}Ga_{.515}P$</td></tr>
<tr><td>100 nm GaAs buffer</td><td>100 nm GaAs buffer</td><td>100 nm GaAs buffer</td><td>100 nm GaAs buffer</td></tr>
<tr><td>n-GaAs (001) substrate</td><td>n-GaAs (001) substrate</td><td>n-GaAs (001) substrate</td><td>n-GaAs (001) substrate</td></tr>
<tr><td>**Sample 1 (500°C)**</td><td>**Sample 2 (500°C)**</td><td>**Sample 3 (470°C)**</td><td>**Sample 4 (470°C)**</td></tr>
</table>

Table 5-1: Details of the metamorphic structures grown

Linear or logarithmically step-graded structure means that the strain is varying in linear and logarithmic fashions (as shown in Fig 5-1). Thus for the logarithmic case the strain gradient is higher initially and gradually decreases with layer thickness, whereas it is same for all layers in linear case. It should be noted that samples 1 and 2 were grown at 500°C while sample 3 and 4 were grown at 470°C. This is because, significant phase separation has been observed for quaternary sample grown at 500°C, which is evident in Fig 5-2). By lowering growth temperature at 470°C, phase separation was reduced significantly.

For the quaternary system the In/Ga ratio was kept fixed for all the layers. Thus it becomes basically anion-graded metamorphic buffer. Compositional control of the quaternary material system is more complex than ternary, because the group V sticking coefficient has the dependency on group III composition [94]. Thus for every

combination of group III composition, it would be necessary to run a new set of calibrations. For this work, $In_{.485}Ga_{.515}P$ was selected as a starting point as it is lattice matched to GaAs. As group III elements have unity sticking coefficient at the growth temperature used here, it has been assumed that addition of As will not affect the Ga/In ratio.

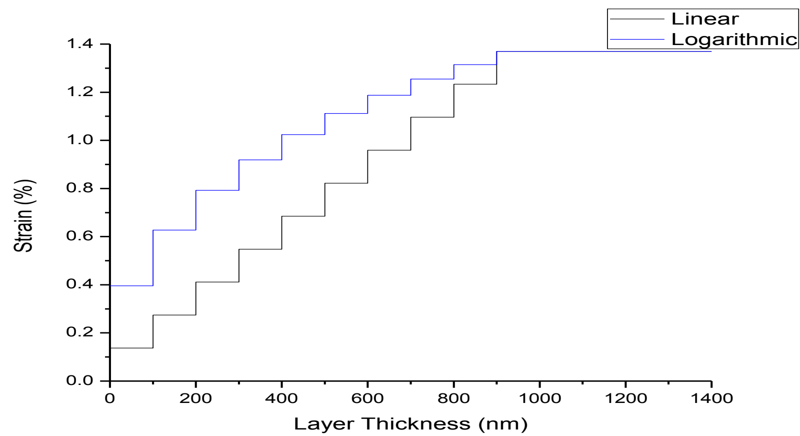

Fig 5-1: Variation of strain with layer thickness for linear and logarithmically graded sample.

Fig 5-2: Cross-sectional bright field TEM image of linearly-graded quaternary alloy grown at 500°C.

To assess the optical quality of the metamorphic layer, an InGaAs quantum well was grown in the top metamorphic layer of each sample. General structures for all of the quantum wells are shown in Table 5-2. All the epitaxial layers grown on top of the metamorphic substrates have a lattice constant equal to the in-plane lattice constant of the meta-substrate. The growth temperature was ~500°C for all the layers. The Ga/In ratio was kept same as the graded layers to avoid the growth of a new set of calibration samples.

25 nm $In_xGa_{1-x}P$
100 nm $In_{.485}Ga_{.515}As_yP_{1-y}$
7 nm $In_xGa_{1-x}As$
100 nm $In_{.485}Ga_{.515}As_yP_{1-y}$
100 nm $In_xGa_{1-x}P$
100 nm $In_{.485}Ga_{.515}As_yP_{1-y}$ or $In_xGa_{1-x}As$ of lattice constant, a(depending on whether the graded buffer is quaternary or ternary, respectively)
Metamorphic substrate (in-plane lattice constant, a)

Table 5-2: Structural details of the layers grown on top of meta-substrate.

Lattice relaxation and tilt of the sample was characterized by XRD and surface roughness and crosshatch were investigated by AFM. An etch pit density experiment was done to quantify the threading dislocations. DOP measurements were used to analyze the strain distribution within the QW and TEM was used to see the details of dislocation distributions in the layers. PL was used to verify the optical quality of the buffer layers.

5.5 X-ray analysis

(004) x-ray scans were performed for all the samples in both <110> and <1$\bar{1}$0> directions. Two different scans were performed for all samples; an ω-2θ scan (ω_{rel}=0, ω_{rel} is the tilt of the sample) and an ω-scan (ω_{rel} has the value obtained from ω-2θ scan). ω-2θ scans, where both substrate and detector were moved, provides strain information and ω-scans, where only the substrate is tilted, provides information about tilt and mosaicity. The width of an ω-scan peak is also known to be related to the threading dislocation density [95]. For an ω-scan, the x-ray system was aligned to the peak corresponding to

the top metamorphic layer and also to the layer grown on top of the meta-substrate. Although the in-plane lattice constant was approximately equal for both, the difference arises due to the strain difference of two layers, as the lattice constants in the growth direction were not equal. 2-dimensional reciprocal space maps (RSMs) were also obtained for all the samples. Results from x-ray analysis are tabulated in Table 5-3.

Sample Number	Tilt (arc sec)		FWHM of buffer layer (arc sec)		FWHM of layers grown on top of meta-buffer (arc sec)		Relaxation (%)	
	<110>	<1$\bar{1}$0>	<110>	<1$\bar{1}$0>	<110>	<1$\bar{1}$0>	<110>	<1$\bar{1}$0>
Sample1	-30	57	1066	1054	1185	753	80.13	78.82
Sample2	-862	-120	722	689	489.8	620.5	80.15	79.05
Sample3	-69	-1014	598	1196	459.4	1247.7	52.23	58.15
Sample4	-50	1342	638	899	629	908.6	57.68	60.86

Table 5-3: Results from x-ray analysis

Fig 5-3 shows (004) *ω-2θ* scans for sample 1 and 3, where the x-ray scans were done on <110> direction. It can be seen that for quaternary sample, there exists an additional peak, at around 500 arc sec, just after the substrate peak, in addition to the substrate and terminal buffer layer. All the (004) *ω-2θ* scans from quaternary graded layers exhibited this property, whereas the extra peak was absent for ternary graded layers. This extra peak indicates that for quaternary system, first few layers are strained, whereas for the ternary, the layers are relaxed from initial layers. This feature can be clearly seen in the cross-sectional TEM images in Fig 5-10. Thus, quaternary alloys have higher barrier for MD generation than ternary alloys.

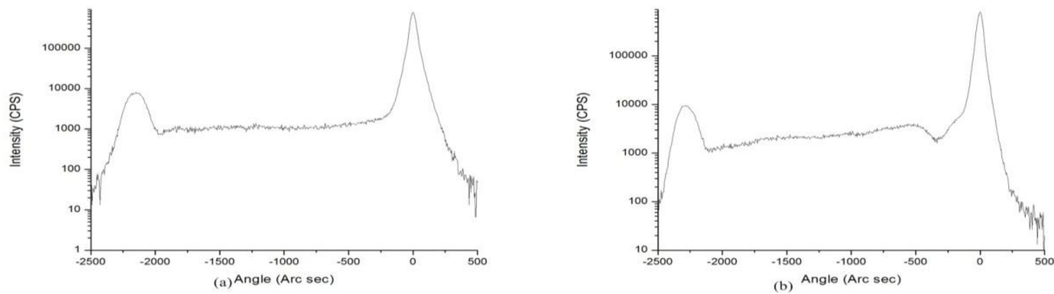

Fig 5-3: (004) ω-2θ x-ray scans around <110> direction for (a) linear $In_xGa_{1-x}As$ and (b) linear $In_{.485}Ga_{.515}As_yP_{1-y}$ metamorphic layers.

Crystallographic tilt is often observed in mismatched hetero-epitaxial systems [34, 76, 78, 96]. Fig 5-4 Shows (004) RSMs of the MBLs for orthogonal <110> directions. Asymmetric crystallographic tilt in orthogonal <110> directions has been observed for all samples except linearly graded $In_xGa_{1-x}As$ sample. Table 5-3 gives the magnitude and direction of tilt of each sample. Greater amount of tilts were seen in <1$\bar{1}$0> direction for quaternary graded samples (Fig 5-4 (f) and (h)). Logarithmically graded ternary sample showed tilt in the <110> direction (Fig 5-4 (c)). Linearly graded ternary sample also showed tilt initiation in the initial part of strain relaxation, but tilt vanished as the relaxation grows (Fig 5-4 (a)). The FWHM also seems to have a correlation with tilt, as FWHM of the terminating buffer layers also shows asymmetry in two orthogonal <110> directions for the samples where asymmetric tilts have been found. It can be seen from Table 5-3 that higher FWHM or mosaicity has been obtained for the directions which have higher magnitude of tilt.

Tilted epitaxial growth is mainly attributed to asymmetry of MD generation [96]. Thus the magnitude and direction of tilt is related with the nature of relaxation process. An unequal distribution of dislocations in different slip planes results in tilt in different directions. An interesting observation is that logarithmic grading introduces larger tilt than linear grading. This might be due to the higher number of MDs generated initially for the logarithmic case, due to the greater initial misfit stress. Thus during the initial relaxation, dislocations would be more widely spaced in the linearly graded system. Therefore, all the eight slip systems have enough time to participate [76]. Whereas for the logarithmic graded structures, the interaction between dislocations is higher in first few layers, which in turn increases the magnitude of the tilt. Häusler et al. [97] also showed that magnitude of tilt depends on the values of misfit. Fig 5-4 (f) and (h) clearly show that initially when the epitaxial layers are elastically strained, there is no tilt and the tilt starts when the layer starts to relax.

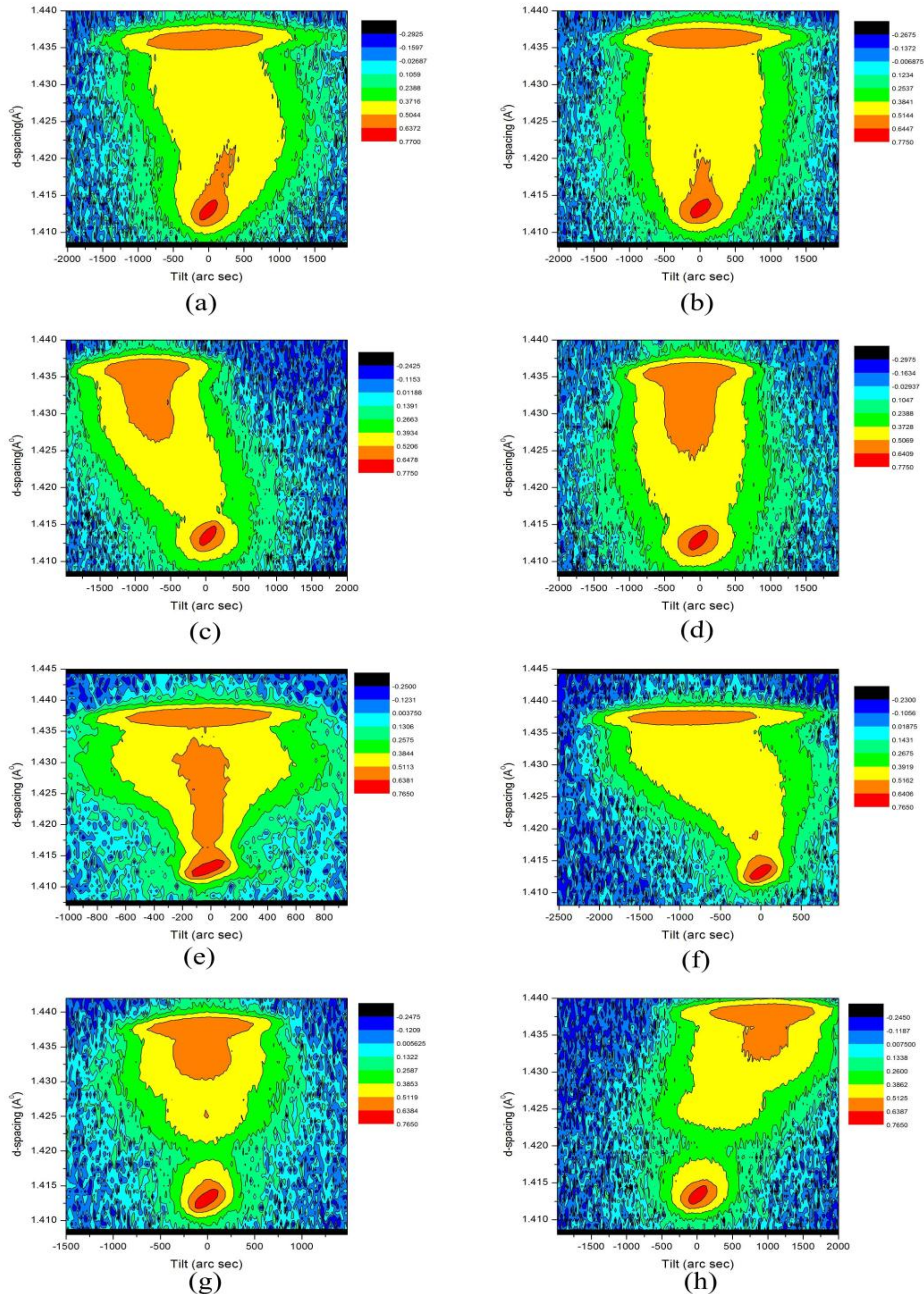

Fig 5-4: (004) Reciprocal space maps for linearly graded $In_xGa_{1-x}As$ (a) in $\langle 110 \rangle$ and (b) in $\langle 1\bar{1}0 \rangle$ directions; logarithmically graded $In_xGa_{1-x}As$ (c) in $\langle 110 \rangle$ and (d) in $\langle 1\bar{1}0 \rangle$ directions; linearly graded $In_{.485}Ga_{.515}As_yP_{1-y}$ (e) in $\langle 110 \rangle$ and (f) in $\langle 1\bar{1}0 \rangle$ directions and logarithmically graded $In_{.485}Ga_{.515}As_yP_{1-y}$ (g) in $\langle 110 \rangle$ and (h) in $\langle 1\bar{1}0 \rangle$ directions.

It can be seen from the intensity distribution of the RSM of sample 2 and 4 (Fig 5-4 (c), (d), (g) and (h)) that the peaks of final metamorphic buffer layers are wider in d-space. This is an indication that for sample 2 and 4, last few layers are strained and hence not relaxed for the logarithmic graded samples. Fewer MDs are introduced in the last few layers which in turn increases the intensity. Thus the dislocation free thickness is higher for logarithmic grading approach.

For logarithmic grading, the FWHM of the final buffer layer and the lattice matched layers, grown on top, is less than the linear grading case. It has been shown that this broadening effect is mainly due to the mosaicity and not due to different lattice constants, as the entire layer has nominally the same lattice constant [98] This indicates that the logarithmically graded sample has less mosaicity, which means superior crystal quality. For the ternary system, the FWHM is almost similar in both directions, whereas it is smaller in <110> direction for quaternary graded system. This can be considered to be due to the mobility difference of α and β dislocations, discussed in Chapter 4.

Relaxation was almost similar irrespective of grading laws (linear or logarithmic). But relaxation of quaternary layers is significantly lower than ternary layers. One reason for the lower relaxation might be the lower growth temperature. Linear quaternary graded sample grown at 500°C showed higher relaxation. 93% and 85% relaxation were seen in <1$\bar{1}$0> and <110> directions, respectively. Asymmetry of relaxation in orthogonal <110> directions is mainly attributed in the mobility difference of α and β dislocations [34, 67, 72].

5.6 Atomic Force Microscopy (AFM)

It is important to characterize the surface morphology of the graded buffers, as future device structures will be grown on top of these buffer layers. As it is described in the previous chapter, surface observation also gives information about the strain distribution in the heteroepitaxial layer. Fig 5-5 shows AFM scans of 5x5 μm^2 of all samples. There are no significant differences of surface roughness among them. RMS calculation of roughness shows that quaternary graded samples have slightly lower roughness than the

ternary graded ones. The grading law seems to have no significant effect on roughness. This might be due to the lower growth temperature of the quaternary. Quaternary samples showed more spotty patterns (Fig 5-5(c) and (d)) than ternary samples. This is due to the higher residual strain of the top metamorphic layers for quaternary graded samples. To see the cross-hatch pattern clearly 15x15 μm^2 scans were done (Fig 5-6 shows 3D view of samples 1 and 3). All of the samples showed typical CH pattern, which is the characteristics morphology of metamorphic systems.

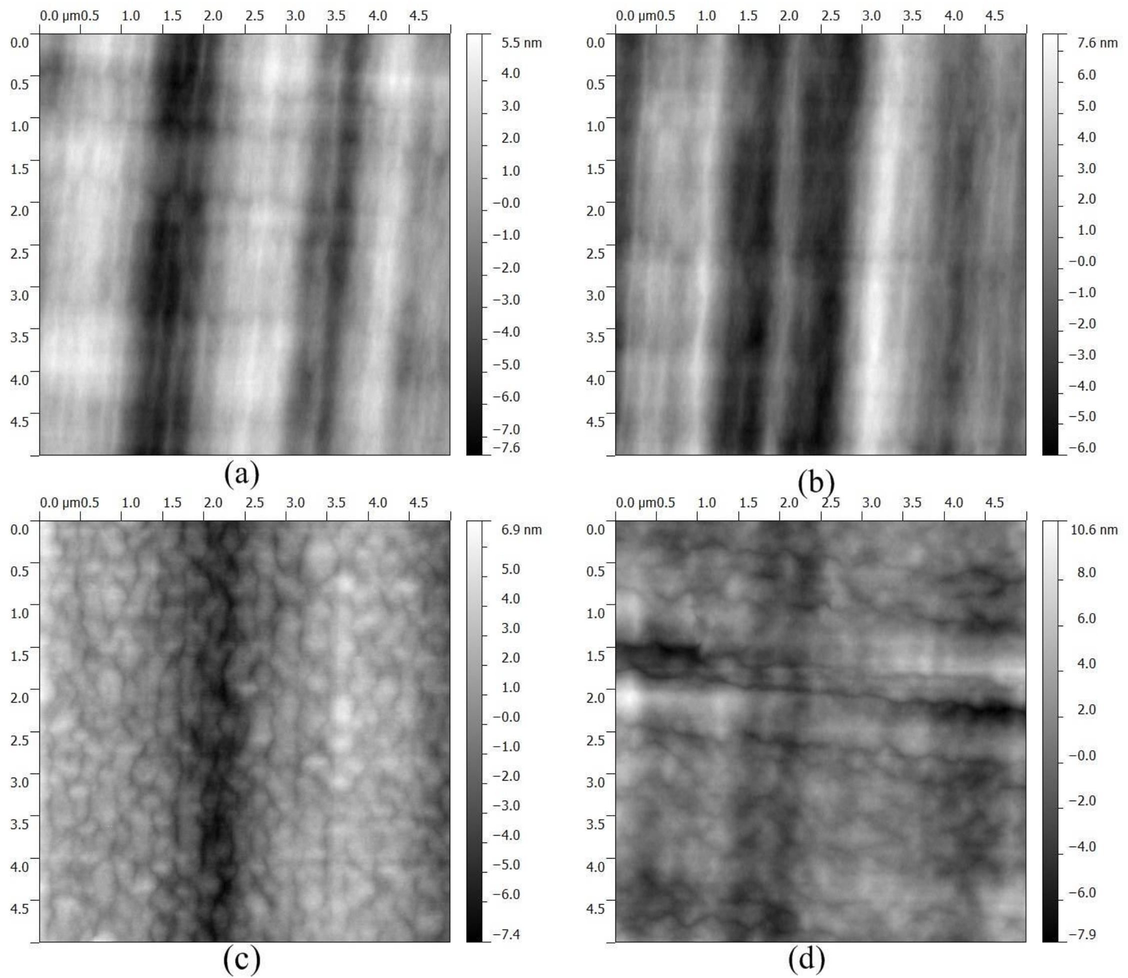

Fig 5-5: 5x5 μm^2 AFM images of (a) sample 1, (b) sample 2, (c) sample 3 and (d) sample 4.

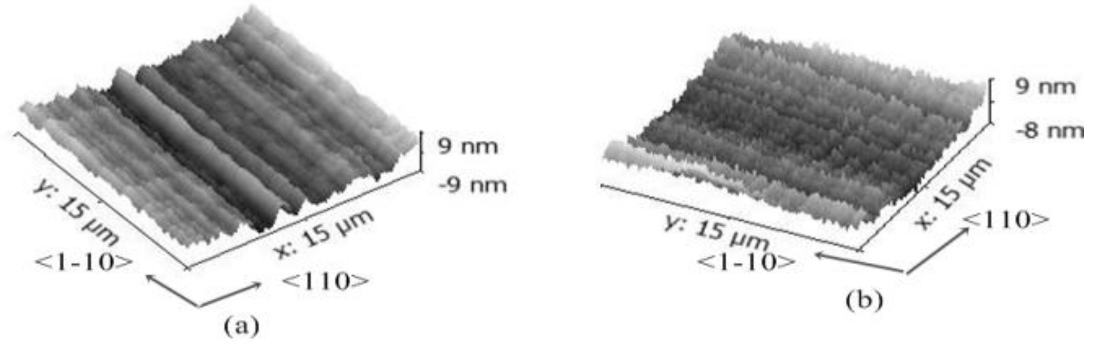

Fig 5-6: 3-D view of 15x15 μm^2 of AFM images for (a) sample 1 and (b) sample 2.

Table 5-4 lists the parameters obtained from AFM images. It can be seen that the wavelength of CH is reduced for sample 3 and 4. CH wavelength is related to the strain of the epitaxial layer. The critical wavelength of surface undulation is inversely proportional to the square of the strain, $\lambda_{cr} \propto \frac{1}{\varepsilon^2}$ [39], where λ_{cr} is the critical wavelength of undulation and ε is the mismatch strain. As the relaxation for sample 3 and 4 is lower, the strain existing on the terminating buffer layer is higher, which increases the wavelength of the undulations.

Sample number	Growth temperature	Avg. Peak to valley distance (nm)		Avg. Wavelength (µm)		RMS roughness
		<110>	$<1\bar{1}0>$	<110>	$<1\bar{1}0>$	
1	500 °C	8.2	0.65	2.2	1.01	2.70 nm
2	500 °C	9.2	0.6	2.15	0.97	2.67 nm
3	470 °C	5.1	2.6	1.15	0.6	2.32 nm
4	470 °C	5.12	2.58	1.43	0.7	2.16 nm

Table 5-4: AFM measurement of different parameters.

The anisotropy of the average peak to valley distance is higher for samples 1 and 2. This anisotropy is normally attributed to the differences of group III adatom incorporation rate in A-type and B-type steps [41]. At higher growth temperature the

differences of incorporation rate in two orthogonal <110> directions are higher; hence the average peak to valley ratio increases.

From above discussion, we can see that surface morphology is almost similar for logarithmic and linear grading. Although there are differences between ternary and quaternary grading, the relative amount of differences is not significant to conclude that it is not due to the growth temperature.

5.7 Etch Pit Density

The Etch pit density (EPD) is a measure for the quality of epitaxial layers. Generally an etch solution is selected which has higher etch rate at dislocations, and hence will produce pits. To quantify threading dislocations, etch pit measurements were done. For $In_xGa_{1-x}As$ metamorphic buffers an A-B etch [99] (A: 40 ml H_2O:40 g CrO_3, B: 40 ml H_2O:0.3 g $AgNO_3$; A:B (3:1)) was applied. Then HF was mixed with A-B solution in a ratio A-B etch:HF (1:3). HF was used to slow the etch rate. Samples 1 and 2 were kept in this solution for 10s at 60°C. For the $In_{.485}Ga_{.515}As_yP_{1-y}$ metamorphic buffer the etchant was changed to HCl:HNO_3:H_2O (6:1:6) [99]. Samples 3 and 4 were kept in this solution for 90s at 25°C. Fig 5-7 shows typical optical microscope images of the buffer layers after keeping them in the etch pit solution. Etch pits can be seen clearly, and were counted manually.

Table 5-5 shows etch pit density obtained from experiment. Threading dislocation densities are quite low in the final buffer layer. It should be noted that the etch pit density is not uniform over the sample. The value given here are the average values obtained from four images taken in different areas of the sample. For a particular material system (ternary or quaternary) logarithmic grading gives lower TDD.

As the etch pits are small in size, they need to be counted under a microscope. Thus for the etch pit analysis, a small proportion ($100\times100\mu m^2$) was measured. As a result, EPD measurement represents a small statistical sampling of the surface area. Hence, calculation of statistical error becomes important. Rose et al. [100] showed that Poisson

distribution can be used to analyze dislocation distribution. The EPD, which was calculated as the total number of counted pits, x, divided by the total imaged area, should have a standard deviation of $x^{1/2}$/area [101]. The statistical error in Table 5-5 corresponds to one standard deviation. However, it should be noted that there are several other sources of error. The most obvious is the inhomogeneous distribution of the etch pits. Therefore 5 different areas were chosen randomly to calculate EPD and the average were taken. However counting of etch pits themselves is also difficult due to the small pit size.

Sample number	Etch pit density (per cm^2)	Statistical error
Sample 1	3.9×10^5	6.2×10^4
Sample 2	3.2×10^5	5.6×10^4
Sample 3	5.6×10^5	7.5×10^4
Sample 4	1.8×10^5	4.2×10^4

Table 5-5: Etch pit density measurement

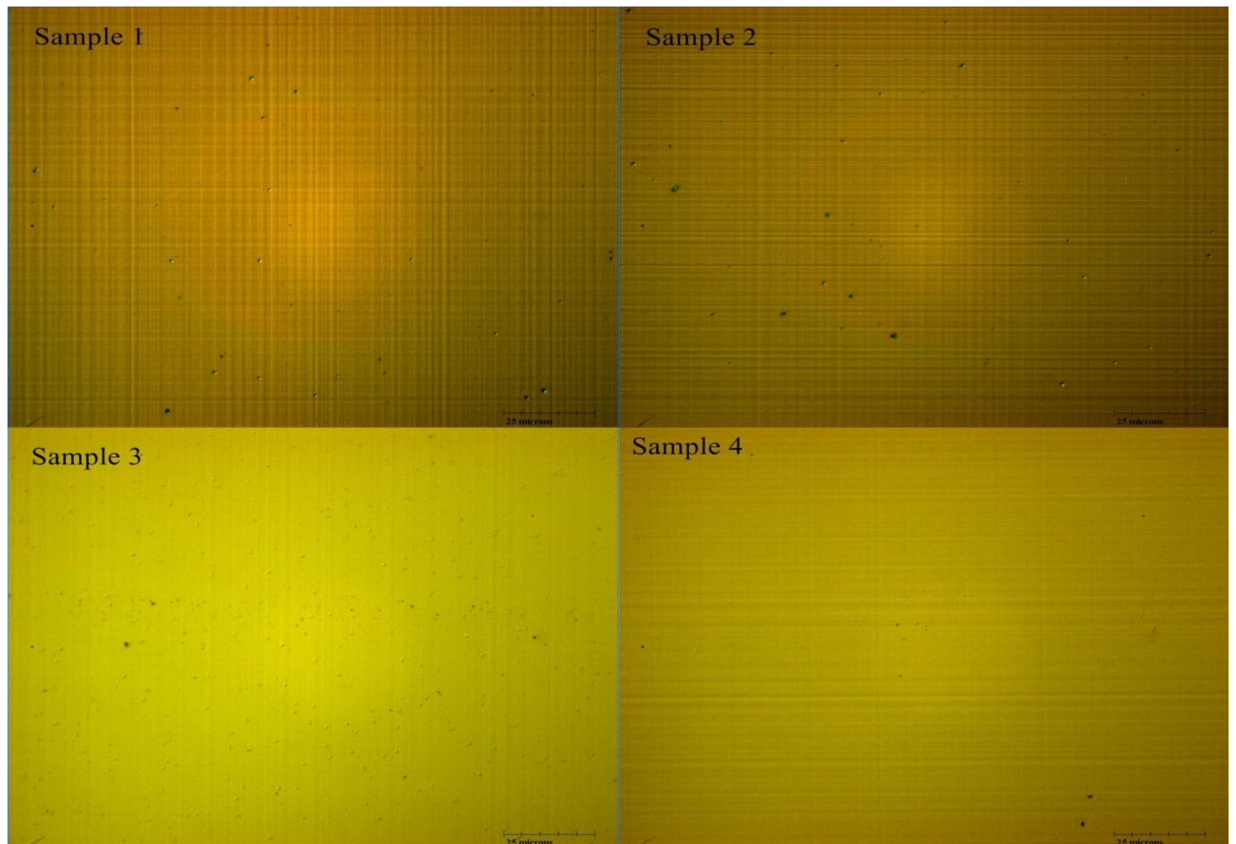

Fig 5-7: Optical microscope images of the buffer layers after etching.

5.8 Photoluminescence

Room temperature (RT) PL has been achieved from the QWs grown above each metamorphic structure (shown in Fig 5-8). RT-PL scans were done by using Si-detector. The sensitivity of the Si-detector is gradually decreasing with wavelength over the range of interest. The low PL intensity, combined with the lower sensitivity, made the PL signal very noisy. Hence FFT filtering was done to remove high-frequency noise components. As the PL was obtained in room temperature, it is an indication of the good quality epitaxial layers; because if the epitaxial layers have a high TDD, no PL should be observed at RT. Due to the different detector sensitivity, intensity comparison between ternary and quaternary graded samples is not possible. But as the logarithmic and linear graded samples have similar peak energy, intensity comparison become possible for those. The PL-intensity was slightly higher for the logarithmic graded sample than linear graded one; although it is not significant. Table 5-6 shows FWHM of RT-PL spectra. The FWHM values are larger for quaternary graded samples. PL broadening can be attributed to impurities, lattice defects and phase separations [102]. Impurity effects can be ignored as no intentional impurity was added during growth.

Sample 1	Sample 2	Sample 3	Sample 4
23.95 nm	23.2 nm	36.34 nm	37 nm

Table 5-6: FWHM of RT-PL spectra

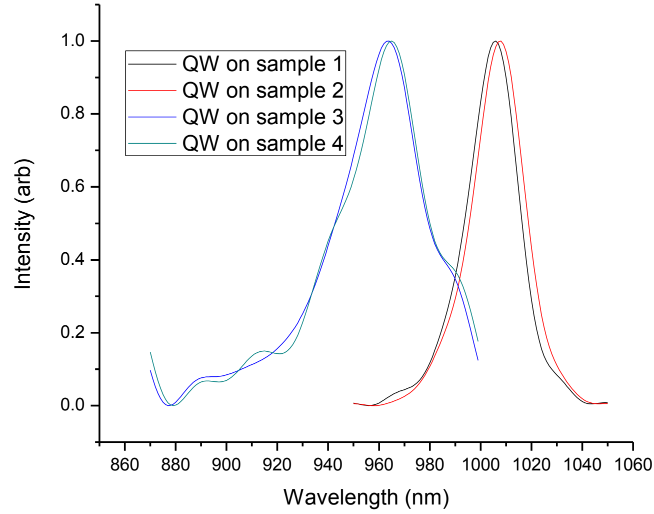

Fig 5-8: RT-PL spectra from the QW grown above metamorphic buffers.

Besides roughness or any lattice defects, phase separation is a mechanism to produce PL broadening. If a statistical fluctuation of the composition exists in the meta-buffer, it can propagate all the way to the QW, which leads to fluctuations in the bandgap. The temperature dependence of PL peak position for homogeneous material is given empirically by the Varshni equation [103]:

$$E_g(T) = E_{g0} - \frac{\alpha T^2}{T+\beta}$$

where, $E_g(T)$ is the bandgap at TK, and E_{g0} is the bandgap at 0K, T is the temperature, α and β are the empirical constants. From the equation, it is evident that the bandgap decreases at higher temperature.

It has been shown [104] that, if the composition is not uniform in the epitaxial layer, then the bandgap will be lower at low temperature (<~100K) than would be expected from Varshni equation. This occurs because the period of lateral composition modulation is much smaller than the carrier diffusion length, thus carriers will trap into the lower bandgap region at lower temperature, which will red-shift the PL peak energy at low temperature. As the temperature is increased, carriers acquire enough energy to

overcome the barrier due to phase separation. At high temperature, three peaks from three regions (shown in Fig 5-9) will then coalesce into one peak which broadens the PL peak.

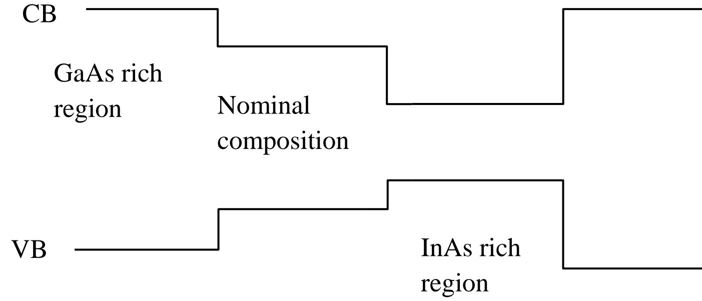

Fig 5-9: Bandgap model for phase separated region.

The PL peak energy was determined both at 9K and 300K. To remove noise from the spectra, a low pass FFT filter was applied. The difference of these two bandgaps will be:

$$\Delta E_g = E_g(T=9) - E_g(T=300) = \frac{\alpha 300^2}{300+\beta} - \frac{\alpha 9^2}{9+\beta}$$

The values of $\alpha = 5.58\text{x}10^{-4}$ and $2.5\text{x}10^{-4}$ and $\beta = 220$ and 75 for GaAs and InAs respectively [105]. Vegard's law was applied to find α and β values for the QWs. The results of the calculation were summarized in Table 5-7. Although, the differences between calculated and measured values are within experimental uncertainty for sample 1 and 2, for sample 3 and 4, ΔE_g is less than expected, which indicates the existence of composition modulation or phase separation in the QW grown on top of quaternary graded metamorphic pseudosubstrate.

Sample number	QW composition	α (eV/K)	B (K)	$\Delta E_{g,calculated}$ (meV)	Measured values (meV)		
					E_g, at 9K	E_g at 300K	ΔE_g
1	$In_{.154}Ga_{.846}As$	$5.11\text{x}10^{-4}$	197.67	91.8	1322	1234	88
2	$In_{.153}Ga_{.847}As$	$5.11\text{x}10^{-4}$	197.82	91.7	1319.3	1231.7	87.6
3	$In_{.112}Ga_{.888}As$	$5.24\text{x}10^{-4}$	203.76	93.4	1368	1290.5	77.5
4	$In_{.128}Ga_{.882}As$	$5.22\text{x}10^{-4}$	202.89	93.2	1363.5	1289.1	74.4

Table 5-7: Calculation of band-gap difference between 9K and 300K.

5.9 Degree of Polarization

As the PL obtained was only from the QW and not from the meta-buffer, it is impossible to check the strain distribution of the meta-buffer; because to get the DOP map of an epilayer, PL emission is necessary from that layer. DOP analysis was used to see the QW only. DOP scans were performed on both (001) plane and the <110> facet. As all the QWs were lattice matched and have same thickness, (001) DOP scan will give information about interface roughness and the facet scan will show the relative amount of stress in the substrate.

For the ideal QW, the interface will be smooth. However, it is almost impossible to produce a completely smooth interface in MBE. This structural perturbation in the interface affects the electronic states [106]. It has been shown [62] that the impact of the anisotropic strain increases with the decreasing QW thickness as the relative volume of the interfacial perturbation with respect to QW increases. Now, from equation 2-7

$$DOP_{001} = -C_{\varepsilon}(\varepsilon_{110}-\varepsilon_{1-10})$$

Here, ε_{110} and ε_{1-10} are the normal components of strain along <110> and $<1\bar{1}0>$ directions respectively and C_{ε} is the calibration constant.

For a symmetrical biaxially strained system, the DOP_{001} should be zero. But this is not the case in this experiment. The average values were tabulated in Table 5-8. It should be noted that DOP_{001} is higher for the quaternary graded sample, which indicates that the anisotropy of strained bonds in the interface is greater [62]. It was speculated by Lakshmi et al. [62] that the strained Ga-P bonds have the highest contribution for the non-zero value of DOP_{001}. For the quaternary graded samples QWs contain more Ga than the ternary graded samples as the lattice constant of QW is smaller for quaternary graded samples. Hence during the change from only As flux to combined As and P flux, more strained Ga-P bonds created, which in turn increases the value of DOP_{001}. Facet scans can give the stress induced in the substrate also, as DOP signals also arise from the GaAs substrate. Higher the DOP values in the substrate means higher the stress induced and a

negative sign implies tensile stress. As the grown layers are all compressively strained, the substrate is expected to exhibit some tensile strain. From Table 5-8, it is seen that substrates on which quaternary graded buffers are grown are more strained than for ternary graded buffers. This result is consistent with the x-ray data. Ternary buffers begin to generate MDs from the first layers, whereas quaternary buffers have first few layers strained. In the next section, this is confirmed by TEM observation.

Parameter	Sample 1	Sample 2	Sample 3	Sample 4
DOP_{001} (%)	5.4	6	9.9	16.4
DOP in substrate	-0.4	-0.05	-1.35	-1.3

Table 5-8: Values obtained from DOP scan.

5.10 Transmission Electron Microscopy (TEM)

To view the dislocation distribution in the epitaxial layers cross-sectional TEM (X-TEM) samples were prepared. Fig 5-10 (a-d) shows X-TEM images for the samples. The meta-substrate appears free of threading dislocations (less than the detectable limit of TEM ($10^6/cm^2$)) for all four samples. It is evident that for quaternary grading the first few layers are strained and the layer starts to relax after some layer and the dislocations are not distributed over in whole graded region, where as for ternary graded buffers, MDs can be seen at the very first layers and are distributed more uniformly. Although the strain distribution in both ternary and quaternary graded samples are similar, the MD distribution appears significantly different. The exact physical reason behind this is yet to be solved. Logarithmic graded sample have larger area which is free of threading dislocations. This explains the elongated region in d-space of RSM.

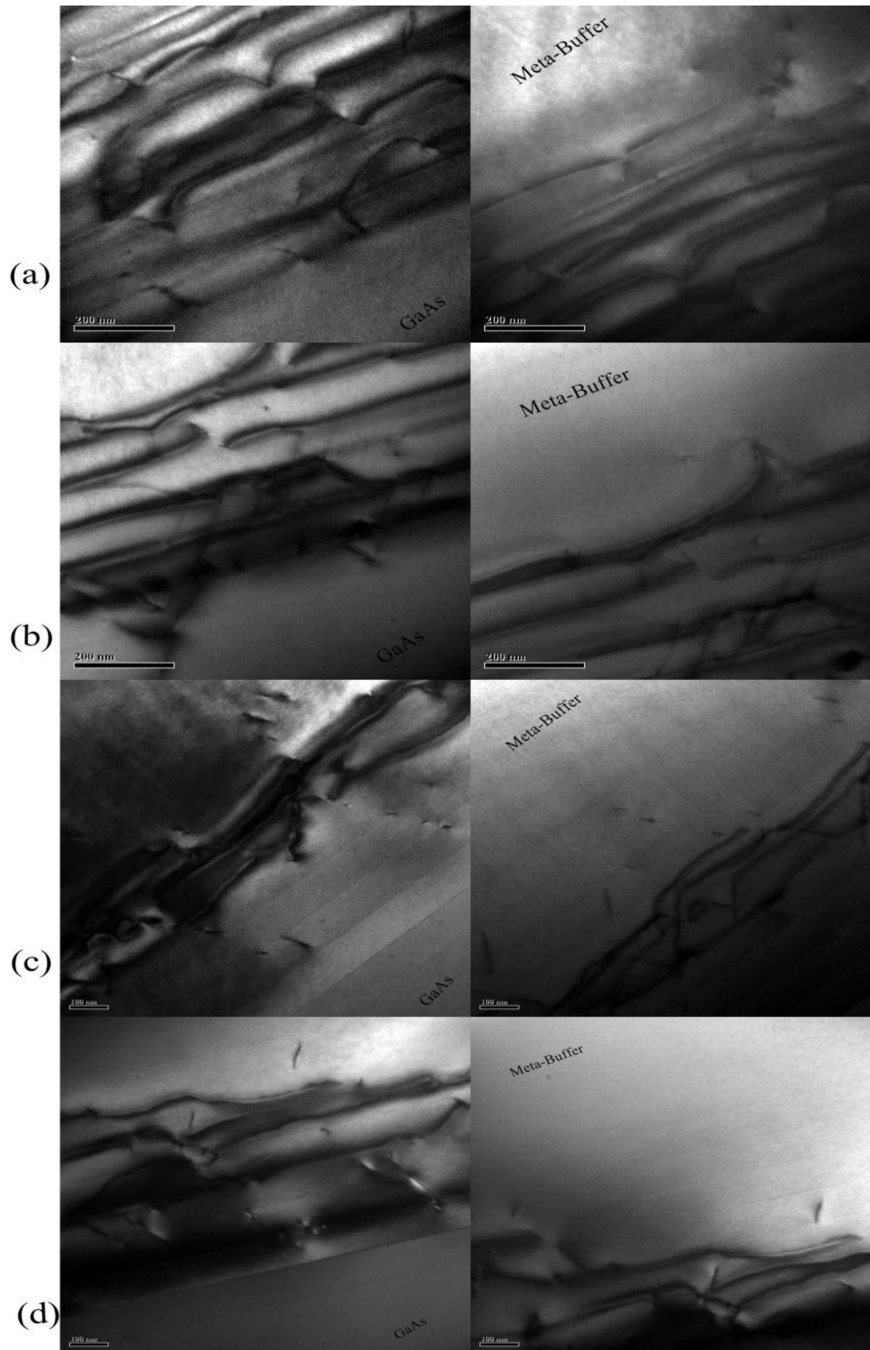

Fig 5-10: Bright field X-TEM images of (a) sample 1, (b) sample 2, (c) sample 3 and (d) sample 4. Left images are for the first few layers and right images are the last few layers.

Although quaternary graded samples have lower relaxation, the existing TDD obtained from EPD is comparable with the ternary graded samples. It can be seen (Fig 5-10 (c) and (d)) that for quaternary graded sample, the first layer which contains high

density of dislocations have higher strain compared with the ternary graded samples (Fig 5-10 (a) and (b)). Hence it might be expected that the first layer, which have high density of dislocations, contains higher number of dislocations for quaternary graded samples. Thus pinning of dislocations should be higher, which would increase the threading dislocations [80]. In some instances for samples 1 and 2, a few dislocations were observed to enter the substrate (not shown in figure). Legoues et al. [107] showed that this phenomenon is an indication that the nodes of intersecting MDs act as Frank-Read source. They showed that activation of Frank-Read source reduces the dislocation pinning. Thus the dislocations become free to move all the way toward the edge of the sample and thus reduce the TDD.

To investigate about the existence of composition modulation diffraction contrast TEM imaging was done by using g_{200} diffraction vector, as this has been shown [108] to be sensitive on chemical composition. Practically the samples were tilted slightly to enhance the image contrast. Fig 5-11 shows X-TEM images of QW grown on top of meta-substrate for sample 2 and 3. Lateral composition modulation was seen for quaternary graded sample (Fig 5-11(b)), while ternary graded sample have uniform composition (Fig 5-11(a)). As the growth conditions were similar for both samples, it can be said that the existence of composition modulation in QW is due to the existence of composition modulation in MBLs. Thus QW grown on top of quaternary graded buffer layers would have lower quality. This also explains the broadening of PL peak from quaternary graded sample.

For ideal case of InGaAsP growth, it has been assumed that all four elements are distributed randomly. For such homogeneous quaternary alloys, the In-As bonds become compressed and the Ga-P bonds become elongated, and it has been shown thermodynamically [109] that a driving force exists for InGaAsP layers to become separated into two distinct phases with compositions of the end point binary compounds. Since In-As is the longest bond and Ga-P is the shortest of the four binary constituent bonds, they are more strained than others. Thus the production of In-As and Ga-P rich

regions is favored as it reduces the system energy by minimizing the number of strained bonds.

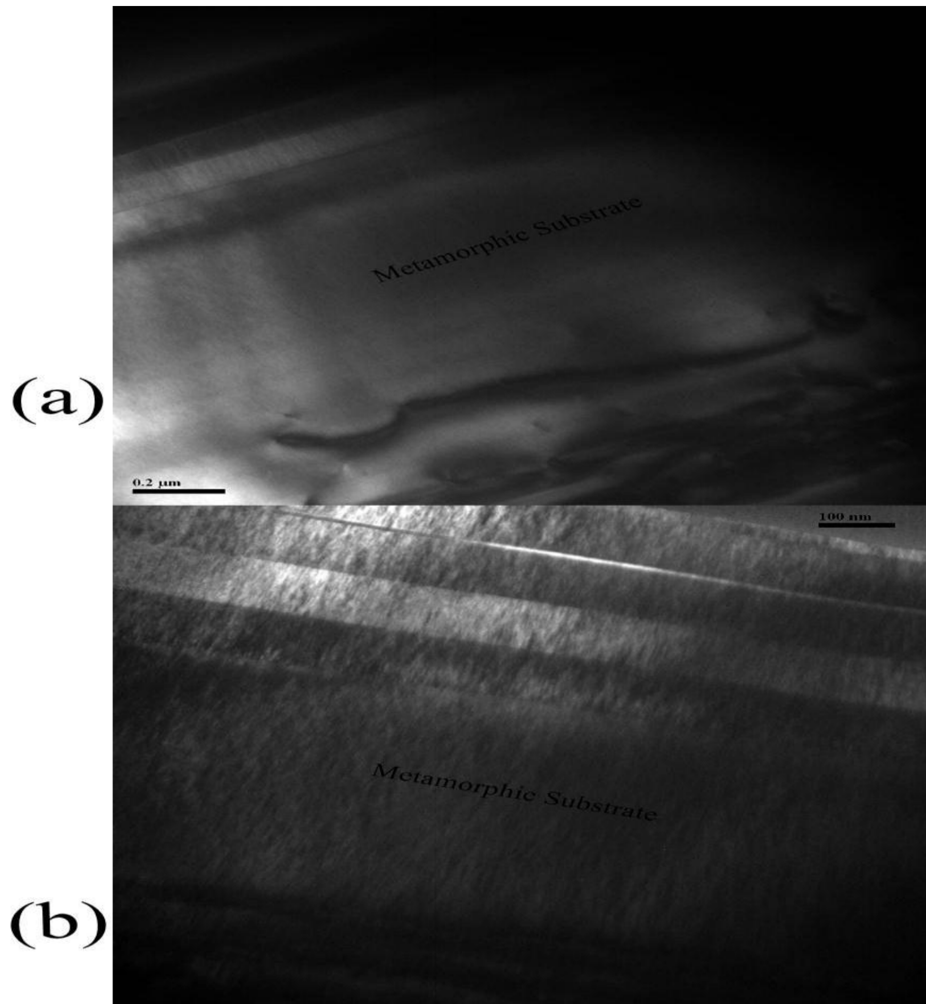

Fig 5-11: Dark field (g=200) XTEM images of (a) sample2 and (b) sample 3.

5.11 Conclusion

Relaxation was found independent of the grading laws. However, as the phase separation was severe at 500°C, lower growth temperature had to be employed for the growth of quaternary graded samples, which in turn reduces the relaxation significantly. From x-ray data, it appears that logarithmic grading gives slightly better quality than linear grading. The logarithmic grading scheme was chosen arbitrarily to see if decreasing grading rate with thickness can improve the performance. This is an indication

that instead of having simple linear grading rate, it might be useful to change the grading rate with thickness and reduce the probability of new MD nucleation as the growth continues. As the metamorphic layers are grown to yield a pseudo-substrate of different lattice constant than the substrate, relaxation of strain with low TDD is desired. Low relaxation or higher residual strain of the quaternary graded samples showed spotty surface patterns in the QW in AFM images, which is detrimental for future device growth. Etch pit density measurement showed slight improvement for logarithmic grading over linear grading. Evidence of phase separation was observed from the PL measurements of QWs grown on top of MBLs, which also increases the FWHM. DOP measurement showed that higher tensile stress is applied to the substrate for the quaternary graded samples. This might be related with the initial dislocation formation at higher thickness for quaternary graded buffers, which is not desired for metamorphic approach. Reason behind higher tensile stress in the substrate becomes evident from the TEM observation as it shows that quaternary graded samples has highly dislocated regions at higher thickness than the ternary graded samples. Moreover, quaternary graded samples shows composition modulation when observed with chemical sensitive diffraction vector, g_{200}. It was seen that the logarithmic graded samples have larger thickness which is free of MDs than the linear graded samples.

Lower relaxation rate and existence of composition modulation makes quaternary graded samples unfavourable for growing pseudo-substrates. As the target of growing meta-buffer is to change the lattice constant of substrate, lower relaxation is highly undesirable. And hence more study is required to optimize the growth of quaternary graded samples. However, logarithmic graded samples exhibited improvement over the linear graded samples, which means that it might be helpful if we have higher grading rate initially and gradually decrease the grading rate as the buffer grows.

Chapter 6 : Conclusion

6.1 Summary

A metamorphic growth of III-V semiconductor layer provides an inexpensive way for the fabrication of semiconductor devices with wider range of properties than available using normally available binary III-V substrates. This dissertation provides a systematic study for producing a III-V pseudo-substrate grown using compressive metamorphic buffers on a GaAs substrate. Different ways to improve the quality of the pseudo-substrate were investigated.

Use of lattice-matched underlying LT buffer layer had been shown to be useful for InP growth on GaAs substrate [26] and also in the InAsP MBs [27]. The same approach was applied for InGaAs MBs using a LT InGaP layer. Both crystal quality and optical qualities were probed by using x-ray and PL measurements respectively. It was shown that the InGaP LT layer used in this thesis offer no significant improvement. RTA at higher temperature (>750°C) was shown to increase the intensity of PL as the TDD is expected to decrease. However, cracks appear in the surface in <110> direction and thereby decrease the crystal quality of the pseudo-substrate.

As the strain is varied slowly, the surface of the pseudo-substrate is always in the low-mismatch regime [79]. CH appears in the surface of the pseudo-substrate as a typical characteristic of the MBs. Although the CH phenomenon is very common, the physical mechanism for the evolution of CH is still under investigation. However, it has been established that underlying MD network is correlated with the CH [55-57, 79]. For the first time, DOP analysis has been applied to measure the strain field of the pseudo-substrate. Similar type of asymmetry in orthogonal <110> directions was observed in the strain field. By comparing periodicity of strain field and surface undulation, it has been proposed that the CH forms before the nucleation of MDs. However, due to the concentration of stress in the troughs of the undulation, they become the source of new

MDs and thereby form new ridges. The area of ridges due to the dislocations gives high DOP values as they are highly strained.

Linear InGaAs MBs are typically used in order to grow devices with a larger lattice constant than GaAs on a GaAs substrate. InGaAsP MBs were grown in this work and a comparison was done with more conventional InGaAs MBs which have similar as-grown strain. In the quaternary buffers, group III ratio was kept fixed and group V ratio was varied with thickness. Changing group V fluxes is less time consuming in GSMBE growth. Comparison was also done between logarithmic and linear grading. The idea of logarithmic grading was applied to investigate whether the quality of the pseudo-substrate improved using a gradually decreasing strain profile with thickness. The likelihood of the existence of phase separation is more in quaternary buffers than ternary buffers. Thus lower growth temperature was needed for the growth of InGaAsP MBs, which in turn reduces the relaxation. However, PL measurements and TEM observations showed the existence of composition modulation in InGaAsP MBs. Lower relaxation and composition modulation makes quaternary MBs less attractive. A logarithmic grading profile shows some improvement in crystal quality over linear grading. Lower mosaicity, higher MD free thickness and lower EPD demonstrated the improved quality of logarithmic grading profile over linear grading profile. These results means that applying slightly higher grading rate initially and decreasing the grading rate close towards the final layer might be helpful to improve the quality of pseudo-substrates.

6.2 Future Research

In the growth of an MB, there are several parameters which are needed to optimize. This section discusses about the “wish-lists” as to what could be tried in order to obtain a better pseudo-substrate.

As the logarithmic grading showed some improvement, it would be worth to try to optimize the grading profile. In the case of logarithmic grading, the initial grading rate is very high. Instead of applying a very high grading rate initially, moderate grading rate

can be applied which will be fixed for first few layers, and then grading rate should be decreased as the buffer grows.

In this work, the effect of doping was omitted, whereas other work [58, 89] has already shown that Be-doping can improve the quality of InGaAs buffers. It would be interesting to see the effect of Be-doping on an optimized grading profile. InGaAs pseudo-substrates containing a high In percentage (~30%) shows high surface roughness. Be-doping might be helpful to improve the surface quality. Also Sb could be used as a surfactant to reduce the surface roughness. Use of chemical-mechanical polishing (CMP) might also prove helpful to obtain better surfaces.

REFERENCES

[1] J. J. Rosenberg, M. Benlamri, P. D. Kirchner, J. M. Woodall and G. D. Pettit, Electron Device Letters, IEEE 6 (1985) 491.

[2] J. J. Coleman, Selected Topics in Quantum Electronics, IEEE Journal of 6 (2000) 1008.

[3] T. Takamoto, T. Agui, K. Kamimura and M. Kaneiwa, in Photovoltaic Energy Conversion, 2003. Proceedings of 3rd World Conference on (2003) p. 581.

[4] M. Yamaguchi, T. Takamoto and K. Araki, Solar Energy Materials and Solar Cells 90 (2006) 3068.

[5] J. Singh, Electronic and Optoelectronic Properties of Semiconductor Structures (Cambridge University Press, 2003).

[6] J. W. Matthews and A. E. Blakeslee, Journal of Crystal Growth 27 (1974) 118.

[7] E. A. Fitzgerald, Materials Science Reports 7 (1991) 87.

[8] D. Dunstan, Journal of Materials Science: Materials in Electronics 8 (1997) 337.

[9] U. Jain, S. C. Jain, J. Nijs, J. R. Willis, R. Bullough, R. P. Mertens and R. Van Overstraeten, Solid-State Electronics 36 (1993) 331.

[10] D. B. Holt and B. G. Yacobi, Extended Defects in Semiconductors (Cambridge University Press, 2007).

[11] J. M. Titchmarsh, G. R. Booker, W. Harding and D. R. Wight, Journal of Materials Science 12 (1977) 341.

[12] M. S. Abrahams, L. R. Weisberg, C. J. Buiocchi and J. Blanc, Journal of Materials Science 4 (1969) 223.

[13] M. A. Herman and H. Sitter, Molecular Beam Epitaxy: fundamental and current status (Springer-Verlag, 1996).

[14] H. Ibach and H. Lueth, Solid-State Physics (Springer-Verlag, 2003).

[15] D. K. Bowen and B. K. Tanner, High Resolution X-ray Diffractometry and Topography (Taylor & Francis, 2002).

[16] M. Fatemi, Journal of Crystal Growth 207 (1999) 188.

[17] A. Malachias, W. N. Rodrigues, M. V. B. Moreira, S. Kycia and R. Magalh˜aes-Paniago, Journal of Physics D: Applied Physics 36 (2003) A249.

[18] H. Nagai, Journal of Applied Physics 45 (1974) 3789.

[19] M. Aindow, J. L. Batstone, L. Pfeiffer, J. M. Phillips and R. C. Pond, MRS Proceedings 138 (1988).

[20] D. T. Cassidy, S. K. K. Lam, B. Lakshmi and D. M. Bruce, Appl. Opt. 43 (2004) 1811.

[21] Y. Tang, D. H. Rich, E. H. Lingunis and N. M. Haegel, Journal of Applied Physics 76 (1994) 3032.

[22] B. Lakshmi, T. C. Daniel and B. J. Robinson, Journal of Applied Physics 79 (1996) 7640.

[23] D. B. Williams and C. B. Carter, Transmission Electron Microscopy (Springer, 2009).

[24] K. Radhakrishnan, K. Yuan and W. Hong, Journal of Crystal Growth 261 (2004) 16.

[25] H. Horikawa, Y. Ogawa, Y. Kawai and M. Sakuta, Applied Physics Letters 53 (1988) 397.

[26] A. Ren, X. Ren, Q. Wang, D. Xiong, H. Huang and Y. Huang, Microelectronics Journal 37 (2006) 700.

[27] J. A. Czaban, D. A. Thompson and B. J. Robinson, Semiconductor Science and Technology 22 (2007) 408.

[28] P. Dreszer, W. M. Chen, K. Seendripu, J. A. Wolk, W. Walukiewicz, B. W. Liang, C. W. Tu and E. R. Weber, Physical Review B 47 (1993) 4111.

[29] M. Kaminska, Liliental, x, Z. Weber, E. R. Weber, T. George, J. B. Kortright, F. W. Smith, B. Tsaur, Y and A. R. Calawa, Applied Physics Letters 54 (1989) 1881.
[30] A. C. Warren, J. M. Woodall, J. L. Freeouf, D. Grischkowsky, D. T. McInturff, M. R. Melloch and N. Otsuka, Applied Physics Letters 57 (1990) 1331.
[31] J. E. Haysom, P. J. Poole, R. L. Williams, S. Raymond and G. C. Aers, Solid State Communications 116 (2000) 187.
[32] M. R. Melloch, J. M. Woodall, E. S. Harmon, N. Otsuka, F. H. Pollak, D. D. Nolte, R. M. Feenstra and M. A. Lutz, Annu. Rev. Mater. 25 (1995) 547.
[33] O. Hulko, D. A. Thompson, B. J. Robinson and J. G. Simmons, J. Appl. Phys. 105 (2009) 073507.
[34] S. G. Tavakoli, O. Hulko and D. A. Thompson, J. Appl. Phys. 103 (2008) 10357.
[35] A. S. W. Lee, O. Hulko, D. A. Thompson, B. J. Robinson and J. G. Simmons, J. Appl. Phys. 100 (2006) 023101.
[36] K. H. Chang, R. Gilbala, D. J. Srolovitz, P. K. Bhattacharya and J. F. Mansfield, Journal of Applied Physics 67 (1990) 4093.
[37] G. H. Olsen, M. S. Abrahams and T. J. Zamerowski, J. Electrochem Soc. 121 (1974) 1650.
[38] J. A. Venables, Introduction to surface and thin film processes (Cambridge University Press, 2000).
[39] D. J. Srolovitz, Acta Metallurgica 37 (1989) 621.
[40] A. M. Andrews, A. E. Romanov, J. S. Speck, M. Bobeth and W. Pompe, Applied Physics Letters 77 (2000) 3740.
[41] K. Samonji, H. Yonezu, Y. Takagi and N. Ohshima, Journal of Applied Physics 86 (1999) 1331.
[42] R. Pal, M. Singh, R. Murlidharan, S. Agarwal, D. Pal and D. Bose, Bulletin of Materials Science 21 (1998) 313.
[43] O. Yastrubchak, T. Wosinski, T. Figielski, E. Lusakowska, B. Pecz and A. L. Toth, Physica E: Low-dimensional Systems and Nanostructures 17 (2003) 561.
[44] A. M. Andrews, J. S. Speck, A. E. Romanov, M. Bobeth and W. Pompe, Journal of Applied Physics 91 (2002) 1933.
[45] R. Beanland, M. Aindow, T. B. Joyce, P. Kidd, M. LourenÃ§o and P. J. Goodhew, Journal of Crystal Growth 149 (1995) 1.
[46] A. G. Cullis, A. J. Pidduck and M. T. Emeny, Journal of Crystal Growth 158 (1996) 15.
[47] I. Tangring, S. M. Wang, M. Sadeghi, A. Larsson and X. D. Wang, Journal of Crystal Growth 301-302 (2007) 971.
[48] R. A. Burmesiter, G. P. Pighini and P. E. Greene, Trans. TMS-AIME 245 (1969).
[49] S. Kishino, M. Ogirima and K. Kurata, J. electrochem Soc. 119 (1972).
[50] G. H. Olsen, Journal of Crystal Growth 31 (1975) 223.
[51] P. Franzosi, G. Salviati, F. Genova, A. Stano and F. Taiariol, Journal of Crystal Growth 75 (1986) 521.
[52] F. Glas, Journal of Applied Physics 62 (1987) 3201.
[53] B. J. Spencer, P. W. Voorhees and S. H. Davis, Journal of Applied Physics 73 (1993) 4955.
[54] A. J. Pidduck, D. J. Robbins, A. G. Cullis, W. Y. Leong and A. M. Pitt, Thin solid films 222 (1992) 78.
[55] A. G. Cullis, D. J. Robbins, S. J. Barnett and A. J. Pidduck, Journal of Vacuum Science & Technology A: Vacuum, Surfaces, and Films 12 (1994) 1924.

[56] D. E. Jesson, S. J. Pennycook, J. M. Baribeau and D. C. Houghton, Physical Review Letters 71 (1993) 1744.
[57] A. Jallipalli, G. Balakrishnan, S. H. Huang, A. Khoshakhlagh, L. R. Dawson and D. L. Huffaker, Journal of Crystal Growth 303 (2007) 449.
[58] I. Tangring, S. M. Wang, X. R. Zhu, A. Larsson, Z. H. Lai and M. Sadeghi, Applied Physics Letters 90 (2007) 071904.
[59] J. H. Scheel and F. Tsuguo, Crystal growth Technology 2003).
[60] F. K. LeGoues, B. S. Meyerson, J. F. Morar and P. D. Kirchner, Journal of Applied Physics 71 (1992) 4230.
[61] P. S. Zory, Quantum Well Lasers (Academic Press, 1993).
[62] B. Lakshmi, D. T. Cassidy and B. J. Robinson, Journal of Applied Physics 84 (1998) 5739.
[63] A. M. Andrews, R. LeSar, M. A. Kerner, J. S. Speck, A. E. Romanov, A. L. Kolesnikova, M. Bobeth and W. Pompe, Journal of Applied Physics 95 (2004) 6032.
[64] A. G. Cullis, A. J. Pidduck and M. T. Emeny, Physical Review Letters 75 (1995) 2368.
[65] M. Albrecht, S. Christiansen, J. Michler, W. Dorsch, H. P. Strunk, P. O. Hansson and E. Bauser, Applied Physics Letters 67 (1995) 1232.
[66] H. Gao and W. D. Nix, Annual Review of Materials Science 29 (1999) 173.
[67] K. L. Kavanagh, M. A. Capano, L. W. Hobbs, J. C. Barbour, P. M. J. Maree, W. Schaff, J. W. Mayer, D. Pettit, J. M. Woodall, J. A. Stroscio and R. M. Feenstra, Journal of Applied Physics 64 (1988) 4843.
[68] E. A. Fitzgerald, Y.-H. Xie, M. L. Green, D. Brasen, A. R. Kortan, J. Michel, Y. Mii and B. E. Weir, Applied Physics Letters 59 (1991) 811.
[69] M. K. Hudait, Y. Lin, M. N. Palmisiano, C. Tivarus, J. P. Pelz and S. A. Ringel, Journal of Applied Physics 95 (2004) 3952.
[70] A. M. Carlin, Growth and Strain Relaxation in Anion-Graded Ga(x)In(1-x)As(y)P(1-y), in "Electrical and Computer Engineering" (Ohio State University, 2010).
[71] M. Sexl, G. Bohm, M. Maier, G. Trankle, G. Weimann and G. Abstreiter, in Compound Semiconductors, 1997 IEEE International Symposium on (1998) p. 49.
[72] F. Romanato, E. Napolitani, A. Carnera, A. V. Drigo, L. Lazzarini, G. Salviati, C. Ferrari, A. Bosacchi and S. Franchi, Journal of Applied Physics 86 (1999) 4748.
[73] E. Napolitani, thesis, (Padova University, 1996).
[74] M. S. Abrahams, L. R. Weisberg and J. J. Tietjen, Journal of Applied Physics 40 (1969) 3754.
[75] C. M. Serrano and C.-A. Chang, Applied Physics Letters 39 (1981) 808.
[76] J.-I. Chyi, J.-L. Shieh, J.-W. Pan and R.-M. Lin, Journal of Applied Physics 79 (1996) 8367.
[77] F. M. Mohammedy, O. Hulko, B. J. Robinson, D. A. Thompson and M. J. Deen, Journal of Vacuum Science & Technology B: Microelectronics and Nanometer Structures 26 (2008) 636.
[78] M. K. Hudait, Y. Lin and S. A. Ringel, J. Appl. Phys. 105 (2009) 061643.
[79] E. A. Fitzgerald, S. B. Samavedam, Y. H. Xie and L. M. Giovane, Journal of Vacuum Science & Technology A: Vacuum, Surfaces, and Films 15 (1997) 1048.
[80] J. Tersoff, Applied Physics Letters 62 (1993) 693.
[81] S.-D. Kim, S. M. Lord and J. S. Harris, Journal of Vacuum Science & Technology B: Microelectronics and Nanometer Structures 14 (1996) 642.
[82] H. K. H. Choy and G. F. J. Clifton, J.Vac. Sci. Technology B 23 (2005) 2109.

[83] C. W. Leitz, M. T. Currie, A. Y. Kim, J. Lai, E. Robbins, E. A. Fitzgerald and M. T. Bulsara, Journal of Applied Physics 90 (2001) 2730.
[84] K. E. Lee and E. A. Fitzgerald, Journal of Crystal Growth 312 (2010) 250.
[85] S. G. Tavakoli, M. A. Naser, D. A. Thompson and M. Jamal Deen, Journal of Applied Physics 106 (2009) 063533.
[86] Z. Mi, C. Wu, J. Yang and P. Bhattacharya, Journal of Vacuum Science & Technology B: Microelectronics and Nanometer Structures 26 (2008) 1153.
[87] Z. Mi, J. Yang and P. Bhattacharya, Journal of Crystal Growth 301-302 (2007) 923.
[88] M. Zetian and P. Bhattacharya, Selected Topics in Quantum Electronics, IEEE Journal of 14 (2008) 1171.
[89] S. Yuxin, W. Shumin, T. Ivar, L. Zonghe and S. Mahdad, Journal of Applied Physics 106 (2009) 123531.
[90] B.-P. Wu, D.-H. Wu, H.-Q. Ni, S.-S. Huang, F. Zhan, Y.-H. Xiong, Y.-Q. Xu and Z.-C. Niu, Chinese Physics Letters 24 (2007) 3543.
[91] T. Sasaki, H. Suzuki, M. Inagaki, K. Ikeda, K. Shimomura, M. Takahasi, M. Kozu, H. Wen, I. Kamiya, Y. Ohshita and M. Yamaguchi, Photovoltaics, IEEE Journal of 2 (2012) 35.
[92] L. Yang, M. T. Bulsara, K. E. Lee and E. A. Fitzgerald, Journal of Crystal Growth 324 (2011) 103.
[93] J. Kirch, P. Dudley, T. Kim, K. Radavich, S. Ruder, L. J. Mawst, T. F. Kuech, S. D. LaLumondiere, Y. Sin, W. T. Lotshaw and S. C. Moss, in Compound Semiconductor Week (CSW/IPRM), 2011 and 23rd International Conference on Indium Phosphide and Related Materials (2011) p. 1.
[94] Y. Lin, SCIENCE AND APPLICATIONS OF III-V GRADED ANION METAMORPHIC BUFFERS ON INP SUBSTRATES in "Electrical and Computer Engineering" (The Ohio State University, 2007).
[95] J. E. Ayers, Journal of Crystal Growth 135 (1994) 71.
[96] F. M. Mohammedy, Growth, Fabrication and Characterization of metamorphic InGaSb photodetectors for application in 2.0 um and beyond, in "Electrical and Computer Engineering" (McMaster University, Hamilton, 2008).
[97] K. Hausler, K. Eberl and W. Sigle, Semiconductor science and technology 10 (1995).
[98] M. S. Goorsky, K. M. Matney, G. Chu, R. S. Goldman and K. L. Kavanagh, Advances in X-Ray Analysis 38 (1995) 221.
[99] A. R. Clawson, Guide to references on III-V semiconductor chemical etching, in "Materials Science and Engineering" (2001) p. 1.
[100] D. Rose, K. Durose, W. Palosz, A. Szczerbakow and K. Grasza, Journal of Physics D: Applied Physics 31 (1998) 1009.
[101] S. L. Brantley, S. R. Crane, D. A. Crerar, R. Hellmann and R. Stallard, Geochimica et Cosmochimica Acta 50 (1986) 2349.
[102] C. A. Wang, Applied Physics Letters 76 (2000) 2077.
[103] Y. P. Varshni, Physica 34 (1967) 149.
[104] R. R. LaPierre, T. Okada, B. J. Robinson, D. A. Thompson and G. C. Weatherly, Journal of Crystal Growth 158 (1996) 6.
[105] P. Bhattacharya, Properties of Lattice-Matched and Strained Indium Gallium Arsenide (INSPEC, the Institution of Electrical Engineers,, 1993).
[106] B. Lakshmi, Characterization of quantum wells using degree of polarization of photoluminescence, in "Engineering Physics" (McMaster University, 1997).

[107] F. K. LeGoues, B. S. Meyerson and J. F. Morar, Physical Review Letters 66 (1991) 2903.
[108] A. Rosenauer, Transmission Electron Microscopy of Semiconductor Nanostructure: An analysis of composition and strain state (Springer, 2003).
[109] M. Ichimura and A. Sasaki, Journal of Crystal Growth 98 (1989) 18.